FAKULTÄT FÜR PHYSIK
TECHNISCHE UNIVERSITÄT MÜNCHEN

Experimental power exhaust studies of the improved confinement regime at the ASDEX Upgrade tokamak

Davide Silvagni

Vollständiger Abdruck der von der Fakultät für Physik der Technischen Universität München zur Erlangung des akademischen Grades eines

Doktors der Naturwissenschaften

genehmigten Dissertation.

Vorsitzende/-r: Prof. Dr. Andreas Weiler

Prüfende/-r der Dissertation:

1. Prof. Dr. Ulrich Stroth
2. Prof. Dr. Alexander Holleitner

Die Dissertation wurde am 10.02.2021 bei der Technischen Universität München eingereicht und durch die Fakultät für Physik am 26.03.2021 angenommen.

TECHNISCHE UNIVERSITÄT MÜNCHEN

PHYSIK DEPARTMENT

LEHRSTUHL FÜR PLASMARAND UND DIVERTORPHYSIK

Experimental power exhaust studies of the improved confinement regime at the ASDEX Upgrade tokamak

Author:	Davide Silvagni
Supervisor:	Prof. Dr. Ulrich Stroth
Advisor:	Dr. Thomas Eich
Submission Date:	10$^{\text{th}}$ February 2021

Abstract

One of the major challenges for a fusion power plant is to find a plasma confinement regime that couples acceptable power loads onto the wall components and large fusion energy production. One candidate is the H-mode confinement regime, which features high energy and particle confinement. However, H-mode plasmas exhibit type-I edge localized modes (ELMs), edge instabilities that expel a large amount of plasma that transiently enhances the heat load on wall components, such as the divertor targets. Since heat fluxes due to type-I ELMs reduce the lifetime of the divertor targets, they are not accepted in a fusion power plant. A confinement regime that lacks type-I ELMs and has high energy confinement is the improved confinement mode, I-mode. However, the compatibility of I-mode plasmas with the strict requirements of a fusion power plant still needs to be assessed. In this thesis, power exhaust studies in the I-mode confinement regime are carried out at the ASDEX Upgrade tokamak. First, stationary power loads are investigated. A key parameter that sets the peak heat flux onto the divertor target is the width of the power carrying channel on open field lines called scrape-off layer (SOL) power decay length λ_q. The larger λ_q, the lower the peak heat flux. To study how λ_q scales with plasma parameters and how it correlates with SOL and edge gradients, a database encompassing different confinement regimes (L-mode, I-mode and H-mode) has been assembled. It is found that a cross-regime λ_q scaling is best described by the edge electron pressure evaluated at a normalized plasma radius of $\rho_{\mathrm{pol}} = 0.95$. Based on this λ_q scaling law, extrapolations to reactor-relevant I-mode and H-mode plasmas predict λ_q to be in the range of 0.60 mm only, with no major differences between I-mode and H-mode plasmas.
In addition, heat flux asymmetries between the outer and inner divertor targets across different confinement regimes have been investigated. This is an important effect to consider because a strongly unbalanced out-in divertor heat loads will lead to a larger heat flux on one target, increasing the material stresses. It is found that I-mode plasmas have a more balanced out-in heat flux when compared to H-mode plasmas in standard configuration and that the asymmetry depends on the magnetic field direction, pointing to the influence of fluid drifts. Also, I-mode plasmas can experience ELM-like pedestal relaxation events (PREs) that transiently increase the heat flux on the divertor targets. To study their compatibility with a fusion power plant, it is important to understand when these events appear and if their power loads will be tolerable for the divertor

targets. It is found that I-mode PREs appear only close to the H-mode transition on ASDEX Upgrade. Therefore, they can be avoided by staying away from this transition. Also, I-mode discharges both with and without PREs can reach high confinement quality, 80–100% of the H-mode. This indicates that stationary and high-confinement I-mode plasmas without PREs can be achieved. Furthermore, the relative PRE energy loss is about 1 %, and is thus lower than that of type-I ELMs. Also, the peak of the energy fluence measured on the divertor targets during PREs is lower than that of type-I ELMs for the same electron pressure at the plasma edge. However, when projections to fusion reactors are considered, it is found that the PRE divertor energy fluence might be above the material limits.

Zusammenfassung

Eine der größten Herausforderungen für ein Fusionskraftwerk ist es, ein Plasmaeinschlussregime zu finden, das akzeptable Leistungslasten auf die Wandkomponenten und eine hohe Fusionsleistung verbindet. Ein Kandidat ist das H-Mode-Einschlussregime, das sich durch hohen Energie- und Teilcheneinschluss auszeichnet. H-Mode-Plasmen weisen jedoch sog. Edge-Localized-Modes (ELMs) auf, Randinstabilitäten, die eine große Menge Plasma ausstoßen, was die Wärmebelastung der Wandkomponenten, wie z. B. der Divertorplatten, vorübergehend erhöht. Da Wärmeflüsse aufgrund von ELMs die Lebensdauer der Divertorplatten reduzieren, werden sie in einem Fusionskraftwerk nicht akzeptiert. Ein Einschlussregime ohne ELMs und mit hohem Energieeinschluss ist die I-Mode. Allerdings muss die Kompatibilität von I-Mode-Plasmen mit den strengen Anforderungen eines Fusionskraftwerks noch bewertet werden. In dieser Arbeit werden Studien zur Leistungsabgabe im I-Mode-Einschlussregime am Tokamak ASDEX Upgrade durchgeführt.
Zunächst werden die stationären Leistungsflüsse auf den Divertorplatten untersucht. Ein Schlüsselparameter, der den Spitzenwärmefluss festlegt, ist die Breite des leistungsführenden Kanals auf offenen Feldlinien (Abschälschicht, engl. scrape-off layer, SOL), die sogenannte Leistungsabfalllänge λ_q. Je größer λ_q ist, desto geringer ist der Spitzenwärmefluss. Um zu untersuchen, wie λ_q mit den Plasmaparametern skaliert und wie es mit SOL- und Randgradienten des Plasmadrucks korreliert, wurde eine Datenbank zusammengestellt, die verschiedene Einschlussregime (L-Mode, I-Mode und H-Mode) umfasst. Es wird festgestellt, dass eine regimeübergreifende λ_q-Skalierung am besten durch den Randelektronendruck beschrieben wird, der bei einem normierten Plasmaradius von $\rho_{\mathrm{pol}} = 0,95$ ausgewertet wird. Basierend auf diesem Skalierungsgesetz sagen Extrapolationen voraus, dass λ_q in einem Reaktor im Bereich von nur 0,60 mm liegt, wobei es keine größeren Unterschiede zwischen I-Mode- und H-Mode-Plasmen gibt.
Darüber hinaus wurden Wärmeflussasymmetrien zwischen den äußeren und inneren Divertorplatten über verschiedene Einschlussregime hinweg untersucht. Dies ist ein wichtiger Effekt, der berücksichtigt werden muss, da eine stark unausgewogene Wärmebelastung zu einem größeren Wärmefluss auf eine Platte führt, was die Materialspannungen erhöht. Es wird festgestellt, dass I-Mode-Plasmen im Vergleich zu H-Mode-Plasmen einen ausgeglicheneren Wärmefluss aufweisen und dass die Asymmetrie von der Magnetfeldrichtung abhängt, was

auf den Einfluss von Fluiddriften hinweist.
Außerdem können in I-Mode-Plasmen ELM-ähnliche Randinstabilitäten (Pedestal-Relaxation-Events, PREs) auftreten, die den Wärmefluss auf die Divertorplatten vorübergehend erhöhen. Um ihre Kompatibilität mit den Anforderungen eines Fusionskraftwerk zu untersuchen, ist es wichtig zu verstehen, wann diese Ereignisse auftreten und ob ihre Leistungsbelastung für die Divertorplatten tolerierbar ist. Es wird festgestellt, dass PREs nur in der Nähe des Übergangs von der I- zur H-Mode auftreten. Daher können sie vermieden werden, indem man sich von diesem Übergang fernhält. Außerdem können I-Mode-Entladungen sowohl mit als auch ohne PREs eine hohe Einschlussqualität erreichen. Dies zeigt, dass stationäre I-Mode-Plasmen mit hohem Einschluss ohne PREs erreicht werden können. Darüber hinaus liegt der relative Energieverlust durch PREs bei ca. 1 % und ist damit geringer als der von ELMs. Auch die maximale Energiefluenz, die während der PREs auf den Divertorplatten gemessen wird, ist bei gleichem Elektronendruck am Plasmarand niedriger als bei ELMs. Betrachtet man jedoch Projektionen auf Fusionsreaktoren, so stellt man fest, dass die Energiefluenz auf die Divertorplatten oberhalb der Materialgrenzen liegen könnte.

Contents

Chapter 1

Introduction

1.1 Nuclear Fusion as an energy source

During the last 200 years a huge increase in the world energy consumption has taken place. This is not only related to the marked world population growth that occurred in the last century, but also to the increased per capita energy consumption of several countries. To fulfill the new world thirst for energy, fossil fuel usage rose dramatically in the last decades. This is leading to a relentless global warming, which is seriously threatening the environmental world balance. In this context, new energy sources that can ultimately substitute fossil fuels need to be found. With regard to electricity production, the combination of nuclear fusion and renewable energies might be able to provide a fossil-fuel-free electricity base load [1].
Energy production by fusion reactions takes advantage of the large amount of energy released when two light nuclei fuse together giving birth to a heavier nucleus. Different fusion reactions can be considered to create energy, but the one with the largest cross section (and so with largest probability to happen) at technically feasible temperatures is the deuterium (D) tritium (T) reaction:

$$ {}^{2}_{1}\mathrm{D} + {}^{3}_{1}\mathrm{T} = {}^{4}_{2}\mathrm{He} + \mathrm{n} + 17.6\,\mathrm{MeV}. \tag{1.1} $$

Deuterium can be extracted from sea water, whereas tritium has a half-life time of 12.3 years and therefore does not abound in nature. Tritium can be generated by lithium reacting with neutrons directly in the reactor. Lithium is relatively abundant on Earth and resources are likely to be sufficient for several hundreds of years [2, 3].
To fuse, nuclei need to overcome the Coulomb barrier, for which they need to be heated towards high temperatures. For the D-T fusion reaction the maximum cross-section is achieved at temperatures of about 14 keV (approximately 150 million K). At these high temperatures atoms are ionized and in the plasma state. In fusion science, we define ignition the point where a fusion plasma generates enough heating power to run self-sustained without external heating. The Lawson criterion [4] defines the conditions needed to reach ignition. This

criterion forces a threshold for the triple product $n\tau_E T$, where n is the plasma density, τ_E the energy confinement time and T the plasma temperature. The energy confinement time is defined as:

$$\tau_E = \frac{W}{P_{\text{loss}}}, \tag{1.2}$$

where W is the plasma stored energy and P_{loss} is the power lost from the plasma. Stars make use of the strong gravitational force to confine the plasma and achieve ignition. On Earth, at the moment there are two main ideas to confine plasma. The first is to use strong magnetic fields that can trap charged particles present in the plasma, thanks to the Lorentz force. The second is to compress and heat a small fuel pellet with lasers for hundreds of picoseconds. The former approach led to the development of magnetic confinement fusion (MCF) reactors, whereas the latter led to the progress of inertial confinement fusion (ICF) reactors. These two different approaches try to satisfy the Lawson criterion in different ways. MCF reactors rely on low plasma densities ($10^{20}\,\text{m}^{-3}$) and long energy confinement times (few seconds) to reach ignition; ICF reactors, conversely, rely on high plasma densities ($10^{31}\,\text{m}^{-3}$) and short energy confinement time (hundreds of picoseconds) [5]. In this work the attention is turned to MCF reactors and in particular to tokamaks.

1.2 The tokamak concept

The tokamak is a magnetic confinement device with a toroidal shape, first proposed by Soviet Union scientists in the 1950s [6]. The toroidal geometry has been introduced in order to reduce plasma particle losses. In fact, in a tokamak charged particles exhibit a cyclotron motion around the magnetic field lines, because of the Lorentz force. As a consequence, plasma is compelled to move along magnetic field lines. In a linear geometry, a large fraction of plasma particles is lost when the magnetic field line intersects the wall of the linear device. That is why magnetic field lines that close upon themselves in a toroidal geometry are required. However, a magnetic field line topology with only a toroidal component would not stop particles to escape. This is because the curvature of the magnetic field lines induces a drift of charged particles that would cause charge separation in the vessel and, hence, the creation of an electric field. The resulting $\vec{E} \times \vec{B}$ fluid drift velocity will cause charged particles to move radially outwards and to escape the magnetic cage.
For this reason a poloidal magnetic field component is added, so as to compensate for the charge separation and thus to allow for energy confinement times of sufficient duration to meet the ignition criteria. The combination of toroidal and poloidal components creates helical magnetic field lines that are wrapped around a central axis.
A sketch of the magnetic field line topology in a tokamak is shown in Fig. 1.1. In a tokamak the poloidal magnetic field is produced by a toroidal plasma cur-

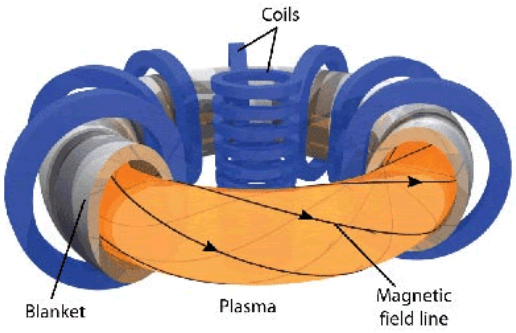

Figure 1.1: Schematic of a magnetically confined plasma in a tokamak, from [7].

rent, induced by an external solenoid. The toroidal magnetic field is instead generated by torodial magnetic field coils. An additional set of vertical coils is also needed to position the plasma inside the vacuum vessel and to avoid vertical displacement.
The equilibrium state of a tokamak is characterized by the following magneto-hydrodynamic (MHD) equation, which comes from momentum conservation:

$$\vec{J} \times \vec{B} = \nabla p, \tag{1.3}$$

where $\vec{J}$ is the plasma current, $\vec{B}$ is the magnetic field and p is the kinetic plasma pressure. Let us consider contours of constant pressure in a well-confined plasma, as illustrated in Fig. 1.2. From Eq. 1.3 it follows that $\nabla p \cdot \vec{B} = 0$, i.e. magnetic field lines lie in the surface of constant pressure. For this reason such contours are also called magnetic flux surfaces. Furthermore, $\nabla p \cdot \vec{J} = 0$, i.e. also the plasma current flows on the magnetic flux surfaces. In a plasma in equilibrium, magnetic flux surfaces are nested toroidally, as shown in Fig. 1.2. Since the parallel heat conductivity is much larger than the radial one, it is a good approximation to consider the plasma temperature T and density n constant on flux surfaces. For this reason, in a tokamak the main plasma quantities are often expressed as a function of a flux surface label, reducing thus a 3D system to a 1D system. This is an advantage of the tokamak, which allowed tokamak research to flourish in the 1960s without the need of strong computational power.

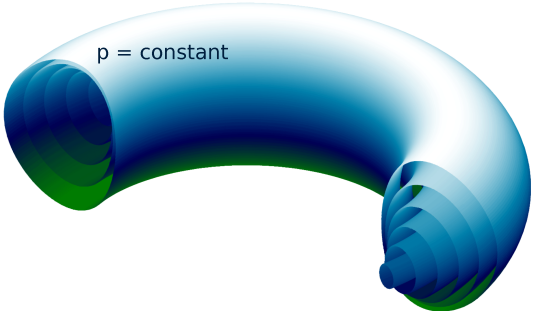

Figure 1.2: Toroidally nested magnetic flux surfaces of constant pressure that characterize a torodial plasma in equilibrium, adapted from [8].

Currently, several tokamak experiments of different size are in operation around the world. The size of a tokamak is described by the major radius R, which is the distance between the center of the torus and the magnetic axis of the plasma. In Europe, the largest tokamak is the Join European Torus (JET) [9] with a major radius of $R = 2.96\,\mathrm{m}$. Additionally, medium-size European devices are the Axially Symmetric Divertor EXperiment (ASDEX) Upgrade tokamak [10], the Mega Amp Spherical Tokamak (MAST) [11] and the Tokamak à Configuration Variable (TCV) [12]. In Asia, two notable tokamaks are the Japan Torus-60 Upgrade (JT-60U) [13] in Japan and the Experimental Advanced Superconducting Tokamak (EAST) [14] in China with a major radius of $R = 3.4\,\mathrm{m}$ and $R = 1.7\,\mathrm{m}$, respectively. In the U.S., prominent tokamak experiments are DIII-D [15] and Alcator C-Mod [16]. The largest tokamak experiment in the world is the International Thermonuclear Experimental Reactor (ITER) [17] in France with a major radius of $R = 6.2\,\mathrm{m}$, which will start operation after 2025.

1.3 The limiter and divertor configurations

The plasma confined in a tokamak is surrounded by a vacuum vessel. Magnetic field lines that lie in flux surfaces that never make contact with the wall are called "closed", while those that intersect the wall are called "open". In tokamaks, an important magnetic flux surface is the so-called last closed (magnetic) flux surface (LCFS). The LCFS is the last flux surface that does not touch the wall. It separates two different regions of the tokamak: the confined plasma, i.e. the region composed of closed magnetic field lines, and the scrape-off layer (SOL), i.e. the region composed of open magnetic field lines that are in contact with the wall. To label magnetic flux surfaces, the normalized minor plasma radius ρ_{pol} is defined:

$$\rho_{\mathrm{pol}} = \sqrt{\frac{\Psi - \Psi_{\mathrm{axis}}}{\Psi_{\mathrm{LCFS}} - \Psi}}, \tag{1.4}$$

where Ψ is the poloidal magnetic flux, Ψ_{axis} is the flux through the ring defined by the magnetic axis and Ψ_{LCFS} is the flux at the LCFS. In tokamaks, another important quantity to characterize magnetic field lines on a flux surface is the safety factor q_{s}. A magnetic field line that starts at a defined position, it will return to that position after a toroidal angle change $\Delta\phi$. The safety factor is thus defined as:

$$q_{\mathrm{s}} = \frac{\Delta\phi}{2\pi} \approx \frac{rB_t}{RB_p}, \tag{1.5}$$

where r is the minor radius of the magnetic flux surface, i.e. the distance between the magnetic axis and the flux surface, R is the major radius, while B_t and B_p are the toroidal and poloidal components of the magnetic field. The approximate expression in Eq. 1.5 is valid for tokamaks with large aspect ratio

$A = R/a$, with a being the plasma minor radius, i.e. the minor radius of the LCFS. Typically, $A > 3$ in tokamaks.
The plasma that enters the SOL will eventually reach the wall and for reactor conditions the resulting wall erosion can be substantial [18]. To limit the plasma-wall interaction to a smaller and well defined region, while protecting the vessel, a protruding element – called *limiter* – is inserted into the vessel, as shown in Fig. 1.3(a). The limiter configuration has been used in tokamaks for several decades. However, this configuration introduces a large amount of impurities, i.e. atoms other than deuterium and tritium, in the confined plasma. They enter the plasma as neutrals coming from the first wall elements. Impurities are mainly produced because of sputtering of wall materials, desorption of surface atoms, evaporation of bulk material, arcing, and chemical reactions [19]. The proximity of the limiter to the LCFS enhances

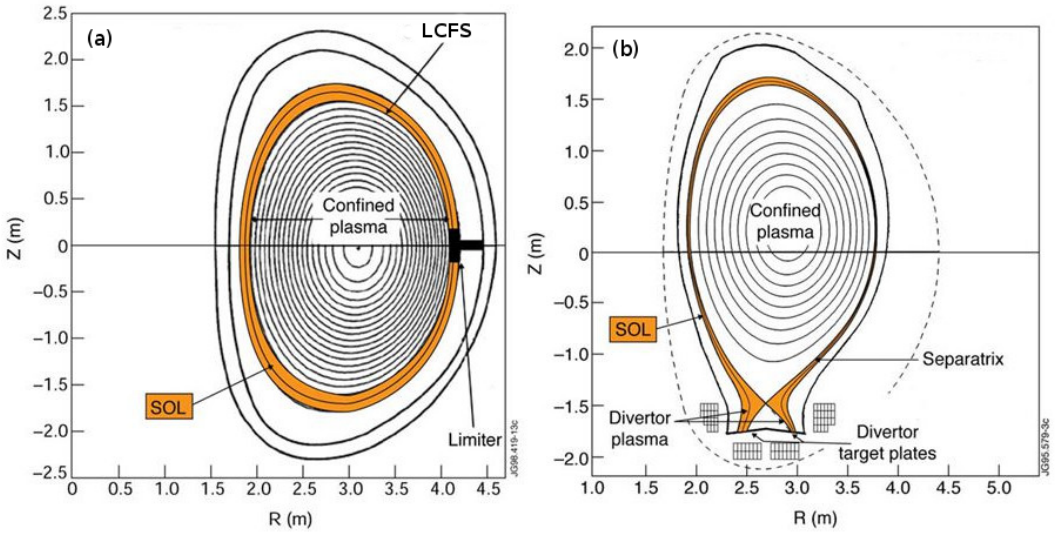

Figure 1.3: Limiter (a) and divertor (b) configuration in the JET tokamak. Adapted from [20].

the probability for impurities to enter the confined plasma. A large impurity content in the confined plasma will cause fuel dilution and increased radiative losses, reducing plasma core pressure and, hence, fusion reactions. To increase the distance between the plasma facing components and the LCFS a different magnetic configuration has been introduced in the 1980s, the *divertor* configuration [21]. In this configuration an external conductor carries a toroidal current flowing in the same direction as the plasma current. This leads to the formation of a point where the poloidal magnetic field is zero (a null), which is termed X-point. A typical divertor configuration features one active X-point and is called a single null configuration. The active X-point can be created in the lower or in the upper part of the vessel. We refer to them as lower single null (LSN) or upper single null (USN) configurations, respectively. A divertor LSN configuration is shown in Fig. 1.3(b). The magnetic flux surface passing

through the X-point is called separatrix.
The plasma flowing into the SOL will ultimately reach the solid surfaces located below the X-point, which are called divertor target plates. The divertor targets are thus the solid components in charge of withstanding the largest amount of heat and particle flux. The divertor configuration has several advantages with respect to the limiter one. The most prominent ones are the reduced impurity content in the confined region, better helium pumping and the achievement of enhanced energy confinement regimes, which will be discussed in the next section.

1.4 Confinement regimes

In a tokamak device with divertor configuration, confinement regimes are divided into three main categories: the low-energy confinement mode (L-mode), the improved-energy confinement mode (I-mode) and the high-energy confinement mode (H-mode).
L-mode plasmas are characterized by electron temperature and density profiles that are less steep at the plasma edge than those of H-mode plasmas. L-mode plasmas have low energy confinement time.
H-mode plasmas are characterized by steep edge temperature and density profiles, and that is why they achieve higher energy and particle confinement times with respect to L-mode plasmas. H-mode plasmas are more easily achieved in tokamaks with divertor configuration, and for this reason they were discovered only in 1982 in the first diverted tokamak (ASDEX) [22]. In H-mode, steep edge profiles form because an edge transport barrier develops, which reduces turbulent transport. This leads to the formation of the so-called *pedestal*, i.e. an about 2-cm-wide region in the tokamak edge where profiles exhibit steep gradients. The steepening up of the profiles is limited by the appearance of magnetohydrodynamic (MHD) instabilities that are triggered by the large edge current and pressure gradient. These instabilities, called edge-localized modes (ELMs) [23], periodically relax the pedestal profiles, expelling energy and particles from the confined region into the SOL. This large amount of energy and particle ultimately reaches the divertor target plates, causing enhanced thermomechanical stresses in the material and reducing the divertor tiles lifetime. For a review on ELMs see [24]. Different kinds of ELMs can occur in H-mode plasmas. They have been classified into three main categories [25]: type-I ELMs, type-II ELMs and type-III ELMs. Among all kinds of ELMs, type-I ELMs expel the highest amount of energy from the confined region, and for this reason they need to be avoided in a future fusion power plant to allow for a sufficient long life time of the divertor target plates [26].
Nevertheless, stationary H-mode plasmas without ELMs also exist [27]. The more prominent ones are the quiescent H-mode (QH-mode) [28–31] and the enhanced D_α H-mode (EDA H-mode) [32, 33]. Both are characterized by the appearance of an edge instability (the edge harmonic oscillation in the QH-

mode and the quasi-coherent mode in the EDA H-mode) which enhances the edge particle transport while leaving the energy transport only moderately affected. In this way, ELMs are avoided while retaining high energy confinement. Whereas stationary QH-mode plasmas were to date achieved only in diverted tokamak with a carbon wall, EDA H-mode plasmas appear in tokamaks with high-Z material wall (molybdenum in Alcator C-Mod [34] and tungsten in ASDEX Upgrade [35]).
Another confinement regime without type-I ELMs is the I-mode. It was discovered in 1998 on the ASDEX Upgrade (AUG) tokamak [36], however it has gained particular attention only after 2010, thanks to the intense research activity carried out at the Alcator C-Mod tokamak [37]. I-mode plasmas are characterized by the steepening of the edge temperature profile, while the edge density profile remains similar to that of L-mode plasmas. This results in a high-energy confinement, while particle confinement stays L-mode like. In this way, the I-mode simultaneously combines the desired properties of L-mode and H-mode plasmas, namely reduced impurity and helium ash accumulation in the plasma core [38], and high energy confinement. Moreover, as mentioned earlier, I-mode plasmas are free of type-I ELMs. This makes the I-mode an attractive confinement regime for a future fusion power plant.
In this thesis, I-mode plasmas will be investigated with particular focus on their SOL and divertor characteristics. Divertor and SOL parameters of a confinement regime are important to study because they influence the amount of power reaching the divertor targets, which is one of the critical issue on the pathway to the development of a fusion power plant.

1.5 The power exhaust challenge

In tokamaks, to increase the triple product $n\tau_E T$, the energy confinement time τ_E needs to be increased. This is because the temperature has an optimum value above which the cross-section of the fusion reaction decreases, while the density is limited by an empirical limit (so-called Greenwald density limit) [39], above which the plasma disrupts. The Greenwald density limit is given by

$$n_{\mathrm{GW}} = I_p/(\pi a^2), \tag{1.6}$$

where n_{GW} is the line-averaged density in $10^{20}\,\mathrm{m}^{-3}$, I_p is the plasma current in MA and a is the minor radius in m.
As we saw in the previous section, τ_E changes with the confinement regime, but it also changes with plasma and engineering parameters. In 1999, a multi-machine scaling law of the energy confinement time in H-mode plasmas was developed [40]. This scaling law, termed IPB98(y,2), predicts

$$\tau_E \propto R^2, \tag{1.7}$$

i.e. the energy confinement time increases quadratically with machine size. Therefore, to maximize the triple product, increasing the major radius of the

tokamak is envisaged; however, with increased machine size, power exhaust becomes more and more challenging. Fusion power by α particles ($^4_2$He, see Eq. 1.1) will be the dominant heating source in a future fusion power plant, and such fusion power increases with R^3 [41]. All this power, if not lost by electromagnetic radiation, will cross the separatrix and ultimately reach the divertor target plates. The power reaching the divertor targets will deposit over a *wetted area* which can be described as

$$A = 2\pi R_{\mathrm{div}} \lambda_{\mathrm{int}}^{\mathrm{tgt}} f_{\mathrm{tor}}, \tag{1.8}$$

where R_{div} is the major radius at the divertor target, $\lambda_{\mathrm{int}}^{\mathrm{tgt}}$ is the extent of the wetted area along the divertor target and f_{tor} is the toroidal wetted fraction, i.e. an engineering parameter that takes into account the toroidal tilt of the divertor targets plates (which reduces the wetted area). In order not to increase the peak heat flux onto the divertor targets ($\mathrm{W/m^2}$) while increasing machine size, $\lambda_{\mathrm{int}}^{\mathrm{tgt}}$ has to rise at least quadratically with R. Studying how $\lambda_{\mathrm{int}}^{\mathrm{tgt}}$ changes with plasma and engineering parameters is one of the main goals of power exhaust studies and also of this thesis.
In addition to steady-state heat loads, also transient heat loads can occur in tokamaks. These are mainly due to transient events, such as ELMs, that expel over a short time a large amount of energy into the SOL. Thus, a key research activity for power exhaust is to evaluate and be able to predict the amount of heat flux that such transient events expel on the divertor target plates. In this thesis, pedestal relaxation events which appear during I-mode will be investigated in detail.
Moreover, in a diverted tokamak with a single null, open magnetic field lines cross the divertor target plates in two main areas (see Fig. 1.3 (b)): on the low-field side, i.e. on the *outer* targets, and on the high-field side, i.e. on the *inner* targets. The power that enters the SOL can be transported asymmetrically on the inner and outer target plates, leading to a larger amount of heat flux deposited on one of the two tile categories, which will be more prone to damage. Therefore, power exhaust studies are also focused in understanding and being able to predict the power and heat flux sharing between inner and outer divertor targets.

1.6 Scope of this thesis

The main goal of this thesis is to investigate steady-state and transient heat loads of I-mode plasmas, and to compare them to those of other confinement regimes, such as L-mode and H-mode. All the experimental work has been carried out at the ASDEX Upgrade tokamak.
In the first part of the thesis, the variation of the scrape-off layer power width λ_q (a quantity strictly related to $\lambda_{\mathrm{int}}^{\mathrm{tgt}}$) across different confinement regimes, among which the I-mode, is studied. Such a cross-regime investigation is accompanied by measurements of temperature, density and pressure gradient

lengths in the SOL and pedestal. A unique dataset is assembled and used to investigate in detail correlations between gradient lengths at the outer midplane (both in the SOL and in the confined region) and the SOL power width measured at the divertor target. In this part, also heat flux asymmetries between inner and outer divertor targets are investigated.
In the second part of the thesis, divertor transient heat loads associated to pedestal relaxation events recently found in I-mode plasmas are investigated. These events, first reported from the Alcator C-Mod tokamak, are here studied for the first time in detail. Their appearance, edge profile evolution and characteristic SOL transport are investigated, besides their associated transient heat loads.
The thesis is organized as follows. In chapter 2, relevant aspects of steady-state and transient power loads are introduced. In chapter 3, plasma edge characteristics of different confinement regimes are described. The ASDEX Upgrade tokamak, with its most relevant diagnostics, is introduced in chapter 4. Chapter 5 reports on a cross-regime analysis of SOL power width, gradient lengths and in-out divertor asymmetry. The investigation of I-mode pedestal relaxation events and their transient heat loads is performed in chapter 6. Finally, in chapter 7, the summary, conclusions and outlook for future research are presented.

Chapter 2

Power exhaust

In this chapter, an overview of tokamak power exhaust research is given. The basic terminology and previous works which constitute the foundations of this thesis are presented. The analysis is divided in steady-state and transient power loads, as different physics processes and models are associated with these two aspects of power exhaust.

2.1 Steady-state divertor power loads

Power loads are considered steady-state when their modulations are averaged faster than the typical measurement time scale. Such conditions are present in L-mode plasmas, in inter-ELM (or ELM-free) H-mode plasmas and, as it will be shown in this thesis, in most of the analyzed I-mode plasma intervals. In these plasmas, heat flux modulations caused by turbulent fluctuations (10–100 kHz range) are faster than the measurement frequency of the data acquisition (kHz). In a future fusion power plant, the maximum tolerable steady-state heat flux on the divertor tiles is $5 - 10\,\mathrm{MW/m^2}$ [42–44]. For comparison, the maximum heat flux on a missile during ballistic re-entry is about $4\,\mathrm{MW/m^2}$ [45]. Before discussing available models, some basic quantities needed to characterize divertor power loads are introduced in the following subsection.

2.1.1 Flux expansion and tile tilting

Two important quantities for power exhaust studies are A_{wet}, the plasma-wetted area of the divertor targets, and $A_{||}^{\mathrm{SOL}}$, the cross-sectional area of the scrape-off layer (SOL) perpendicular to the magnetic field line, see Fig. 2.1. The latter defines the parallel heat flux flowing in the SOL. In a diverted tokamak, the major radius R at the inner and outer divertor target plates can be considered equal, in a first approximation (see Fig. 1.3 for instance). Therefore, $A_{\mathrm{wet,in}} \simeq A_{\mathrm{wet,out}}$ and A_{wet} is defined in Eq. 1.8 with $f_{\mathrm{tor}} = 1$, i.e. the divertor tiles are assumed not to be toroidally tilted. Since the radial

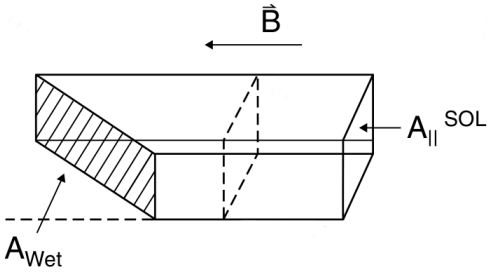

Figure 2.1: Plasma-wetted area of the divertor targets A_{wet}, and cross-sectional area of the SOL perpendicular to the magnetic field line $A_{||}^{\mathrm{SOL}}$. Figure adapted from [45].

component of the magnetic field B_{r} is usually smaller than the toroidal and poloidal components, B_{t} and B_{p}, the angle between the magnetic field line and the divertor target is approximately $\alpha \simeq \arctan(B_{\mathrm{p}}/B_{\mathrm{t}}) = \arcsin(B_{\mathrm{p}}/B)$. Then, $A_{||}^{\mathrm{SOL}}$ can be expressed as

$$A_{||}^{\mathrm{SOL}} \simeq A_{\mathrm{wet}} \sin\alpha \simeq 4\pi R \lambda B_{\mathrm{p}}/B, \tag{2.1}$$

where we dropped the superscript 'tgt' and the subscript 'int' on λ as it can be now calculated along the entire SOL. Also, the approximation $R_{\mathrm{div}} \simeq R$ was introduced.
In a diverted tokamak, the total magnetic field strength decays with the major radius as $B \propto R^{-1}$. For this reason, it does not vary strongly along the SOL, as the variation of R is small. Therefore, the cross-sectional area $A_{||}^{\mathrm{SOL}}$ of any SOL flux tube, i.e. magnetic flux bundle, does not vary greatly in the SOL and it can be considered constant to first approximation [45]. However, the ratio B_{p}/B varies substantially along the SOL, see Fig 2.2. For instance, at the outer midplane, B_{p}/B is about $1/4$; near the X-point, $B_{\mathrm{p}}/B \to 0$; while at the divertor targets, it increases back to typically $1/10$. Since $A_{||}^{\mathrm{SOL}}$ is approximately constant, from Eq. 2.1 it follows that the width of the SOL cross-sectional area λ varies along the SOL: it is short at the outer midplane, it gets longer near the X-point and it becomes shorter at the target. We can then define the flux expansion as

$$f_x := \frac{\Delta l_{\mathrm{t}}}{\Delta l_{\mathrm{u}}} = \frac{l_{\mathrm{t}}}{l_{\mathrm{u}}} \frac{1}{\sin\beta} \simeq \frac{(B_{\mathrm{p}}/B)_{\mathrm{u}}}{(B_{\mathrm{p}}/B)_{\mathrm{t}}} \frac{1}{\sin\beta}, \tag{2.2}$$

where l is the distance between the separatrix and a SOL flux surface in the poloidal plane, the subscripts 't' and 'u' stand for target and upstream (i.e. somewhere above the X-point), respectively, Δl_{t} is the projection of l_{t} on the divertor target plate and $\Delta l_{\mathrm{u}} = l_{\mathrm{u}}$. The angle on the poloidal plane between the SOL flux surface and the divertor target plate is called β. In the last form of Eq. 2.2, we used the assumption of constant $A_{||}^{\mathrm{SOL}}$ and Eq. 2.1 with $\lambda = l$.
By increasing the flux expansion, the wetted area broadens, and divertor heat loads reduce. To further increase f_x, one may be tempted to choose small

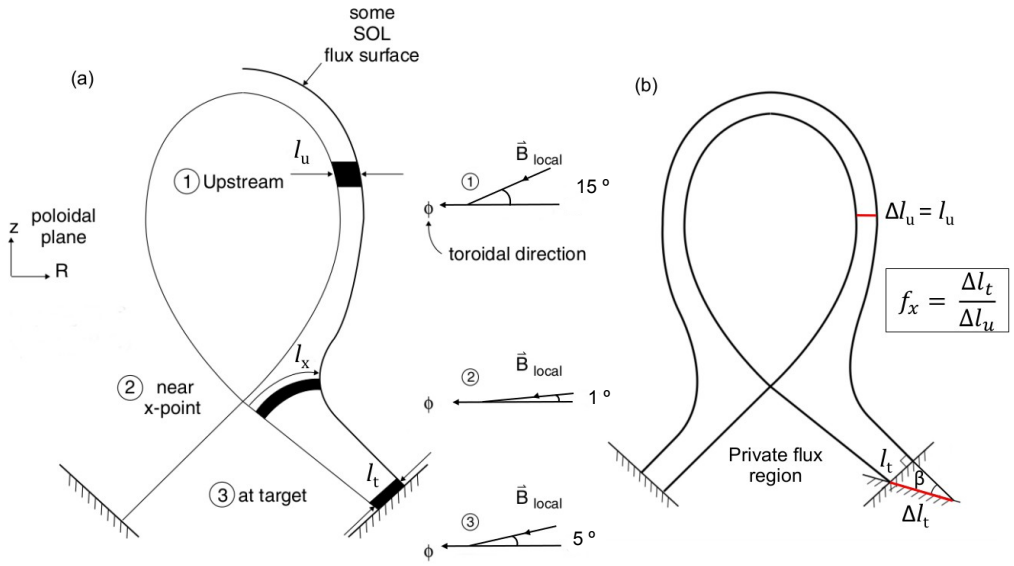

Figure 2.2: (a) Variation of the width of a SOL flux tube l on the poloidal plane due to the variation of the ratio B_p/B along the SOL. (b) Definition of flux expansion f_x. Figure adapted from [45].

values of β, thus reducing the angle between the magnetic field line and the divertor target. However, there are engineering constraints which are incompatible with grazing angles $< 1°$.
In order to allow thermal expansion of the divertor target plates and their installation, assembly and maintenance, they are constructed of separate tiles; however, this separation causes a tile edge (the so-called leading edge) to receive a large amount of heat flux at small grazing angles, which can lead to damage of the tile, see Fig. 2.3 (a). To mitigate this problem, divertor tiles can be slightly tilted toroidally to shadow the edge of the neighboring one, see Fig. 2.3 (b). This expedient, however, reduces the operational flexibility of the tokamak, since the divertor is optimized for a reduced number of B_p/B values. In addition, it reduces the wetted area, as a fraction of each tile is shadowed by the neighboring one. The toroidal wetted fraction f_tor introduced in Eq. 1.8 accounts for such a reduction.

2.1.2 Heat flux model

To describe steady-state heat fluxes onto the divertor target plates a model is used: Above the X-point in the SOL, the heat flux parallel to the magnetic field lines q decays exponentially in the direction s perpendicular to the flux surface:

$$q(s) = q_0 \exp\left(-\frac{s - s_\mathrm{sep}}{\lambda_q f_x}\right) \qquad \text{for } s > s_\mathrm{sep}, \tag{2.3}$$

where s_sep is the separatrix position, λ_q is the power decay length at the outer midplane and q_0 is the parallel heat flux at the separatrix. Below the X-point

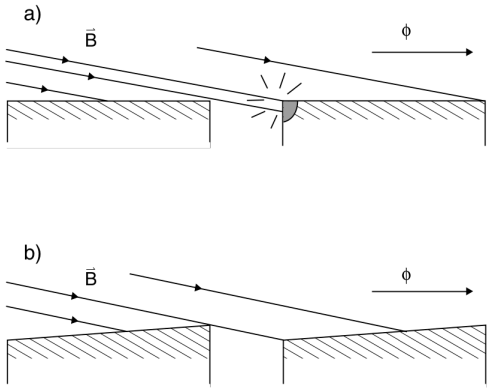

Figure 2.3: (a) At small grazing angles, a leading edge receives large amount of heat flux due to the toroidal separation of the divertor tiles. (b) By tilting toroidally the divertor tiles, the leading edge can be shadowed and protected. Figure adapted from [45].

in the SOL (i.e. in the so-called divertor chamber), the heat flux can diffuse also into the private flux region (see Fig. 2.2 (b)). A 1D diffusion process can be modeled with a Gaussian function:

$$g(s) = \frac{1}{S\sqrt{\pi}} \exp\left(-\left(\frac{s - s_{\text{sep}}}{S}\right)^2\right), \tag{2.4}$$

where S is the divertor broadening, i.e. a parameter related to the standard deviation of the Gaussian, which is defined as

$$S = \sqrt{4\chi_\perp \tau_{||}}, \tag{2.5}$$

where $\chi_\perp$is the perpendicular heat diffusivity and $\tau_{||}$ is the parallel diffusion time from the X-point to the target. Steady-state heat loads on the divertor target are described by convolving of $g(s)$ and $q(s)$ (with $q(s) = 0$ for $s < s_{\text{sep}}$) [46], which gives:

$$q(s) = \frac{q_0}{2} \exp\left(\left(\frac{S}{2\lambda_q}\right)^2 - \frac{s - s_{\text{sep}}}{\lambda_q f_x}\right) \operatorname{erfc}\left(\frac{S}{2\lambda_q} - \frac{s - s_{\text{sep}}}{S f_x}\right). \tag{2.6}$$

In this formulation, S and λ_q represent quantities mapped to the outer midplane via the flux expansion f_x, and s is the spatial coordinate along the divertor target plate. Figure 2.4 shows an example of several heat flux divertor profiles with constant λ_q and varying S. When S increases, the profile broadens and the peak heat flux reduces.
An important shape-independent quantity to characterize divertor heat loads is the so-called integral power decay length [48]:

$$\lambda_{\text{int}}^{\text{tgt}} = \lambda_{\text{int}} f_x \coloneqq \frac{\int q(s)\mathrm{d}s}{q_{\max}}, \tag{2.7}$$

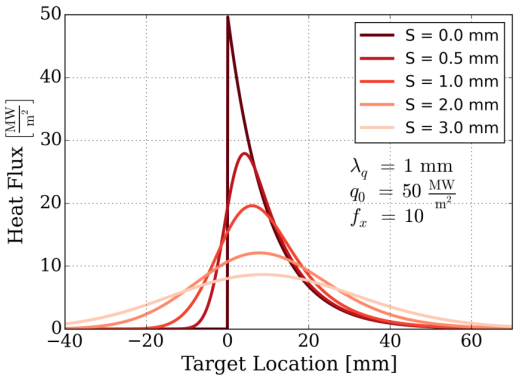

Figure 2.4: Heat flux profiles onto divertor target with constant λ_q and different S parameters. A larger S decreases the peak heat flux. Figure adapted from [47].

where $q_{\max}$ is the peak heat flux on the divertor target, and λ_{int} is the corresponding integral power decay length mapped to the outer midplane. Using Eq. 2.6, one can express the integral power decay length as a function of λ_q and S [49]:

$$\lambda_{\text{int}} \simeq \lambda_q + 1.64\, S \tag{2.8}$$

The integral power decay length allows to calculate the peak heat flux on the divertor target, which is the quantity that serves for a direct comparison to material limits:

$$q_{\max} = \frac{\int q(s)\mathrm{d}s}{\lambda_{\text{int}} f_x} = \frac{P_{\text{div}}}{2\pi R_{\text{div}} f_{\text{tor}} \lambda_{\text{int}} f_x}, \tag{2.9}$$

where P_{div} is the power onto the divertor target plate, R_{div} is the major radius at the divertor target, and f_{tor} accounts for the reduction of exposed toroidal circumference due to the torodial inclination of the tiles. Therefore, in order to estimate the peak heat flux onto divertor components, both λ_q and S need to be known.

2.1.3 Scaling laws of the SOL power decay length

In the last years some progress has been made in the fundamental understanding of what sets the power decay length, with the development of a heuristic model [50] and with implementation of edge gyrokinetic simulations [51, 52]. However, due to the complexity and interconnection of edge and SOL plasma physics, attempts to estimate λ_q based on first principles failed. From the experimental side, a major effort was carried out in 2011 in assembling a multi-machine database of H-mode power decay length data [53], which have been evaluated between type-I ELMs. It was shown that λ_q scales approximately inversely with the poloidal magnetic field at the outer midplane $B_{\text{pol,MP}}$:

$$\lambda_q^{\text{Eich}}\ [\text{mm}] = (0.63 \pm 0.08) \times B_{\text{pol,MP}}^{-1.19\pm0.08}. \tag{2.10}$$

Also, this multi-machine scaling law showed that λ_q is independent of machine size. Considering what was said in section 1.5, i.e. that R needs to be increased to enhance the fusion power in a reactor and that $P_{\text{fus}} \propto R^3$, $\lambda_q \propto R^0$ makes power exhaust in future devices challenging.
More recently, an attempt was made at the Alcator C-Mod tokamak to find a cross-regime (L, I and H-mode) λ_q scaling [54]. It was found that the power decay length exhibits a dependence on volume-averaged core plasma pressure $\overline{p}$ across all confinement regimes analyzed:

$$\lambda_q^{\text{Brunner}}\ [\text{mm}] = (0.91 \pm 0.01) \times (\overline{p}\ [\text{atm}])^{-0.48\pm0.01}. \tag{2.11}$$

In section 5.3 this scaling law will be compared to the results found in this thesis.

2.1.4 Parallel heat conduction in the SOL

In the scrape-off layer, the parallel heat flux is transferred mainly by conduction, while convection can be neglected. This approximation is reasonable when the particle source in the SOL (which then drives the particle flux) is localized in front of the divertor target. By calling $s_{||}$ the parallel coordinate along the SOL, the parallel heat flux conducted in the SOL can be written as:

$$q_{\text{cond}} = -\kappa \frac{\mathrm{d}T}{\mathrm{d}s_{||}} = -\kappa_0 T^{5/2} \frac{\mathrm{d}T}{\mathrm{d}s_{||}}. \tag{2.12}$$

The equation is valid for both electrons and ions, T is the temperature of electrons or ions, and κ is the Spitzer-Härm thermal conductivity for electrons or ions. The constant κ_0 is [55]

$$\kappa_0 = 60 \frac{\sqrt{2\pi}\epsilon_0^2}{e^4 \sqrt{m} Z_{\text{eff}} \ln\Lambda}, \tag{2.13}$$

where ϵ_0 is the electric constant, e is the elementary charge, m is the electron or ion mass, $Z_{\text{eff}} = \sum_j n_j Z_j / n_e$ is the effective charge (n_j and Z_j are the density and the charge number of the ion species j), and $\ln\Lambda$ is the Coulomb logarithm. Typical values of $\ln\Lambda$ and Z_{eff} in the SOL in machines with tungsten as first-wall material are 14 and 1.3, respectively. Due to its mass dependence, κ_0 differs strongly for electrons and ions, with $\kappa_0^e \simeq 2000\,\text{W}/(\text{eV}^{7/2}\text{m})$ and $\kappa_0^i \simeq 60\,\text{W}/(\text{eV}^{7/2}\text{m})$. Therefore, $q_{\text{cond}}^e \gg q_{\text{cond}}^i$ and, if ions and electrons are thermally well coupled in the SOL, one can approximate the total conducted heat flux by the electron component only.
Under such assumptions, Eq. 2.12 can be integrated along $s_{||}$ from an upstream position 'u' to the target position 't'. Upstream is often chosen to be at the outer mid-plane, as in this area the plasma in the confined region is more unstable and therefore more turbulent transport across the separatrix is generated. Equation 2.12 is integrated along the connection length L for two

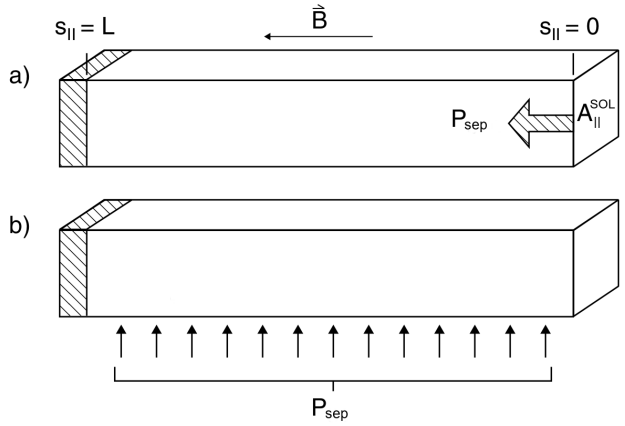

Figure 2.5: (a) All power crossing the separatrix P_{sep} enters the SOL at the upstream position. (b) P_{sep} enters uniformly over the connection length L. Figure adapted from [45].

extreme cases: (a) All of the power crossing the separatrix P_{sep} enters at the upstream position and is conducted without loss to the target, see Fig. 2.5 (a); (b) P_{sep} enters uniformly over length L and is conducted without loss to the target, see Fig. 2.5 (b). For case (a), it is:

$$q_{\mathrm{cond}} = P_{\mathrm{sep}}/A_{||}^{\mathrm{SOL}}. \tag{2.14}$$

By integrating Eq. 2.12 along $s_{||}$ from upstream ($s = 0$) to the target ($s = L$), one finds

$$T_u = \left(T_t^{7/2} + \frac{7}{2} \frac{P_{\mathrm{sep}} L}{A_{||}^{\mathrm{SOL}} \kappa_0} \right)^{2/7} \simeq \left(\frac{7}{2} \frac{P_{\mathrm{sep}} L}{A_{||}^{\mathrm{SOL}} \kappa_0} \right)^{2/7}, \tag{2.15}$$

where $T_u \gg T_t$ (which is often the case) has been used.
For case (b), when P_{sep} enters the SOL uniformly along L, it is:

$$\frac{\mathrm{d}q_{\mathrm{cond}}}{\mathrm{d}s_{||}} = \frac{P_{\mathrm{sep}}}{A_{||}^{\mathrm{SOL}} L}. \tag{2.16}$$

By carrying out the same integration along $s_{||}$ (twice), one finds:

$$T_u = \left(T_t^{7/2} + \frac{7}{4} \frac{P_{\mathrm{sep}} L}{A_{||}^{\mathrm{SOL}} \kappa_0} \right)^{2/7} \simeq \left(\frac{7}{4} \frac{P_{\mathrm{sep}} L}{A_{||}^{\mathrm{SOL}} \kappa_0} \right)^{2/7}. \tag{2.17}$$

Despite the very different assumption on the power distribution entering the SOL, the upstream temperature differs by only a factor of $(1/2)^{2/7} = 0.82$, i.e. 18 %. This remarkable result is due to the very strong temperature dependence of the parallel heat conductivity: small changes in the upstream temperature can accommodate major changes in the power distribution entering the SOL. By inserting Eq. 2.3 in Eq. 2.15 (with $P_{\mathrm{sep}}/A_{||}^{\mathrm{SOL}} = q$), one finds

$$T_e = \left(\frac{7}{2} \frac{q_0 L}{\kappa_0} \right)^{2/7} \exp\left(-\frac{2r}{7 \lambda_q f_x} \right) := T_{e,0} \exp\left(-\frac{r}{\lambda_{T_e} f_x} \right), \tag{2.18}$$

where λ_{T_e} is the electron temperature decay length at the outer midplane and r is the direction perpendicular to the flux surfaces. From Eq. 2.18, the following relation between λ_{T_e} and λ_q is obtained:

$$\lambda_q = \frac{2}{7}\lambda_{T_e}. \tag{2.19}$$

This simple relation was shown to be in good agreement with experimental data of the ASDEX Upgrade tokamak [56, 57].

2.1.5 $\vec{E} \times \vec{B}$ drift flows in the SOL

In the previous section the parallel convective flow of particles has been neglected to build a simple relation between upstream and divertor target conditions. However, particles in the SOL do exhibit a parallel flow, which is in a first approximation directed towards the divertor targets (sinks). In addition to that, due to electric and magnetic fields in the SOL, the $\vec{E} \times \vec{B}$ drift velocity appears. Before discussing these drifts, the so-called "forward" or "reversed" directions of the magnetic field need to be introduced. These directions are conventionally associated with the direction of the ion ∇B drift [55]

$$\vec{v}_{\nabla B} = \frac{v_\perp^2 m}{2eB^3}\vec{B} \times \vec{\nabla} B, \tag{2.20}$$

where $v_\perp$ is the gyroscopic speed and m is the ion mass. In tokamak geometry, $B \propto 1/R$ and therefore $\vec{\nabla} B$ is always directed towards the central axis of the torus. For this reason, the direction of the ion ∇B drift depends purely on the magnetic field direction. When the ion ∇B drift is directed towards the active X-point, the plasma is operated in a configuration termed "favorable" or "forward field", see Fig. 2.6 (a). Conversely, when the ion ∇B drift is directed away from the active X-point, the plasma configuration is called "unfavorable" or "reversed field", see Fig. 2.6 (b). The reason for naming them "favorable" and "unfavorable" will be described in section 3.2.1.
When an electric field $\vec{E}$ is present, plasma particles experience the drift velocity

$$\vec{v}_{\vec{E}\times\vec{B}} = \frac{\vec{E} \times \vec{B}}{B^2}. \tag{2.21}$$

In the following notation it is assumed that $\vec{B}$ is perpendicular to the poloidal plane as $B_t \gg B_p$. Under this assumption $\vec{E} \times \vec{B}$ drifts can be decomposed in a poloidal and radial component.
A poloidal $\vec{E} \times \vec{B}$ drift is due to the presence of radial electric fields across the SOL. Radial electric fields arise in the SOL due to the radial dependence of the SOL plasma potential $V(r) \sim 3T_e(r)/e$ [45]. Using Eq. 2.18, the radial electic field $E_r = -\partial V/\partial r$ can be written as

$$E_r \approx \frac{3T_e}{e\lambda_{T_e}}, \tag{2.22}$$

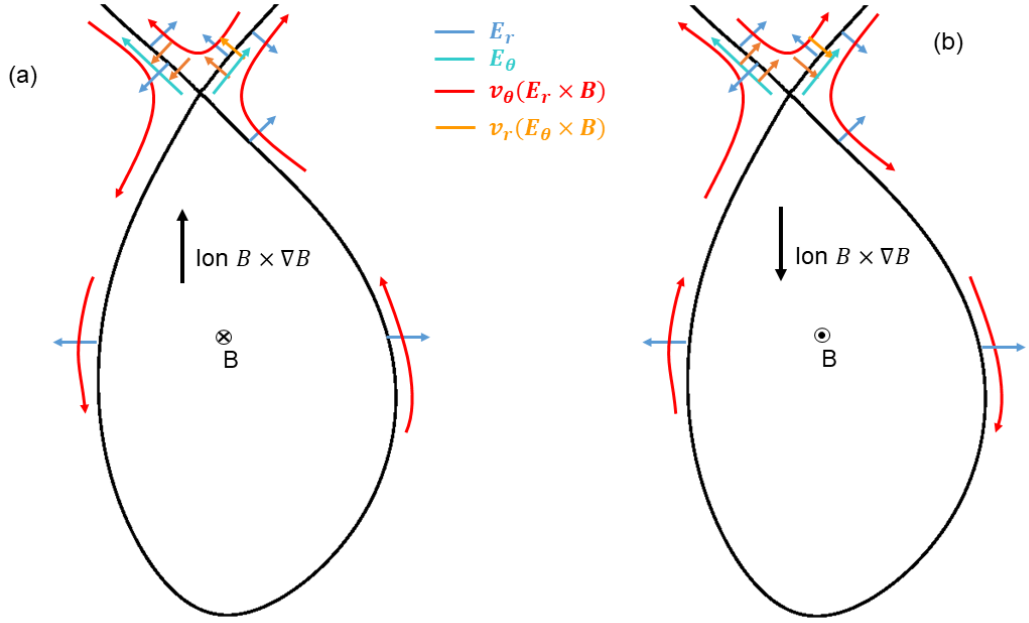

Figure 2.6: Schematic view of poloidal (red) and radial (orange) $E \times B$ drift velocities in favorable (a) and unfavorable (b) configuration, for an USN plasma.

and therefore the resulting poloidal $\vec{E} \times \vec{B}$ velocity is

$$v_{\theta,\vec{E}\times\vec{B}} \approx \frac{3T_e}{e\lambda_{T_e}B}. \tag{2.23}$$

A radial $\vec{E} \times \vec{B}$ drift is due to the presence of a poloidal component of the parallel electric field along the SOL. Parallel electric fields in the SOL are generated due to Ohm's law and are mainly driven by temperature and pressure parallel gradients [45].
In the SOL, $\vec{E}\times\vec{B}$ drift velocities can be comparable to the parallel plasma flow. Moreover, they are charge independent and hence they are able to move the entire plasma in the same direction, influencing the density and temperature distribution in the SOL. Furthermore, the convective $\vec{E} \times \vec{B}$ particle flux

$$\vec{\Gamma}_{\vec{E}\times\vec{B}} = n\frac{\vec{E} \times \vec{B}}{B^2} \tag{2.24}$$

is not divergence-free, i.e. $\vec{\nabla} \cdot \vec{\Gamma}_{\vec{E}\times\vec{B}} \neq 0$. This means that this flow does not close upon itself and, hence, deposits particles and heat onto the divertor targets.
For these reasons, radial and poloidal $\vec{E} \times \vec{B}$ drifts are one of the important players influencing the asymmetry between inner and outer divertor targets, which will be discussed in the next section.

2.1.6 In-out asymmetry in divertor power loads

The energy expelled from the confined region into the SOL can reach the inner and outer divertor targets asymmetrically. Generally, the divertor power load is higher on the outer target than on the inner one. First of all, this is due to a combination of transport and geometrical features of diverted tokamak plasmas. Turbulent transport is localized at the outer midplane and, because of the Shafranov shift (i.e. a radially outward shift of the magnetic axis), outboard flux surfaces are compressed leading to increased local gradients. As a consequence, a larger fraction of the power crosses the separatrix from the outer midplane. For this reason, the power is conducted along different distances in the SOL to reach the outer and inner divertor targets, with $L_{\mathrm{inn}} > L_{\mathrm{out}}$, where L is the connection length from the outer midplane to the targets. Since integrating Eq. 2.12 from the inner or the outer target to the outer midplane must yield the same upstream temperature T_u, from Eq. 2.15 it follows

$$\frac{q_{\mathrm{out}}}{q_{\mathrm{inn}}} = \frac{L_{\mathrm{inn}}}{L_{\mathrm{out}}}, \tag{2.25}$$

which leads to $q_{\mathrm{out}} > q_{\mathrm{inn}}$ for $L_{\mathrm{inn}} > L_{\mathrm{out}}$. In addition to that, divertor asymmetries are influenced by $\vec{E} \times \vec{B}$ drifts in the SOL [45]. In forward-field configuration, those drifts contribute to make the outer target electron temperature larger than the inner one, see Fig. 2.6 (a), and thus to make the inner-outer power ratio larger.

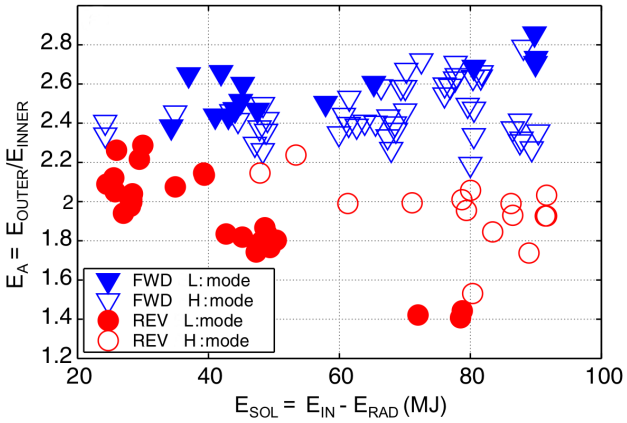

Figure 2.7: Energy ratio between outer and inner divertor targets against the energy entering the SOL in the JET tokamak for L-mode (filled symbols) and H-mode (empty symbols) discharges. Blue and red colors indicate forward and reversed field configurations, respectively. Figure adapted from [58].

Figure 2.7 shows the energy ratio between outer and inner divertor targets against the energy entering the SOL in the JET tokamak. Measurements were performed with target tile embedded thermocouples which provide a shot-integrated estimate of the integral energy deposition on each tile for each discharge. L-mode and H-mode discharges in forward-field configuration exhibit

a large asymmetry in favor of the energy E on the outer target ($E_{\mathrm{out}}/E_{\mathrm{in}} = 2.2-3$). Note also that H-mode discharges show a lower ratio $E_{\mathrm{out}}/E_{\mathrm{in}}$ w.r.t. L-mode ones. As shown in section 2.2.7, this is due to the different in-out asymmetries during type-I ELMs [59].
The effect of $\vec{E} \times \vec{B}$ drifts on divertor asymmetries can be clearly seen when the direction of the toroidal field is reversed, i.e. in unfavorable configuration. In this case, $\vec{E} \times \vec{B}$ drifts contribute to make the inner target electron temperature larger than the outer one, see Fig. 2.6 (b), and thus they tend to make $E_{\mathrm{out}}/E_{\mathrm{in}}$ more even. This effect is shown again in Fig. 2.7, where the L-mode $E_{\mathrm{out}}/E_{\mathrm{in}}$ can reach 1.4. Also, reversed-field H-mode discharges exhibit larger out-in ratios than L-mode ones. This is again due to type-I ELMs in H-mode, which carry energy preferentially to the outer target.

2.2 Transient divertor power loads

Transient divertor power loads are caused by any event that expels plasma from the confined region into the SOL such that the steady-state heat flux is temporarily increased. An example of such events are Edge Localized Modes (ELMs) occurring in H-mode plasmas. The sudden outflow of plasma from the confined region into the SOL leads to a transient increase of the heat flux onto the divertor target plates, which in turns causes the divertor target surface temperature to rise transiently. As ELMs occur periodically, the divertor target surface temperature will undertake periodic increases. The associated fatigue stress reduces considerably the lifetime of the divertor target plates. In the following subsection, a detailed description of ELMs is given. Basic quantities and models to characterize divertor transient thermal loads are introduced in the consecutive sections.

2.2.1 Edge localized modes (ELMs)

As already outlined in section 1.4, ELMs are divided into three main categories [25]. This classification is based on their frequency of occurrence f_{ELM}, on the presence of magnetic precursors, and on the MHD stability of the edge profile w.r.t. the ideal peeling-ballooning criterion [60]. The number of each ELM type is just a historical convention, based on the order in which different types of ELM were first discovered.

- Type-I ELMs exhibit increasing frequency with increasing heating power. The edge profile is close to the ideal peeling-ballooning stability boundary [61]. They also exhibit a magnetic precursor occurring before the onset of the event [62–64].

- Type-II ELMs occur in discharges with plasma cross section that exhibits high triangularity and elongation, with large gas puff (i.e. high separatrix

density [65]), and with good energy confinement [66, 67]. Magnetic precursor oscillations can be also observed before the onset of the event [66]. They have an about 10 times smaller energy loss w.r.t. type-I ELMs.

- Type-III ELMs exhibit decreasing frequency with increasing heating power. They usually appear after the L-H transition or at high density [68, 69]. They occur in plasmas with lower energy confinement w.r.t. that observed during type-I and type-II ELMs [69]. A coherent magnetic precursor oscillation with a frequency of $50-70\,\mathrm{kHz}$ is observed before the onset of the event. They have similar ELM energy losses as type-II ELMs.

2.2.2 ELM energy and particle loss

The energy and particle losses during ELMs are important quantities to describe the size of such events. They are defined as:

$$\Delta W_{\mathrm{ELM}} = \frac{3}{2}\int \Delta p \,\mathrm{d}V \tag{2.26}$$

$$\Delta N_{\mathrm{ELM}} = \int \Delta n_e \,\mathrm{d}V, \tag{2.27}$$

where ΔW and ΔN indicate the energy and particle losses, respectively, V is the plasma volume, $p = p_i + p_e$ is the total pressure of the plasma with p_i and p_e being the ion and electron pressures, n_e is the electron density, and Δ indicates the difference between the radial profiles before and after an ELM. Energy losses are normalized either to the total energy content of the plasma W_{MHD} (which is evaluated from the reconstructed MHD equilibrium) or to the pedestal energy content W_{ped}, defined as

$$W_{\mathrm{ped}} = \frac{3}{2} p_{\mathrm{ped}} V_{\mathrm{plasma}}, \tag{2.28}$$

where p_{ped} is the total pressure of the plasma at the pedestal top position and V_{plasma} is the total plasma volume. Particle losses are usually normalized to the pedestal particle content N_{ped}, defined as

$$N_{\mathrm{ped}} = n_{\mathrm{e,ped}} V_{\mathrm{plasma}}, \tag{2.29}$$

where $n_{\mathrm{e,ped}}$ is the electron density at the pedestal top position.
A previous multi-machine study on type-I ELMs revealed that the relative ELM energy losses scale with the pedestal collisionality [70], which is defined as:

$$\nu^*_{\mathrm{ped}} = R q_{95} \epsilon^{-3/2} (\lambda_{\mathrm{e,e}})^{-1}, \tag{2.30}$$

where $\epsilon = 1/A = a/R$ is the inverse aspect ratio, q_{95} is the safety factor at $\rho_{\mathrm{pol}} = 0.95$, and $\lambda_{\mathrm{e,e}} = 1.7 \times 10^{17}\, T^2_{\mathrm{e,ped}}\,(\mathrm{eV})/(n_{\mathrm{e,ped}}\,(\mathrm{m}^{-3})\ln\Lambda)$ is the electron-electron Coulomb collision mean free path at the pedestal top position. The

Coulomb logarithm $\ln\Lambda$ is evaluated here following the classical formula for electron-electron collisions [71] and using plasma parameters at the pedestal top position.
By writing $p_x = n_x T_x$ where the subscript 'x' refers to ions or electrons, the energy loss can be further broken down into two contributions, termed conductive and convective energy losses (ΔW_{cond} and ΔW_{conv}), which are defined as:

$$\Delta W_{\mathrm{ELM}} = \frac{3}{2}\int (\Delta p_e + \Delta p_i)\ \mathrm{d}V =$$
$$= \frac{3}{2}\sum_{e,i}\left(\int n_x \Delta T_x\,\mathrm{d}V + \int T_x \Delta n_x\,\mathrm{d}V - \int \Delta T_x \Delta n_x\,\mathrm{d}V\right) =$$
$$= \Delta W_{\mathrm{cond}} + \Delta W_{\mathrm{conv}} - \Delta W_{\mathrm{cross}}. \tag{2.31}$$

The cross-term $\Delta W_{\mathrm{cross}}$ is often neglected, as it is of second order. Breaking down the energy loss into a conductive and convective term is important, since these two contributions may behave and scale differently to larger devices. Indeed, for type-I ELMs it has been shown that convective ELM energy losses have a weak dependence on pedestal plasma parameters [72], while conductive ELM energy losses show clear trends with pedestal quantities such as ν^*_{ped}.

2.2.3 ELM filaments: quasi mode number

During ELMs, 3D plasma structures called 'filaments' generate and propagate in the SOL, carrying particle and energy towards the plasma facing components of the main chamber and the divertor target plates [73–75]. Their name comes from the fact that these structures are extended along the magnetic field lines, thereby forming 3D helical filaments [76–78]. When filaments reach the divertor target plates, they form spiral heat flux patterns onto the divertor targets [73], see e.g. Fig. 2.8. These patterns can be interpreted as the result of plasma filaments that are generated at the outer midplane at different torodial locations and that propagate in the SOL in the parallel B-field direction until they hit the divertor targets. Field line tracing of magnetic flux bundles that start at the outer midplane at different toroidal locations reproduce the spiral pattern observed experimentally on the divertor target. In this way, a subset of toroidally displaced origins of energy release at the outer midplane can be identified for each ELM. A quasi mode number can be associated to such toroidal asymmetric energy effluxes reconstructed with field line tracing [74]:

$$n_{\mathrm{QMN}} = \frac{1}{M}\sum_{j}^{M}\frac{2\pi}{\phi_j - \phi_{j+1}}, \tag{2.32}$$

where M is the total number of stripes detected, j is the index indicating each stripe, and ϕ represents the toroidal angle at which flux bundles originate in the outer midplane. For type-I ELMs, n_{QMN} is in the range $5-20$ [73, 75, 79].

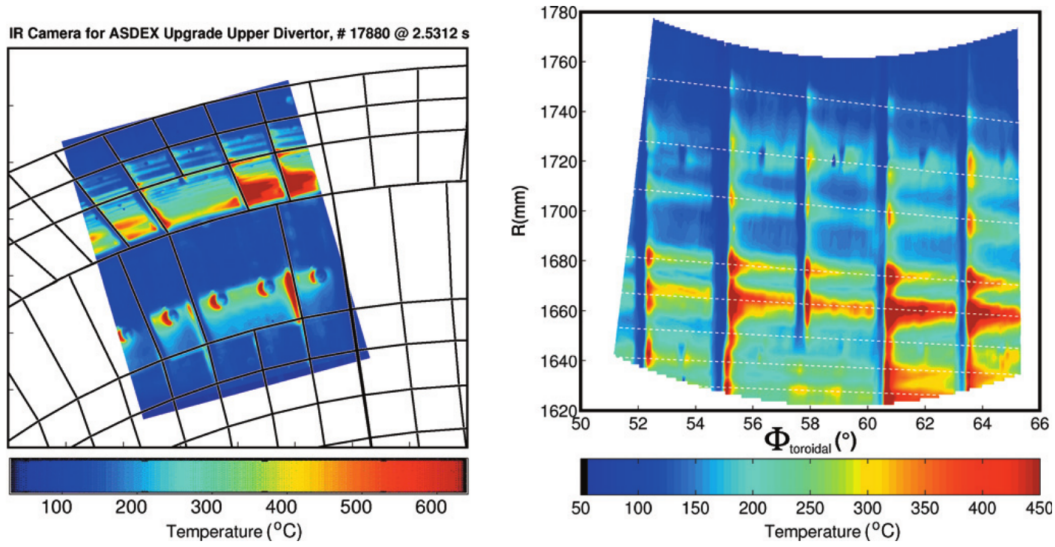

Figure 2.8: (Right) Divertor surface temperature pattern on the ASDEX Upgrade upper divertor targets during a type-I ELM measured with an infrared camera. (Left) Same pattern mapped to target coordinates. Dashed lines represent the intersection structure of eight radial flux bundles (sets of field lines) started at distinct toroidal positions in the outer midplane. Figure from [74].

2.2.4 Heat impact factor

A key quantity to evaluate the thermomechanical stress induced in the divertor target material is the surface temperature rise due to a transient event (e.g. an ELM). The surface temperature rise ΔT_{surf} due to a constant heat flux q over a depositon time τ_{dep} in a 1D semi-infinite slab geometry is [80]:

$$\Delta T_{\mathrm{surf}} = \frac{2}{\sqrt{\pi} b} q \sqrt{\tau_{\mathrm{dep}}} = \frac{2}{\sqrt{\pi} b} \frac{\epsilon}{\sqrt{\tau_{\mathrm{dep}}}} \propto \frac{\epsilon}{\sqrt{\tau_{\mathrm{dep}}}}, \tag{2.33}$$

where $b = \sqrt{\kappa \rho c_{\mathrm{p}}}$ is the thermal effusivity of the material (κ, ρ and c_{p} are the material conductivity, density and specific heat capacity, respectively), and $\epsilon = q \cdot \tau_{\mathrm{dep}}$ is the energy fluence (for a constant heat flux q). The surface temperature rise described by Eq. 2.33 is also called 'heat impact factor'. Equation 2.33 shows that thermomechanical stresses induced by transient events depend mainly on

- the deposition time of the transient event τ_{dep}
- and the energy fluence onto the material surface ϵ.

These two quantities, along with models to predict them, will be described in the following subsections.

2.2.5 Deposition time

The deposition time of a transient event is defined according to the temporal evolution of the power reaching the divertor target. Figure 2.9 shows examples of different temporal evolutions (and so deposition times) during ELMs. Three

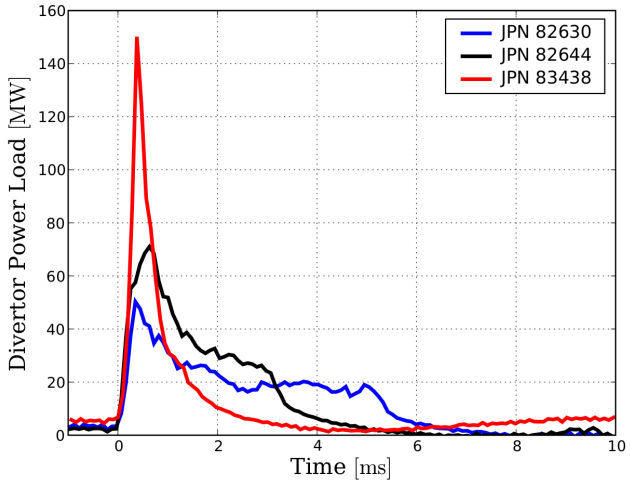

Figure 2.9: Time evolution of the power reaching the divertor target during different ELMs in the JET tokamak. Figure from [81].

different time instants of the power load evolution $P_{\mathrm{div}}(t)$ are defined: The beginning time t_{beg}, the time at the maximum t_{max} and the ending time t_{end}, with

$$P_{\mathrm{div}}(t_{\mathrm{max}}) = P_{\mathrm{div,max}}. \tag{2.34}$$

The beginning time is defined as the time instant when the divertor power takes $1/(10\,\mathrm{e})$ of its peak value for $t < t_{\mathrm{max}}$:

$$P_{\mathrm{div}}(t_{\mathrm{beg}}) = \frac{1}{10\,\mathrm{e}} P_{\mathrm{div,max}}, \qquad \text{for } t < t_{\mathrm{max}}. \tag{2.35}$$

Finally, the ending time is defined as the time instant when the divertor power takes $1/\mathrm{e}$ of its peak value for $t > t_{\mathrm{max}}$:

$$P_{\mathrm{div}}(t_{\mathrm{end}}) = \frac{1}{\mathrm{e}} P_{\mathrm{div,max}}, \qquad \text{for } t > t_{\mathrm{max}}. \tag{2.36}$$

We can now define the deposition time τ_{dep}, the rise time τ_{rise} and the decay time τ_{decay} as:

$$\tau_{\mathrm{rise}} = t_{\mathrm{max}} - t_{\mathrm{beg}} \tag{2.37}$$

$$\tau_{\mathrm{decay}} = t_{\mathrm{end}} - t_{\mathrm{max}} \tag{2.38}$$

$$\tau_{\mathrm{dep}} = t_{\mathrm{end}} - t_{\mathrm{beg}} = \tau_{\mathrm{rise}} + \tau_{\mathrm{decay}} \tag{2.39}$$

For type-I ELMs, a correlation was found between τ_{rise} and the ion parallel transport time [82, 83] $\tau_{||}$:

$$\tau_{||} = \frac{L}{c_s} \simeq \frac{2\pi q_{95} R}{\sqrt{(T_e + T_i)/m_i}}, \tag{2.40}$$

where L is the connection length, c_s is the sound speed, T_e and T_i are the electron and ion temperature at the pedestal top, and m_i is the ion mass. This correlation is in agreement with PIC simulations [84], which suggest that ion convective transport along open field lines during type-I ELMs carries a large amount of energy to the divertor target. The decay time of type-I ELMs is a factor 3−5 larger than the rise time [85].
The temporal evolution of the power reaching the divertor target has been successfully reproduced with the "free-streaming-particle" model [86]. This model assumes that a Maxwellian distribution of plasma particles is released over a short time $\delta(t)$ compared to the SOL parallel transport times and in a short parallel distribution length $\delta(l)$ compared to the parallel connection lengths to the target. These particles propagate in a force-free way along the SOL in the parallel direction. The power reaching the divertor targets can be thus described by the following equation:

$$P(t) = \frac{2E}{3\sqrt{\pi}} \left[1 + \left(\frac{\tau}{t}\right)^2\right] \frac{\tau}{t^2} \exp\left[-\left(\frac{\tau}{t}\right)^2\right] + P_{\text{BG}}, \tag{2.41}$$

where E is the total energy reaching the divertor, τ is the characteristic decay time and P_{BG} is the background power. This equation reproduces the temporal shape of conditionally averaged ELM power loads onto the divertor target, as Fig 2.10 shows.

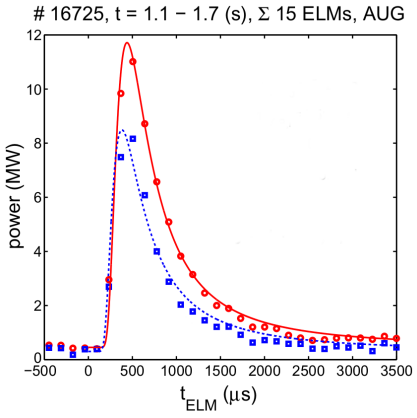

Figure 2.10: Time evolution of the power reaching the upper inner (red circles) and outer (blue squares) divertor targets in the ASDEX Upgrade tokamak. Data are fit with Eq. 2.41. Figure adapted from [87].

2.2.6 Energy fluence

The energy fluence is defined as the time integration of the heat flux over the deposition time of the transient event:

$$\epsilon_{\perp}(s) = \int_{t_{\mathrm{beg}}}^{t_{\mathrm{end}}} q_{\perp}(t, s)\, \mathrm{d}t, \tag{2.42}$$

where $q_{\perp}$ is the perpendicular heat flux reaching the divertor target. Note that $q_{\perp}(t, s)$ is a function of time and space, and s is the spatial coordinate along the divertor target plate (see Eq. 2.6). To allow cross-machine comparisons, divertor geometrical effects must be taken into account, hence the energy fluence parallel to the magnetic field lines is considered. Also, in order to take into account only the energy fluence associated to the transient event, the inter-ELM heat flux q_0 is subtracted from the perpendicular heat flux reaching the divertor target during the transient event. This subtraction introduces little modifications in large machines, but it needs to be taken into account in small or medium-size machines, where q_0 could account for more than 50 % of the total heat flux during the transient event. Therefore, the parallel energy fluence is calculated as:

$$\epsilon_{||}(s) = \int_{t_{\mathrm{beg}}}^{t_{\mathrm{end}}} \frac{q_{\perp} - q_0}{\sin(\alpha_{\mathrm{div}})}\, \mathrm{d}t, \tag{2.43}$$

where α_{div} is the angle between the magnetic field lines and the divertor target. In this way, an energy fluence profile $\epsilon_{||}(s)$ that represents only the additional energy expelled by the transient event is obtained. An example of such energy fluence profiles at the divertor target is shown in Fig. 2.11. The typical steady-

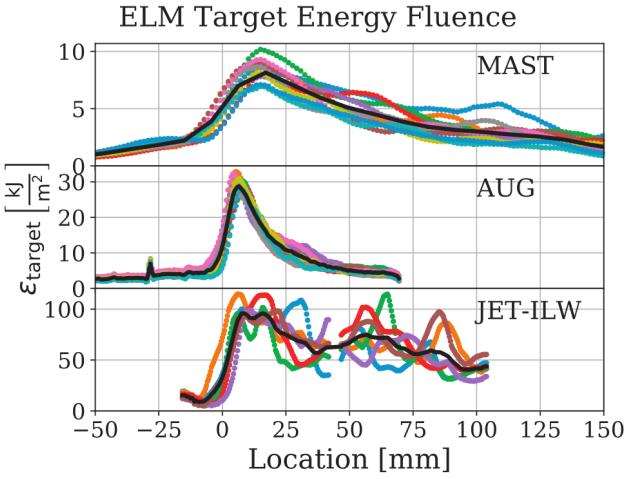

Figure 2.11: ELM energy fluence profiles at the outer divertor targets of three different devices, which are MAST, ASDEX Upgrade and JET from top to bottom. Data are inferred from infrared camera measurements. The black line represents the averaged profile over several ELMs. Figure from [26].

state profile (see e.g. Fig. 2.4) is modified by the presence of additional sub-peaks in the far-SOL, which are due to the additional filamentary transport during ELMs.
To assess thermomechanical fatigue or brittle limits, the quantity of interest is the maximum of the energy fluence profile. Therefore, scaling and modelling attempts have been focused on predicting this quantity.
A semi-empirical model to describe the divertor peak energy fluence has been introduced in [26]. This model is a power balance of a toroidally uniform volume of small width around the pedestal top position. It is assumed that this volume connects to the divertor target plates due to ergodization of magnetic field lines. In such a situation, the energy contained in such a volume is entirely transported to the divertor target. Under these assumptions, the following expression for the peak parallel energy fluence is derived:

$$\epsilon_{||,\mathrm{model}} = \Delta_{\mathrm{equi}} 2\pi a \sqrt{\frac{1+\kappa^2}{2}} \frac{3}{2} p_{e,\mathrm{ped}} \frac{B_{\mathrm{t}}^{\mathrm{MP}}}{B_{\mathrm{p}}^{\mathrm{MP}}} \tag{2.44}$$

where the superscript "MP" stands for outer midplane, B_{t} and B_{p} are the toroidal and poloidal components of the magnetic field, $p_{e,\mathrm{ped}}$ is the pedestal top electron pressure, a is the minor radius, κ is the plasma elongation and Δ_{equi} is a geometrical factor derived by comparison of the assumed elliptical plasma shape to the real equilibrium reconstruction (typically 2.0).
Figure 2.12 shows multi-machine data of the type-I ELM peak parallel energy fluence against the prediciton of the model. The model represents a lower boundary for type-I ELM data, while an upper purely empirical boundary is found by multiplying the model by a factor of three. Data used in such study were mainly from the outer divertor target. Figure 2.12 shows also the projections to ITER according to the model boundaries.

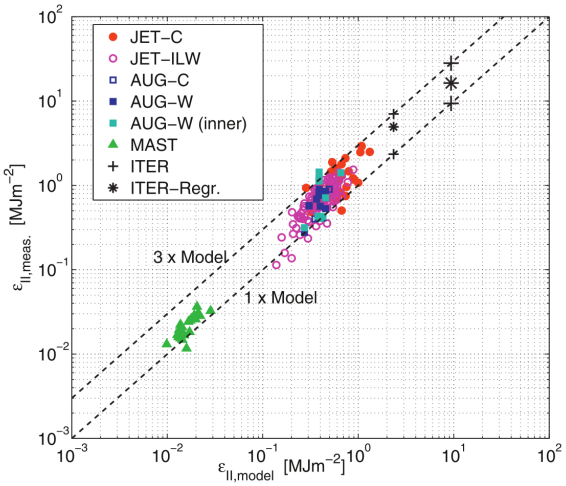

Figure 2.12: Experimental values of the parallel peak energy fluence against the value predicted by Eq. 2.44. Data from different tokamaks (JET, ASDEX Upgrade and MAST) are shown, along with projections to ITER. Figure from [26].

For the baseline $Q = 10$ burning plasma scenario, the predicted parallel energy fluences due to type-I ELMs are above the material limits of the ITER divertor [26]. The ITER divertor material limit has been found after exposure of ITER divertor monoblocks to 10^5 cycles of 500 µs-long transient events [88], and corresponds to a deposited energy fluence limit of about $0.3\,\mathrm{MJ/m^2}$. A most recent study that took into account geometrical effects of the ITER divertor castellated structure further lowered this limit to $\epsilon_{\perp,\mathrm{lim}} = 0.15\,\mathrm{MJ/m^2}$ [89].

2.2.7 In-out energy asymmetry

During transient events divertor energy in-out asymmetries differ from those during steady-state heat loads. In the favorable configuration, during type-I ELMs more energy reaches the inner divertor target plate, i.e. $E_{\mathrm{ELM}}^{\mathrm{outer}} < E_{\mathrm{ELM}}^{\mathrm{inner}}$. This is shown in Fig. 2.13 for the ASDEX Upgrade and JET tokamaks. On the other hand, in unfavorable configuration, more energy reaches the outer divertor target plate during type-I ELMs, i.e. $E_{\mathrm{ELM}}^{\mathrm{outer}} > E_{\mathrm{ELM}}^{\mathrm{inner}}$. The reason for such behavior during transient events is to date unknown. A proposal to explain this asymmetry has been outlined in Ref. [87] based on the free-streaming-particle model.

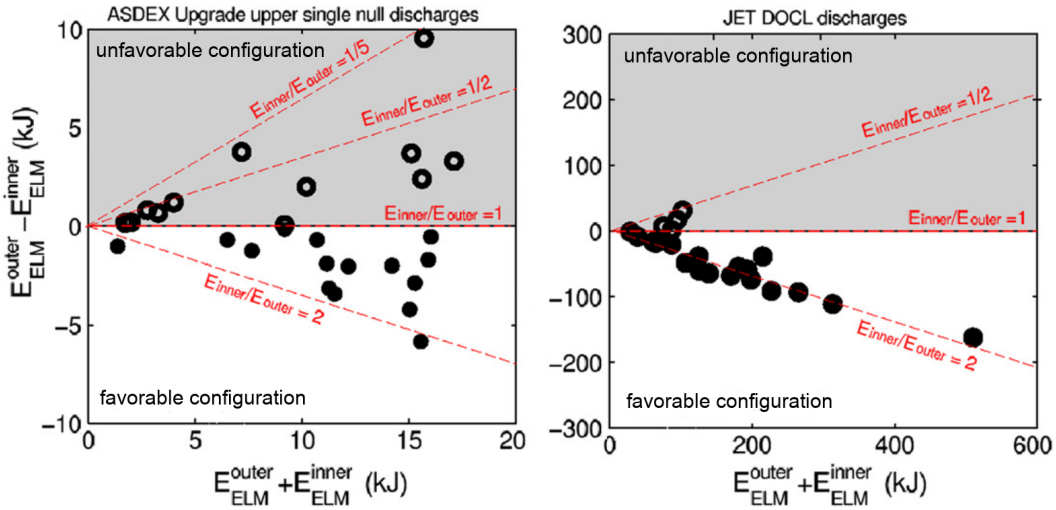

Figure 2.13: ASDEX Upgrade (left) and JET (right) ELM energy in-out asymmetry against the total ELM energy reaching the divertor targets. Closed and open symbols represent discharges in favorable and unfavorable configuration, respectively. Figure from [90].

Chapter 3

Plasma edge in different confinement regimes

In this chapter, the main characteristics of edge plasma parameters in different confinement regimes are introduced. After describing L-mode, H-mode and I-phase plasmas, particular attention is given to the I-mode confinement regime, as it is the main focus of this thesis.

3.1 L-mode, H-mode and I-phase

The low confinement mode (L-mode) is a plasma confinement regime where density and temperature profiles are moderately steep at the plasma edge, as shown in Fig. 3.1 (a) and (d). Energy and particle confinement times of L-mode discharges are low. In L-mode plasmas the edge region is dominated by turbulent transport.
When additional external heating power is added to the plasma, a transition to the high-confinement mode (H-mode) can occur [22]. In this regime, the fluctuation level that drives turbulent transport at the plasma edge is strongly reduced, and a so-called edge transport barrier (ETB) is formed. In this way, both energy and particle confinement times increase [22]. The reduction of turbulent transport in the ETB region leads to the formation of steep edge gradients of plasma temperature and density, as shown in Fig. 3.1 (c) and (f). This region is called pedestal.
To qualify the energy confinement of an H-mode plasma, it is common to normalize the energy confinement time τ_E to that given by a multi-machine scaling law called IPB98(y,2) [40]

$$H_{98} \coloneqq \frac{\tau_E}{\tau_{E,\mathrm{IPB98}}}. \tag{3.1}$$

The IPB98(y,2) scaling law was derived from H-mode discharges. For this reason, H-mode plasmas usually exhibit $H_{98} \approx 1$. Although H_{98} has been

introduced to describe H-mode plasmas, it is often used as a confinement indicator for L-mode plasmas as well. L-mode plasmas usually exhibit $H_{98} \approx 0.6$.

H-mode and L-mode plasmas do not only exhibit differences in the energy confinement and ETB formation. When the plasma transits into H-mode also near-SOL gradients change. This can be seen in Fig. 3.1 by comparing L-mode and H-mode SOL profiles, and further details will be presented in chapter 5. Both near-SOL T_e and n_e gradients become steeper in H-mode than in L-mode [56, 91]. Due to the relationship between temperature and power SOL gradients, see e.g. Eq. 2.19, this affects the SOL power decay length λ_q as well. Indeed, in H-mode plasmas λ_q has about half the value of that in L-mode plasmas [92, 93]. A smaller value of λ_q in H-mode implies higher peak heat fluxes on the divertor.

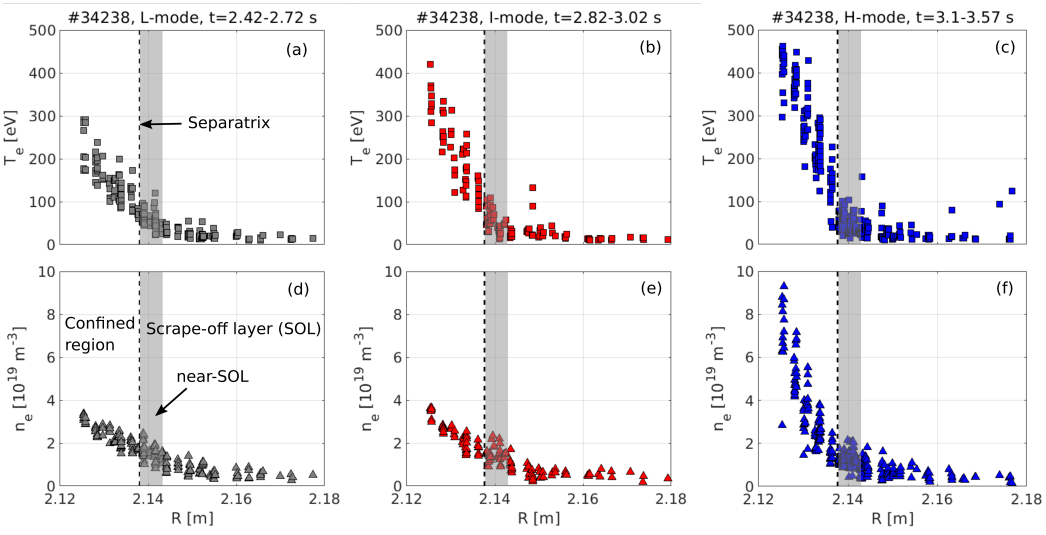

Figure 3.1: Electron temperature (top) and electron density (bottom) edge profiles during the L-mode (left), I-mode (center) and H-mode (right) confinement regimes in the ASDEX Upgrade tokamak. The gray area represents the near-SOL region.

Another plasma state that will be mentioned during this thesis is the so-called "intermediate phase" or I-phase [94, 95], which appears at the transition from L-mode to H-mode in favorable configuration. Before discussing I-phase characteristic, a short digression on L-H transition physics is needed. First of all, it should be mentioned that up to now it is not fully understood what exactly leads to the H-mode transition. For a review of different theories see Ref. [96]. However, many theories suppose a two-step process leading to the L-H transition: 1) the formation of radial electric field E_r with large gradients in the edge region and 2) the consequent formation of a $\vec{E} \times \vec{B}$ velocity shear that suppresses edge turbulence, leading to the pedestal build-up.
In the transition phase from L to H-mode, the $\vec{E} \times \vec{B}$ velocity shear can increase and decrease periodically, leading to oscillations between L-mode and H-mode. This transition phase is called I-phase. The oscillation from L to

H-mode affects the edge profiles as well, which periodically build up and relax the gradients [97, 98]. As a consequence, bursts of energy are expelled from the confined region into the SOL. In ASDEX Upgrade a further distinction between two different I-phase periods has been introduced [99]: An "early" I-phase, where oscillations are regular, and a "late" I-phase, where these oscillations evolve into more intermittent bursts. The oscillations in the early I-phase show a precursor which is detectable only by reflectometry and not by magnetic pick-up coils[1] [99]. Conversely, the bursts in the late I-phase exhibit a precursor which is detected by both magnetic pick-up coils and reflectometry. For this reason, they have been identified as type-III ELMs [99]. These features of I-phase will be compared to the I-mode pedestal relaxation events analyzed in this thesis. The I-phase is not to be confused with the I-mode confinement regime, which will be described in the next section.

3.2 I-mode

The I-mode is a high energy confinement regime free of type-I ELM. As already outlined in section 1.4, I-mode plasmas feature a temperature pedestal at the plasma edge, while the density profile remains similar to that of L-mode, see Fig. 3.1 (b) and (e). As a consequence, they have L-mode-like particle and impurity confinement times [38], while the energy confinement time is H-mode-like. This combines the desired properties of L-mode and H-mode plasmas, namely reduced impurity (and helium ash) accumulation, and the achievement of high core plasma pressure. The operational space and other characteristics of the I-mode related to plasma edge physics are described in the next sections.

3.2.1 Operational domain

I-mode plasmas are usually achieved in the unfavorable (or reversed-field) configuration, i.e. when the ion ∇B drift points away from the active magnetic X-point. By choosing the appropriate B-field direction, these plasmas can be achieved in both the upper and lower single null (USN and LSN) configuration in a broad range of plasma shapes [100]. In the Alcator C-Mod (C-Mod) tokamak, few I-mode plasmas have also been achieved in favorable configuration, when the ion ∇B drift points towards the active X-point [37, 101]. Those I-mode plasmas were obtained only using a particular LSN shape, with the separatrix approaching the vessel on the high-field side. As most of I-mode plasmas are achieved only in the unfavorable configuration, we will turn our attention to these.
In the reversed-field configuration, the power threshold needed to access H-mode increases by approximately a factor 1.5–2.5 [101, 102], i.e. it is 'unfavorable' in terms of H-mode access. The I-mode confinement regime appears

[1] Magnetic pick-up coils and reflectometry are described in sections 4.4.9, respectively.

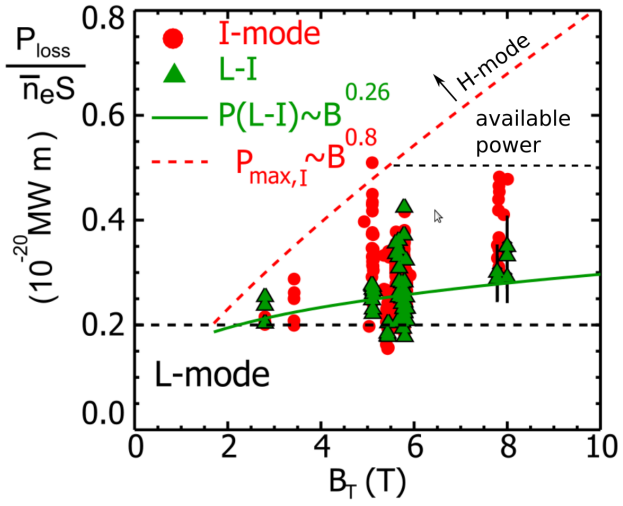

Figure 3.2: Loss power at L-I transition (green triangles) and in I-mode plasmas (red circles), normalized by line-averaged electron density and plasma surface area for the Alcator C-Mod tokamak. Solid green line represents the regression fit of data at the L-I transition. Figure adapted from [100].

exactly in this power window opened up by the higher H-mode access in unfavorable configuration. A multi-machine scaling law of the H-mode power threshold P_{LH} [103] revealed that P_{LH} scales with the line-averaged electron density $\overline{n}_e$, toroidal magnetic field strength B_{t} and the plasma surface S:

$$P_{\mathrm{LH}} \propto \overline{n}_e^{0.7} B_{\mathrm{t}}^{0.8} S^{0.9}. \tag{3.2}$$

Therefore, for the same plasma surface and line-averaged density, the power needed to enter H-mode increases almost linearly with the toroidal magnetic field strength. At the same time, the power needed to access I-mode P_{LI} was found to scale weakly with the toroidal magnetic field strength in both the Alcator C-Mod [100] and the ASDEX Upgrade tokamak [104]:

$$P_{\mathrm{LI}}^{\mathrm{C\text{-}Mod}} \propto B_{\mathrm{t}}^{0.26} \tag{3.3}$$

$$P_{\mathrm{LI}}^{\mathrm{AUG}} \propto B_{\mathrm{t}}^{0.39} \tag{3.4}$$

Figure 3.2 shows the loss power ($P_{\mathrm{loss}} = P_{\mathrm{heat}} - \mathrm{d}W/\mathrm{d}t$, where P_{heat} is the heating power and W is the plasma stored energy) normalized to the line-averaged electron density and the plasma surface during different I-mode plasmas in Alcator C-Mod. While P_{LI} is proportional to $B_{\mathrm{t}}^{0.26}$, the highest power at which the discharges stay in I-mode increases with $B_{\mathrm{t}}^{0.8}$, which is consistent with the B_{t} dependence of P_{LH}. A further increase of the heating power brings a transition to H-mode. Therefore, the I-mode existence power window broadens at higher magnetic fields. The data at $B_{\mathrm{t}} = 8\,\mathrm{T}$ shown in Fig. 3.2 is limited by the available external heating power installed on Alcator C-Mod and in unfavorable configuration, no H-mode plasmas at $B_{\mathrm{t}} = 8\,\mathrm{T}$ have been accessed.

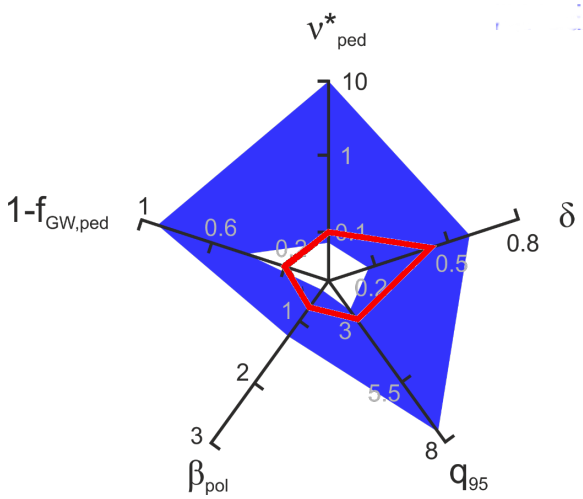

Figure 3.3: Existence diagram of I-mode plasmas. The five axes represent the pedestal collisionality ν^*_{ped}, triangularity δ, q_{95}, β_{pol}, and $1-f_{\mathrm{GW,ped}}$, with $f_{\mathrm{GW,ped}}$ being the Greenwald pedestal fraction. The blue area spans the values assumed by I-mode plasmas in the ASDEX Upgrade and Alcator C-Mod tokamaks. The red pentagon represents the ITER target values [17]. Figure adapted from [27].

Once the plasma is heated in the prescribed power range, I-mode plasmas can exist in a broad range of parameters. The star chart in Fig. 3.3 shows five quantities which are relevant for ITER [17]: the pedestal top collisionality ν^*_{ped} (Eq. 2.30), the plasma triangularity δ, the safety factor q_{95} at $\rho_{\mathrm{pol}} = 0.95$, the poloidal beta $\beta_{\mathrm{pol}} = \overline{p}/(B^2_{\mathrm{pol}}/2\mu_0)$, where $\overline{p}$ is the averaged plasma pressure and B_{pol} is the average poloidal magnetic field strength, and the pedestal Greenwald fraction $f_{\mathrm{GW,ped}} = n_{\mathrm{e,ped}}/n_{\mathrm{GW}}$, with $n_{\mathrm{e,ped}}$ being the electron density at the pedestal top and $n_{\mathrm{GW}} = I_p/(\pi a^2)$. Note that the distance of the pedestal Greenwald fraction to unity $(1-f_{\mathrm{GW,ped}})$ is plotted here. The plasma triangularity is the average of the upper and lower triangularity δ_{up} and δ_{low}. The upper and lower triangularity are defined as $\delta_{\mathrm{up}} = (R_{\mathrm{geo}} - R_{\mathrm{up}})/a$ and $\delta_{\mathrm{low}} = (R_{\mathrm{geo}} - R_{\mathrm{low}})/a$, where R_{geo} is the geometrical major radius, and R_{up} and R_{low} are the radii at the upper and lower most points of the separatrix, respectively. The ITER target values [17] are highlighted in red. I-mode plasmas cover a wide area in particular in ν^*_{ped}, δ, q_{95} and $f_{\mathrm{GW,ped}}$; however, they did not achieve the high Greenwald fraction required for ITER ($f_{\mathrm{GW,ped}} = 0.8$) yet. It should be noted that some of these parameters cannot be obtained simultaneously in present-day machines. An example is the combination of high Greenwald fraction with low pedestal top collisionality, with the latter being achieved only at low density (and thus low $f_{\mathrm{GW,ped}}$) in present-day machines.

3.2.2 Edge transport characteristics

A key feature of I-mode discharges is a suppression of low-frequency turbulent density fluctuations, and the simultaneous appearance of a weakly coherent

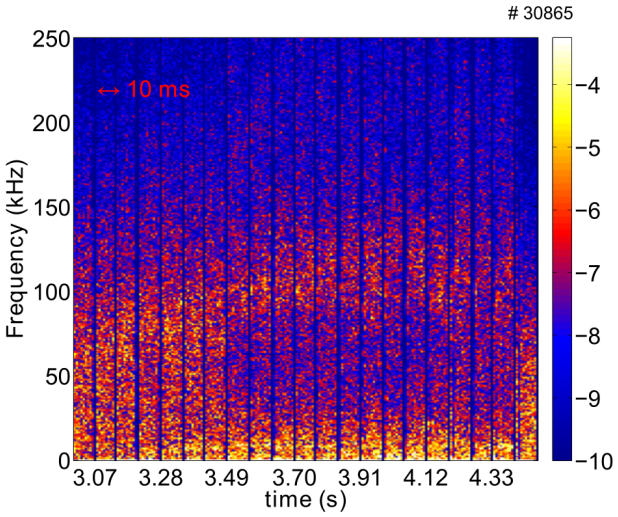

Figure 3.4: Spectrogram of density fluctuations from hopping reflectometry during an ASDEX Upgrade discharge in unfavorable configuration. Amplitudes are shown in logarithmic scale. When the plasma enters the I-mode regime ($t \simeq 3.5\,\mathrm{s}$), the WCM appears, peaking at $f = 120\,\mathrm{kHz}$. Figure from [105].

mode (WCM) at higher frequencies ($f \approx 80$–$300\,\mathrm{kHz}$) [37, 105–107]. An example of the development of the WCM during the L-I transition in an AUG discharge is shown in Fig. 3.4, where the spectrogram of density fluctuations from reflectometry[2] is displayed. At the onset of the I-mode ($t \simeq 3.5\,\mathrm{s}$), a reduction of edge density fluctuations for $f < 80\,\mathrm{kHz}$ is observed, along with the appearance of the WCM at $f = 120\,\mathrm{kHz}$. The WCM is detectable not only in the edge electron density fluctuations, but also in the edge electron temperature and magnetic field fluctuations [108, 109]. Their fluctuation levels are around $\tilde{n}_e/n_e = 10$–$20\,\%$ [101, 111], $\tilde{T}_e/T_e = 1$–$10\,\%$ [108, 111] and

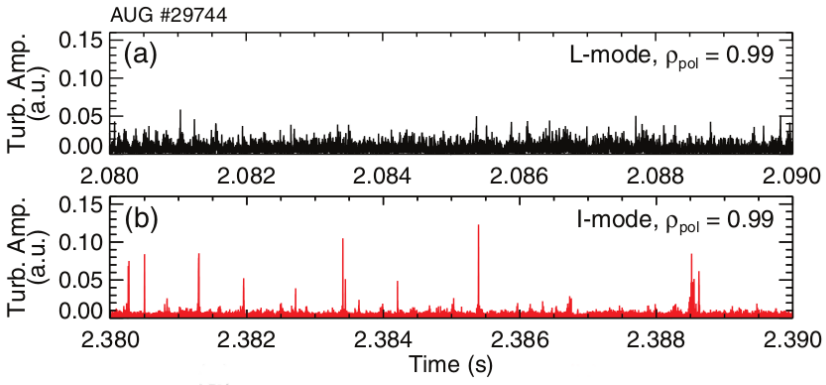

Figure 3.5: Comparison of turbulence amplitude behavior at the plasma edge ($\rho_{\mathrm{pol}} = 0.99$) in (a) L-mode and (b) I-mode. In I-mode, a low turbulence base level and strong bursts are observed, while the L-mode exhibits a higher turbulence level. Figure from [110].

[2]Reflectometry is described in subsection 4.4.4.

$\tilde{B}/B = 0.01$–$0.02\,\%$ [105]. The WCM is localized in the edge of the confined region $0.97 < \rho_{\mathrm{pol}} < 0.99 \pm 0.01$ [105]. The toroidal mode number associated to the WCM is between $15-25$ [109].
During I-mode discharges, also edge turbulence changes w.r.t. that in L-mode plasmas. This is shown in Fig. 3.5, where the fluctuation amplitude measured at $\rho_{\mathrm{pol}} \approx 0.99$ of an L-mode and I-mode plasma is compared. In L-mode, the signal exhibits a roughly constant turbulence level with few spikes. In contrast, in I-mode the edge turbulence amplitude has a lower base level, but it shows strong intermittent bursts [104, 110]. They are significantly stronger than any fluctuations in L-mode, and last for 2–10 µs.
Figure 3.6 (a) shows three time traces of the fluctuation amplitude relative to the time when a burst arrives ($t = 0$) for different I-mode discharges in AUG. Measurements presented here are from the very edge of the plasma, i.e. $\rho_{\mathrm{pol}} \approx 0.99$. In each case, precursor events with growing amplitude can be observed before the last burst occurs. These precursor events appear with a temporal separation Δt that corresponds to a frequency of $f = 1/\Delta t = 90\,\mathrm{kHz}$. Such frequency is very similar to the frequency of the WCM in these discharges ($f_{\mathrm{WCM}} = 100\,\mathrm{kHz}$), as it can be seen from the spectral power of reflectometry signal in Fig. 3.6 (b). This indicates a possible connection between WCM and the bursts observed in I-mode.

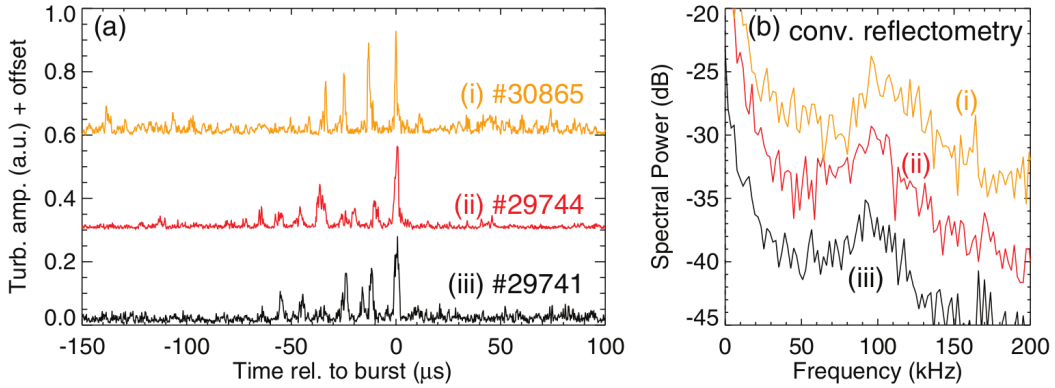

Figure 3.6: (a) Time traces of turbulence amplitude signal measured at $\rho_{\mathrm{pol}} \approx 0.99$ relative to the time when a burst arrives. Three different AUG I-mode discharges are depicted. (b) Spectral power of reflectometry signal in those three different discharges. The frequency of the precursor events occurring before the onset of a strong burst corresponds to the frequency of the WCM. Figure from [104].

3.2.3 I-mode ELM-like events

I-mode plasmas are free of type-I ELMs. This is because the I-mode pedestal is ideal peeling-ballooning stable [104, 112]. Nevertheless, small 'ELM-like' events are reported for I-Mode plasmas in C-Mod [37, 112], though only for a limited subset of discharges. In C-Mod, these ELM-like events are often triggered by a periodic core MHD instability, called sawtooth instability [113, 114].

The heat pulse caused by the core relaxations travels to the edeg, and thus can trigger such 'ELM-like' events or even transitions to H-mode [115–117] or I-mode [118]. However, in C-Mod these ELM-like events can also appear in the absence of the sawtooth instability.

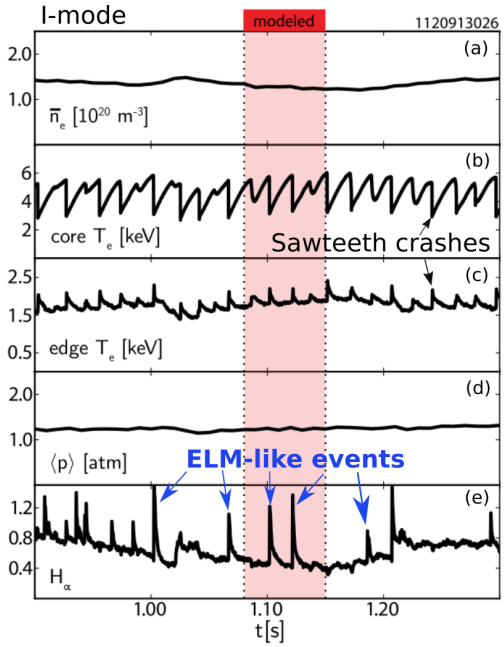

Figure 3.7: Time traces line-averaged electron density (a), core (b) and edge (c) electron temperature, volume-averaged plasma pressure (d) and H_α emission intensity in the divertor region during an I-mode discharge in C-Mod. ELM-like events are visible from the H_α signal. Figure adapted from [112].

An example of an I-mode discharge with such events is shown in Fig. 3.7. Throughout the I-mode, sawteeth oscillations are present. They are visible in panel (b) from the time trace of the core electron temperature, which drops periodically. The H_α emission intensity measured in the divertor region clearly shows the appearance of these ELM-like events, which are transiently expelling a larger amount of plasma into the open magnetic field lines of the SOL. Stability analysis of the I-mode edge profiles with 'ELM-like' events revealed that the plasma edge is ideal peeling-ballooning stable [112]. In C-Mod, the relative plasma energy loss associated to these events was roughly estimated to be $\Delta W/W \simeq 0.5 - 1.5\,\%$ [37].
These events have not been extensively investigated yet. However, understanding the appearance and the amount of energy expelled by these events is fundamental for the I-mode candidature as an operational regime in a fusion power plant. In this thesis the appearance and energy expelled by these events will be investigated in the ASDEX Upgrade tokamak.

3.2.4 Previous studies on I-mode power exhaust

Prior to this thesis work, the only power exhaust studies on the I-mode regime were performed in the Alcator C-Mod tokamak. A recent work carried out in C-Mod [54] analyzed the SOL power decay length λ_q in I-mode plasmas, comparing it to other confinement regimes (L-mode and EDA H-mode). Figure 3.8 shows the main results of this study. Firstly, all three confinement regimes ex-

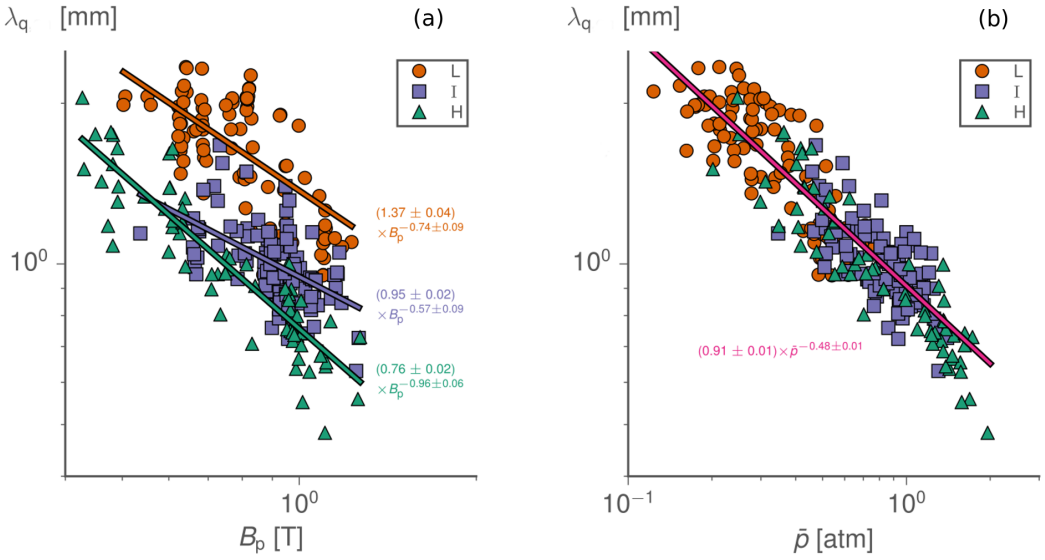

Figure 3.8: (a) Scaling of the SOL power decay length λ_q in L-mode (circles), I-mode (squares) and EDA H-mode (triangles) plasmas with the poloidal magnetic field B_{pol}. (b) Scaling of λ_q across the three confinement regimes with the volume-averaged plasma pressure. Data are from C-Mod. Figure adapted from [54].

hibit a dependence on the poloidal magnetic field B_{p}, however, each one with a different scaling law. H-mode λ_q data scale inversely with the poloidal magnetic field, as already found in [85], see section 2.1.3. L-mode λ_q values are about 2 times as large as in H-mode and with a shallower B_{p} dependence, as also found in [92, 93]. I-mode λ_q data span the space between L-mode and H-mode data for a given value of B_{p}. They exhibit an approximately inverse square root dependence on the poloidal magnetic field for C-Mod data:

$$\lambda_q^{\text{I-mode}}[\mathrm{mm}] \approx 0.95 \times (B_{\mathrm{p}}[\mathrm{T}])^{-0.57}, \tag{3.5}$$

but with a large scatter.
As already introduced in section 2.1.3, λ_q data of these three confinement regimes have been brought together in a single scaling law that groups them across different confinement regimes more coherently. Figure 3.8 (b) shows the resulting scaling law, which predicts λ_q to scale inversely with the square root of the volume-averaged plasma pressure $\bar{p}$. This holds for L-mode, I-mode and H-mode plasmas. However, it remains unclear the physical reason behind such correlation, which cannot be assessed by core-related quantities such as

$\bar{p}$. This can be further studied if correlations between λ_q and local edge plasma parameters are analyzed. During this thesis a cross-regime scaling law of λ_q will be derived and correlated to local edge and SOL plasma parameters.
Regarding I-mode divertor stationary in-out asymmetries, only very few studies are present. Since I-mode plasmas are achieved in reversed-field configuration, based on previous studies carried out in L-mode and H-mode (see section 2.1.6), one would expect a more balanced in-out divertor power sharing. In Ref. [119], it is specified that in I-mode plasmas in C-Mod, the inner target receives roughly 1.5 to 3 times more shot-integrated energy than that received by the outer target. Another C-Mod study [120] showed the influence of the closeness to the double null configuration on the divertor power sharing. The more the plasma shape approaches the double null configuration, the more the divertor power is deposited on the lower and upper outer divertor targets [120]. In this thesis, I-mode divertor power in-out asymmetries are investigated and compared to those of L-mode and H-mode plasmas.
Concerning transient power loads associated to the 'ELM-like' events introduced in section 3.2.3, no studies have been performed so far. However, this is of particular importance as the main benefit of I-Mode to be ELM-free shall not be hampered by the appearance of ELM-like events. Though they are much smaller in amplitude than type-I ELMs, it is yet unclear if they would constitute an issue for reactor-like designs. Therefore, divertor transient power load associated with these events are investigated in this thesis.

In summary, the I-mode is an attractive high-energy confinement regime without type-I ELMs. However, additional studies concerning power exhaust are needed to assess its compatibility with a fusion reactor. In the next chapters, investigations on stationary and transient I-mode power loads are carried out and compared to those of L-mode and H-mode plasmas.

Chapter 4

Experimental Setup

The experiments for this thesis have been carried out at the ASDEX Upgrade (AUG) tokamak. In this chapter the main features of AUG, along with the main diagnostics used for this thesis, are described.

4.1 ASDEX Upgrade

The ASDEX (Axially Symmetric Divertor EXperiment) Upgrade tokamak [10] is operating since 1991 at the Max Planck Institute for Plasma Physics in Garching. The main technical and plasma parameters of ASDEX Upgrade are shown in table 4.1. Having a medium size major radius ($R = 1.65\,\mathrm{m}$) and an external heating power of about 30 MW, AUG is the highest powered experimental fusion device with respect to its dimensions world wide. This allows to study reactor relevant divertor and SOL plasma physics. In addition, AUG has been the first tokamak to demonstrate operation with a full metal (tungsten) wall [121]. Tungsten is considered as the most promising material for plasma

Parameter	Value
Major radius, R [m]	1.65
Minor plasma radius, a [m]	0.5
Magnetic field strength, $B(0)$ [T]	≤ 3.2
Plasma current [MA]	0.4–1.4
Pulse duration [s]	≤ 10
Working gas	D, H, He
Neutral beam injection heating power [MW]	20
Ion cyclotron heating power [MW]	7
Electron cyclotron heating power [MW]	5.5
Plasma volume [m^3]	13
Electron density, $n_e(0)$ [m^{-3}]	$\leq 2 \times 10^{20}$
Electron temperature, $T_e(0)$ [keV]	≤ 10

Table 4.1: Technical and plasma parameters for ASDEX Upgrade. For details on the heating systems refer to [122, 123].

facing components in a future fusion reactor. Experiments in AUG can be

carried out with different working gases: Deuterium, hydrogen or helium. Tritium is not used. In this thesis, discharges with deuterium and hydrogen as working gas are studied. The plasma can be heated in several ways, which will be described in the following paragraphs.

Ohmic heating

As in any tokamak device, the toroidal current heats up the plasma. This is the same process happening when an electric current flows in a wire, i.e. Ohmic heating, and it follows the law $P_{\mathrm{OH}} = R_{\mathrm{p}} I_{\mathrm{p}}^2$, where I_{p} and R_{p} are the plasma current and resistance, respectively. The typical Ohmic heating power at AUG is about 1 MW. However, since $R_{\mathrm{p}} \propto T_e^{-3/2}$ where T_e is the electron temperature, the Ohmic heating reduces when the plasma temperature rises. Therefore, other external heating mechanisms need to be introduced in order to achieve high temperatures. These can be classified in two groups: electromagnetic wave heating and neutral beam injection (NBI) heating.

Electromagnetic wave heating

Electromagnetic wave heating takes advantage of the cyclotron motion of ions and electrons around magnetic field lines, which is described by the cyclotron frequency $\omega_{\mathrm{c}} = eB/m$, where m is the ion or electron mass and e the elementary charge. Electromagnetic waves can propagate in the plasma and deposit energy to either electrons or ions via resonant absorption at their corresponding resonance frequencies. Then, the heated plasma particles will transfer their energy via Coulomb collisions. The Electron Cyclotron Resonance Heating (ECRH) system installed at AUG heats directly electrons, launching waves in the GHz range (140 and 105 GHz) and it has been able to provide up to 5.5 MW to the plasma [10]. The Ion Cyclotron Resonance Heating (ICRH) system at AUG heats ions, launching waves with frequencies of 30–80 MHz and releasing up to 7 MW to the plasma [10].

Neutral beam injection heating

The most powerful system used to heat the plasma is NBI heating. The working principle is simple: a beam of energetic neutral deuterium atoms is injected into the plasma. Neutral atoms are not deflected by the magnetic field and thus they are capable to reach the plasma center. Once the beam enters the plasma, it is ionized via collisions with the background plasma. The resulting high-energetic charged particles transfer their energy to both ions and electrons via Coulomb collisions. AUG is equipped with eight NBI sources [122], each capable of providing up to 2.5 MW of heating power, for a total of 20 MW.

4.2 Divertor tiles and operational restrictions

ASDEX Upgrade is equipped with upper and lower divertor tiles to accommodate the exhaust power in the upper and lower single null (USN and LSN) plasma configurations, respectively. Most of AUG's plasma facing components, including divertor tiles, are made of graphite and are coated with a thin (few tens of μm) tungsten layer. Only the lower outer divertor tiles are made of bulk tungsten. This is due to both an economical and structural engineering reason; indeed, covering the entire vessel with heavy bulk tungsten tiles would require additional supporting structures and would introduce a higher degree of engineering complexity in the machine, besides increasing the costs.
Most of AUG discharges are carried out in LSN configuration. To avoid formation of leading edges in the divertor tiles, the inner and outer lower divertor tiles are toroidally tilted. In this way, each leading edge is shadowed by the neighboring tile and risk of tile melting is reduced (see section 2.1.1). On the contrary, the upper divertor tiles are not toroidally tilted. Therefore, they have leading edges; however, the reduced number of USN discharges per experimental campaign and the usual lower power used in USN discharges make thermomechanical stresses in the tiles tolerable.
Because of their toroidal inclination, the lower divertor tiles are optimized for a specific magnetic field line direction. As most of AUG discharges are carried out in favorable configuration to have easier access to H-mode, the lower divertor tiles are optimized for the B-field direction in favorable configuration. However, if one component of the magnetic field is reversed, for example the toroidal one (see Fig. 2.3) even larger thermomechanical stresses can arise. For this reason, operation in 'reverse-field' (or unfavorable) configuration are possible in LSN plasmas only when *both* the toroidal *and* poloidal magnetic field components are reversed, in order to keep the same magnetic field line helicity. Since the poloidal magnetic field is created by the plasma current in tokamaks, LSN plasmas in unfavorable configuration are obtained in the so-called reversed I_p/B_t plasmas, i.e. discharges with both the plasma current and the toroidal magnetic field reversed w.r.t. the "standard" direction. On the other hand, USN plasmas in unfavorable configuration are achieved without reversing the plasma current direction, as the divertor tiles are not optimized for one magnetic field line inclination. Since reversing the plasma current limits the usage of the NBI heating system due to strong ion orbit losses, plasmas in the unfavorable configuration are more frequently studied in USN at AUG.

4.3 Infrared thermography

The main diagnostics used in this thesis is infrared (IR) thermography. IR thermography is used to measure the surface temperature of solid objects and, in this particular case, of the divertor target plates. From this, the heat flux

reaching the divertor target plates can be evaluated. In the next sections it is described how IR thermography is used to evaluate heat fluxes at AUG.

4.3.1 Planck's law

An object absorbing electromagnetic radiation at all wavelength without any reflection is called black body. Planck's law describes the spectral radiance M ($\mathrm{W{\cdot}sr^{-1}{\cdot}m^{-3}}$) emitted by a black body in thermal equilibrium at a certain temperature T [124]:

$$M(\lambda, T) = \frac{2\pi hc^2}{\lambda^5} \frac{1}{\exp(\frac{hc}{\lambda k_\mathrm{B} T}) - 1}, \tag{4.1}$$

where λ is the wavelength, h is Planck's constant, c the velocity of light and k_B is the Boltzmann constant. The spectral radiance is the power emitted from a surface area $\mathrm{d}A$ in the wavelength interval $\mathrm{d}\lambda$ and in the solid angle $\mathrm{d}\Omega$. For an object in thermal equilibrium the absorbed power is equal to the emitted one. A black body in thermal equilibrium emits all the incident energy, as it absorbs all incident radiation. Conversely, a real object in thermal equilibrium emits less energy than the incident one, since it has finite reflections and, hence, it does not absorb all incident radiation. For this reason the spectral radiance of a real object will be lower than that of a black body.
The ratio between the spectral radiance of a real object and the black body is called emissivity, $\epsilon = \epsilon(\lambda, T)$. The emissivity depends on the wavelength and surface temperature and it ranges between 0 and 1, with $\epsilon = 1$ for a black body. Since IR cameras measure the number of photons reaching the detector, it is convenient to rewrite Eq. 4.1 as a photon flux Γ by dividing the emitted power by the energy of each photon $E_\gamma = hc/\lambda$:

$$\Gamma(\lambda, T) = \epsilon(\lambda, T) \frac{2\pi c}{\lambda^4} \frac{1}{\exp(\frac{hc}{\lambda k_\mathrm{B} T}) - 1}. \tag{4.2}$$

Note that Γ denotes the number of photons emitted per second by any object (as the emissivity has been introduced), per unit surface, solid angle and wavelength ($s^{-1}{\cdot}\mathrm{sr^{-1}{\cdot}m^{-3}}$). Figure 4.1 shows the emitted black body photon flux against the surface temperature for different wavelengths, which are in the visible/near infrared (vis/NIR, $\lambda = 0.9$–$1.1\,\mu\mathrm{m}$), in the mid wavelength infrared (MWIR, $\lambda = 4$–$5\,\mu\mathrm{m}$) and in the long wavelength infrared (LWIR, $\lambda = 9$–$11\,\mu\mathrm{m}$) range, respectively. The photon flux exhibits a different behaviour depending on the wavelength. In the vis/NIR, the photon flux raises substantially for $T > 1000\,\mathrm{K}$. Therefore this wavelength range is not suitable for divertor measurements, where the temperature can also be around 500 K. Nonetheless, cameras in the vis/NIR are used at AUG for machine protection where only components with high temperatures need to be detected [125]. Conversely, in the MWIR the photon flux assumes relatively large values across

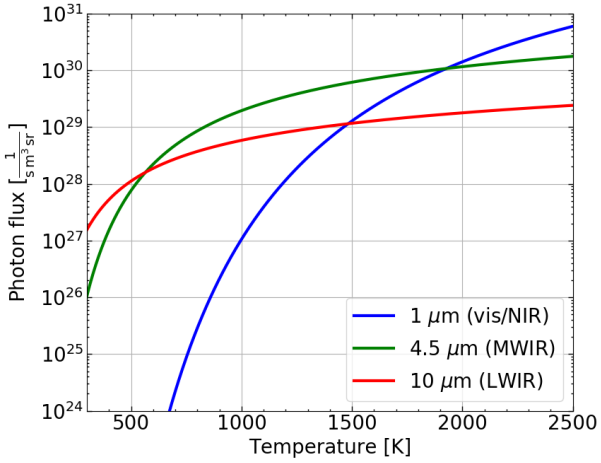

Figure 4.1: Photon flux (Eq. 4.2) emitted by a black body for different wavelengths against the surface temperature. For the surface temperatures of AUG divertor, the mid wavelength infrared (MWIR) range is the most suited.

the entire temperature range. In the LWIR, the photon flux is larger at room temperature, but is lower than the MWIR one for $T > 600\,\mathrm{K}$. Since the divertor temperature mainly ranges between 500 K and 1500 K, the MWIR suits best for the measurements. For this reason, IR cameras at AUG are equipped with a filter around $\lambda = 4.5\,\mu\mathrm{m}$.

4.3.2 From camera data to temperature

IR camera detectors measure directly the number of counts reaching the sensor during a certain integration time. From this measurement several corrections need to be introduced to obtain the surface temperature. Hereinafter, they are briefly discussed.

Gain and offset correction

The IR camera detector uses an InSb Complementary Metal Oxide Semiconductor (CMOS) sensor that has a read out logic for each single pixel (and not one read out logic for all the pixels). This results in a nonuniform image. To obtain a uniform image the so-called gain and offset have to be taken into account. To estimate these parameters the camera view is covered by a uniform black body (e.g. lens cover) in such a way that each pixel receives the same photon flux. The counts measured by the detector are proportional to the integration time (i.e. the time used to collect photons). By varying the integration time τ and measuring the corresponding digits count N_{digits}, a characteristic straight line can be found for each pixel $N^{\mathrm{pix}}_{\mathrm{digits}} = b_{\mathrm{pix}} + a_{\mathrm{pix}} \cdot \tau \cdot \Gamma$. The slope of the straight line is the gain a_{pix}, while the offset of that pixel is b_{pix}. The gain and offset vary for each pixel. To obtain a uniform image, first the offset b_{pix}

is subtracted from the digit counts of each pixel; then the gain of each pixel is normalized to the median gain of all the pixels, a_{median}, in order to have a uniform image while retaining the total response of the system. To obtain the count rate (counts per µs), the corrected digital level has to be divided by the integration time, yielding:

$$\Gamma = \frac{N_{\text{digits}}^{\text{pix}} - b_{\text{pix}}}{a_{\text{median}}\tau}. \tag{4.3}$$

Equation 4.3 is used to obtain the corrected count rate of each pixel.

Bad pixel correction

After the gain and offset correction, the image can still be composed of pixels that deviate from the expected response. Those "bad" pixels could be stuck at low or high values. They can be easily recognized by analyzing the gain and offset correction, as they have no gain. In addition, also pixels with a deviating response with respect to the median one can be detected. Once a bad pixel is recognized, its value is replaced with the mean from its four nearest neighbors.

Movement correction

At ASDEX Upgrade periodic forces act on the camera, in particular during an ELM event, inducing oscillating displacements of the camera. Moreover, the infrared camera observes the upper divertor over two mirrors and with an optical distance of around 4 m. Therefore, every movement of the mirror and of the camera is amplified and needs to be taken into account for a correct evaluation of heat fluxes. The movement correction is calculated by computing the phase correlation between two frames. The position of the maximum of the phase correlation gives the shift between two frames. For more details refer to [81].

Temperature calibration

Once all these corrections are evaluated, the corrected count rate (which is strictly related to the photon flux) can be converted to temperature by means of Planck's law. Eq. 4.2 is simplified by considering that filters reduce the observed wavelength interval and by assuming a homogeneous surface:

$$\Gamma(\lambda, T) = c_0 \epsilon \frac{2\pi c}{\lambda_{\text{eff}}^4} \frac{1}{\exp(\frac{hc}{\lambda_{\text{eff}} k_{\text{B}} T}) - 1} \tag{4.4}$$

where now λ_{eff} denotes the effective wavelength of the filter used for the measurement and the constant c_0 contains information about the solid angle and the spectral bandwidth of the measurement. This constant has to be obtained via calibration. The camera is calibrated using a cavity radiator with a known emissivity of $\epsilon = 0.95$ and a known temperature (ranging between 100 °C and

1200 °C). In this way a relationship between the count rate measured by the camera (coming from an object of $\epsilon = 0.95$), $\Gamma_{\epsilon=0.95}$, and surface temperature of this object can be found. Finally, the photon flux measured by the camera from an object with emissivity ϵ will be given by:

$$\Gamma = \frac{\epsilon}{0.95}\Gamma_{\epsilon=0.95} = \frac{\epsilon}{0.95}\frac{c_1}{\exp(\frac{c_2}{T}) - 1} \tag{4.5}$$

where c_1 and c_2 are calibration constants for the effective wavelength λ_{eff}. Eq. 4.5 can be inverted to find the surface temperature of the observed object.

4.3.3 Heat flux calculation

Once the surface temperature $T(s,t)$ is known, where s is the coordinate along the divertor tile surface, the heat flux $q(s,t)$ can be calculated. This is done by using the THEODOR (THermal Energy Onto DivertOR) code [81, 126, 127], which solves the 2D heat diffusion equation in the poloidal cross-section of the divertor target tile:

$$\rho c_p \frac{\partial T}{\partial t} = \nabla \cdot (\kappa \nabla T), \tag{4.6}$$

where ρ is the mass density, c_p the specific heat capacity and κ the heat conductivity of the target material. The outer lower divertor tiles are bulk tungsten, therefore tungsten material properties are used. Conversely, the upper divertor and the lower inner divertor targets are graphite tiles covered by a tungsten coating of few µm, hence carbon material properties are used. In order to solve the non-linear heat diffusion equation, the following substitution is introduced, using the heat potential u:

$$u(T) = \int_0^T \kappa(T')\mathrm{d}T', \tag{4.7}$$

which leads to the following linear diffusion equation:

$$\frac{\partial u}{\partial t} = \frac{\kappa}{\rho c_p}\Delta u = D\Delta u. \tag{4.8}$$

Equation 4.8 is solved using an implicit scheme [128]. The measured surface temperature $T(s,t)$ is used as a boundary condition. The discretization step perpendicular to the surface Δx is chosen in order to have the Courant number $\frac{D\Delta t}{(\Delta x)^2}$ equal to one. Lastly the perpendicular heat flux onto the divertor tile is calculated from the heat potential at the surface via Fourier's law:

$$q = -\nabla u|_{\text{surf}}. \tag{4.9}$$

4.3.4 IR camera system at ASDEX Upgrade

ASDEX Upgrade is equipped with a system of IR cameras observing the lower and upper divertor targets. Both cameras are installed on the low field side

(LFS). A poloidal cross-section of a plasma with a low magnetic X-point and the IR view on the lower outer divertor target are shown in Fig. 4.2. This camera view is over a mirror installed in the vessel. The IR camera provides a 2D image of the divertor target (Fig. 4.2(b)). From this image, a 1D line

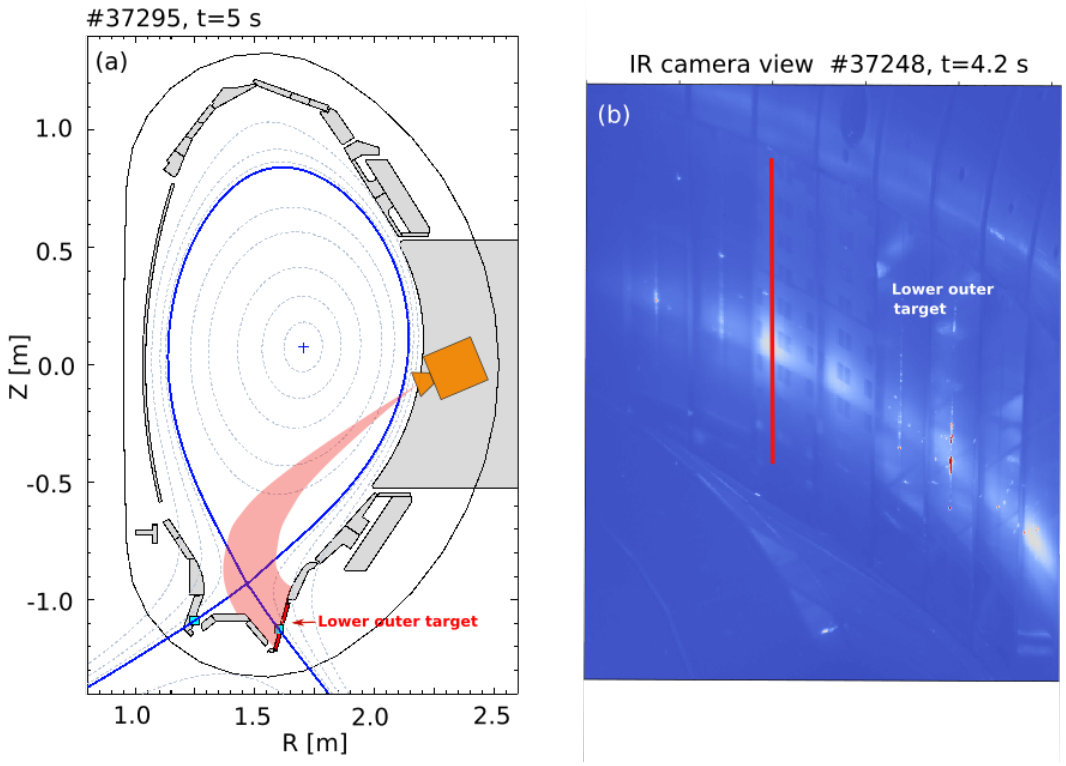

Figure 4.2: Poloidal cross section of a LSN plasma equilibrium at ASDEX Upgrade (a) and photon counts measured by the IR camera looking at the lower outer divertor target (b). The cyan squares in panel (a) are the strike points, while the light red area is the IR camera line of sight projected onto the poloidal plane. The red line in panel (b) indicates where the 1D profile for the heat flux calculation is taken.

(marked in red in Fig 4.2(b)) is chosen to obtain the 1D temperature profile as input for the THEODOR code. The castellated structure on the divertor tile is used to improve the movement correction.
Table 4.2 summarizes the technical parameters of the IR camera looking at the outer lower divertor for the different confinement regimes analyzed. The Analog-to-Digital Converter (ADC) resolution is 15 bit for low-heated discharges (L-mode and I-mode) where the signal-to-noise ratio is lower, whereas

Parameter	L-mode	I-mode	H-mode
Frame rate [Hz]	600	2100	2100
Spectral range [µm]		4.7 ± 0.15	
Spacial resolution [mm/pixel]		0.6	
ADC resolution [bit]	15	15	14

Table 4.2: Parameters of the IR camera viewing the lower outer divertor.

it is 14 bit for high-power discharges (H-mode). The frame rate (or acquisition frequency) of the camera depends mainly on how many camera pixels have to be read out. Therefore, a large view on the divertor implies a low acquisition frequency, while a smaller view allows to reach higher acquisition frequencies. In L-mode plasmas, since no fast transients occur, it is preferred to have a larger view on the divertor to improve the movement correction. In I-mode and H-mode plasmas, where fast transients can occur, a smaller view is chosen to obtain higher acquisition frequencies.

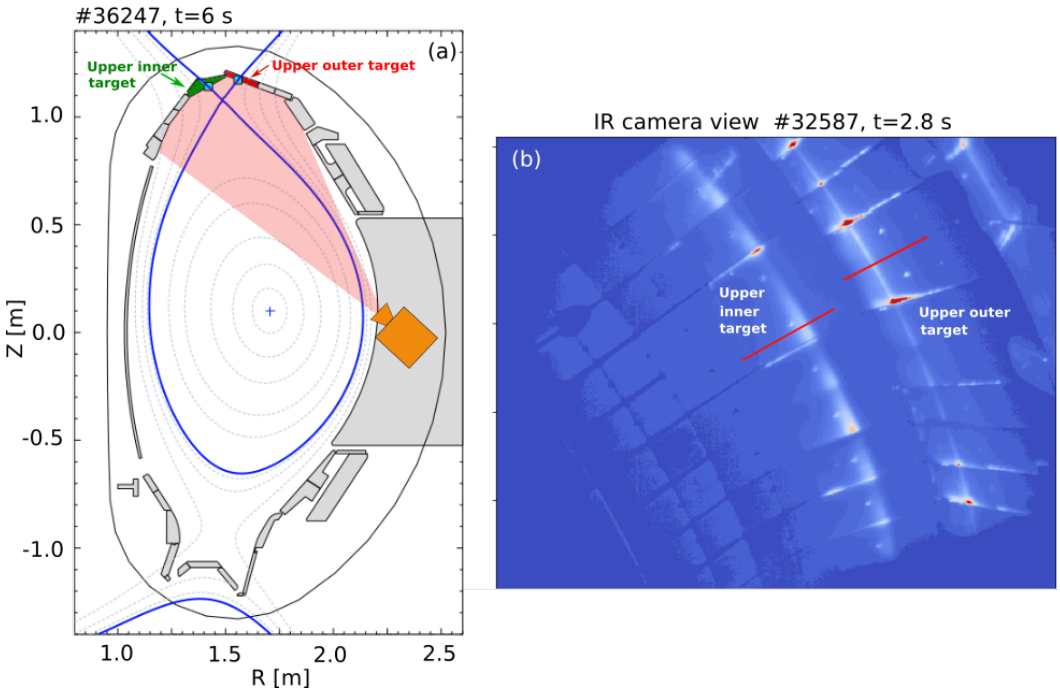

Figure 4.3: Poloidal cross section of an USN plasma equilibrium at ASDEX Upgrade (a) and photon counts measured by the IR camera looking at the upper divertor targets (b). The cyan squares in panel (a) are the upper strike points. The IR camera simultaneously looks at the inner and outer upper divertor targets. The red lines in panel (b) indicate where the 1D profiles for the heat flux calculation are taken.

Figure 4.3 shows a poloidal cross section of an USN plasma equilibrium and the IR view on the inner and outer upper divertor targets. The IR camera is equipped with steerable mirrors that can change the viewing angle inside the torus. Therefore, this camera can observe not only the upper divertor but also the ICRH antenna limiters, the lower inner divertor target and the inner heat shield (i.e. the part of the vessel on the high field side). Throughout this thesis, this IR camera will be used for upper divertor studies. The IR view provides images of both inner and outer divertor targets simultaneously. Hence, two 1D profiles (one for the outer and one for the inner target) are extracted to calculate heat fluxes, as shown in Fig. 4.3(b). Table 4.3 describes the main technical parameters of this camera. Due to the more inclined view of the upper outer target, the spatial resolution is lower for the outer than for

the inner target. The frame rate of this camera can vary largely depending on which frame window is chosen.

Parameter	L-mode	I-mode	H-mode
Frame rate [Hz]		400 – 1500	
Spectral range [µm]		4.7 ± 0.15	
Spacial resolution outer [mm/pixel]		2.2	
Spacial resolution inner [mm/pixel]		1.5	
ADC resolution [bit]	15	15	14

Table 4.3: Parameters of the IR camera viewing the upper divertor.

4.4 Supplementary diagnostics

In this section diagnostics to measure electron temperature and density profiles and/or fluctuations in different region of the plasma are described. Also, diagnostics to measure the plasma radiation and magnetic fluctuations are introduced. The physical measurement principle along with temporal and spatial resolution of each diagnostics is briefly discussed.

4.4.1 Thomson scattering

Thomson Scattering (TS) is a widely used process exploited to obtain localized and simultaneous measurements of the electron temperature and density in plasmas. It is based on the elastic scattering of photons from a laser beam by plasma electrons [129]. The process of electromagnetic wave scattering by charged particles may be thought of as follows. The electric and magnetic fields of the incident wave accelerate charged particles (mainly the electrons, as $m_e \ll m_i$). Accelerated electrons, in turn, create electromagnetic radiation in all directions, thus scattering the incident wave. The intensity of the elastically scattered light depends on the local electron density, while its Doppler shift is related to the electron velocity distribution function. Assuming a Maxwellian distribution function, it is possible to obtain the electron temperature from the Doppler shift.
ASDEX Upgrade is equipped with a vertical Thomson scattering system that provides electron density and temperature profiles from the plasma core to the edge [130]. Two TS systems of four and six lasers are used for edge and core measurements, respectively. Each laser runs at a frequency of 20 Hz, with an adjustable delay time between them. Usually, they are equally spaced in time and therefore a 80 Hz pulse sequence for the core and a 120 Hz for the edge is obtained. Figure 4.4 shows the position of the scattering volumes for both the core and egde TS systems with respect to the plasma equilibrum of a LSN and an USN plasma discharge. The scattering volumes of the core (edge) system have a length of about 25 mm (3 mm). The edge region of the plasma where

steep gradients are located is about 2 cm wide and, hence, it can be spatially resolved by the edge TS system.

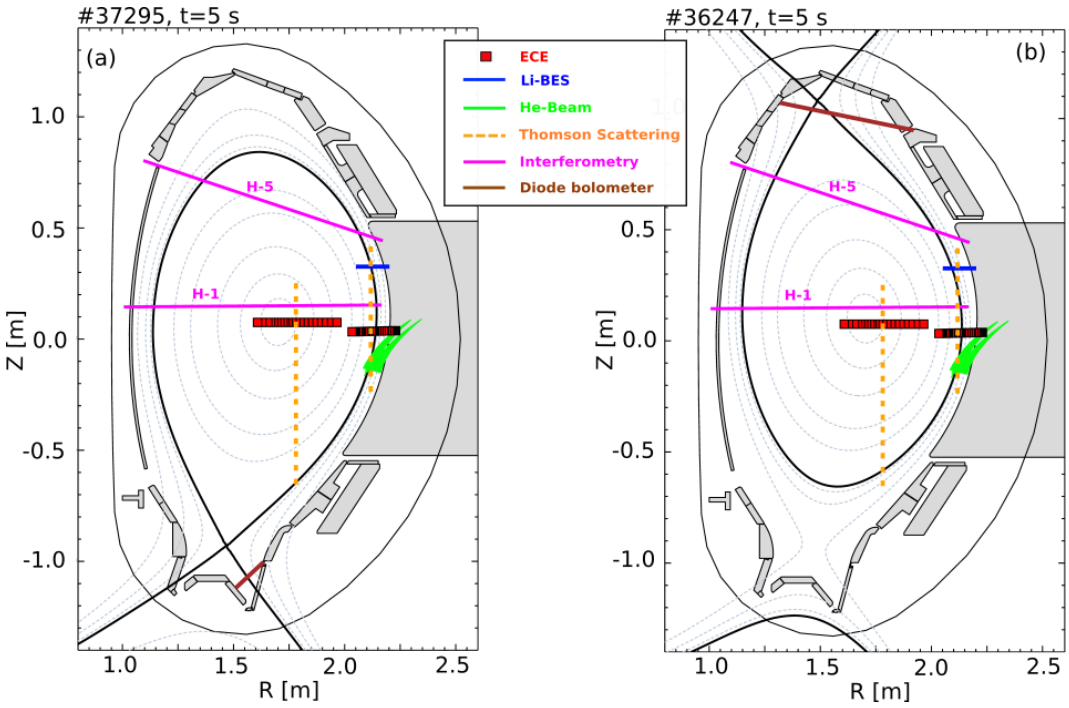

Figure 4.4: Poloidal cross sections of a LSN (a) and an USN (b) plasma equilibrium of ASDEX Upgrade with the measurement positions of several diagnostics.

4.4.2 Electron cyclotron emission

The electron cyclotron emission (ECE) is a broadly used diagnostics to obtain localized and high-frequency measurements of the electron temperature. It takes advantage of the cyclotron motion of electrons around the magnetic field lines, which is characterized by the cyclotron angular frequency $\omega_{\mathrm{c,e}} = eB/m_e$ and its harmonics $\omega_k = k\omega_{\mathrm{c,e}}$ with $k = 1, 2, 3$. Due to their accelerated cyclotron motion, electrons emit electromagnetic radiation at these frequencies. Fusion plasmas are for some particular harmonics of $\omega_{\mathrm{c,e}}$ *optically thick*, which means that they can be considered to represent a black body radiator. This approximation holds because all radiation travelling through the plasma at these frequencies over a sufficient ray path length is absorbed by the plasma. In fusion plasmas, since $h\nu \ll kT$, the Rayleigh-Jeans approximation of Planck's law (Eq. 4.1) can be used, giving:

$$M(T) = \frac{\omega^2}{2\pi^2 c^2} k_{\mathrm{B}} T_e. \tag{4.10}$$

With this simple formula the electron temperature is obtained from the measured spectral radiance M at a certain frequency. Moreover, in tokamak devices

the magnetic field strength is spatially inhomogeneous (i.e. $B \propto 1/R$, where R is the majour radius). Therefore, as $\omega = \omega(B(r))$, spectral resolution of ECE measurements translates to spatial resolution. Since the optically thick layer in the plasma is relatively small (few mm), ECE measurements at different frequencies can be spatially resolved with high-accuracy. In this way, T_e radial profiles are obtained.
However, the plasma is not always optically thick. In particular, at low densities the plasma can be *optically thin*, meaning that a fraction of the radiation is not absorbed and passes through (or shines through) the plasma. When this happens, the shined-through radiation will undertake multiple reflections in the vessel, increasing the measured radiative temperature at the resonance layer (see e.g. [131]). This phenomenon is often referred to as "shine-through effect". For this reason, in the region when the plasma is optically thin, ECE measurements become less reliable and additional effects related to radiation transport must be taken into account for a correct evaluation of T_e.
At ASDEX Upgrade the ECE system measures radiation at the second harmonic of the cyclotron frequency in extraordinary polarization (i.e. electric field vector perpendicular to the magnetic field) with a sampling rate of 1 MHz. The system measures sixty different frequencies simultaneously, to obtain the desired spatial resolution. The measurement positions of the ECE temperature, for a standard plasma discharge with $B_0 = 2.5\,\mathrm{T}$, are depicted in Fig. 4.4.

4.4.3 Interferometry

Interferometry is used in plasmas to measure the line-averaged electron density. It exploits the difference between the refractive index of the plasma N_p, which depends on the electron density, and the one of vacuum $N_\mathrm{v} = 1$. The refractive index for an electromagnetic wave propagating in a magnetized plasma in ordinary mode (O-mode) polarization (i.e. electric field parallel to the magnetic field) is:

$$N_\mathrm{p} = \sqrt{1 - \left(\frac{\omega_p}{\omega_0}\right)^2} = \sqrt{1 - \frac{e^2 n_e}{\epsilon_0 m_e \omega_0^2}}, \tag{4.11}$$

where ω_0 is the angular frequency of the wave, ω_p is the plasma frequency, e is the elementary charge, ϵ_0 is the dielectric constant and m_e the electron mass. By superimposing two different waves, one traveling through the plasma and another propagating in vacuum, a phase difference is introduced:

$$\Delta\phi = \frac{2\pi}{\lambda} \int (N_\mathrm{v} - N_\mathrm{p}) \mathrm{d}l \approx \frac{\lambda e^2}{4\pi\epsilon_0 m_e c^2} \int n_e(l) \mathrm{d}l, \tag{4.12}$$

where N_p has been Taylor expanded at the first order assuming $\omega_p/\omega_0 \ll 1$. With Eq. 4.12 the line-averaged density can be calculated from the measured phase shift.
At ASDEX Upgrade, a deuterium cyanide (DCN) laser with a wavelength of

195 µm is used for the measurement [132]. The system has a phase resolution of $2\pi/64$, which corresponds to a line-integrated density resolution of about $8.9 \times 10^{16}\,\mathrm{m}^{-2}$. It provides measurements with a frequency of 10 kHz. The beam is split into five different components (H-1 to H-5) that propagate in the plasma across different paths. The first beam (H-1) crosses the plasma core and provides a core line-averaged electron density. The fifth beam (H-5) crosses the plasma edge in the pedestal region and gives an edge line-averaged electron density. Their optical paths are shown in Fig 4.4.

4.4.4 Reflectometry

The reflectometry diagnostics is used to measure radial profiles or local fluctuations of the electron density. Its working principle is based on the reflection of a wave from plasma layers where the refractive index goes to zero (cutoff layers). For an O-mode polarized wave, the wave reflection occurs when $\omega = \omega_p$, see Eq. 4.11. Since the plasma frequency depends on the electron density, it is therefore possible to extract information on n_e at the cutoff layer from the reflected wave. In addition, measuring the phase delay of the reflected wave gives information on the cutoff layer position. Therefore, by launching waves in the GHz range (the plasma frequency range in tokamaks), it is possible to reconstruct the electron density as a function of the radial coordinate [129]. To obtain a radial profile, the frequency of the launched wave needs to be swept. Conversely, if local measurements of the density fluctuations are of interest, a wave with fixed frequency is injected.
At ASDEX Upgrade, two reflectometer systems are installed: the frequency modulated continuous wave (FM-CW) broadband reflectometer [133] and the hopping frequency reflectometer [134].
The FM-CW reflectometer has four O-mode channels measuring on the high-field side (HFS) and five O-mode channels measuring on the low-field side (LFS). Both HFS and LFS channels can inject waves in the K, Ka, Q and V-band, measuring densities in the range $0.3 - 6.7 \times 10^{19}\,\mathrm{m}^{-3}$ [135]. The FM-CW reflectometer system can operate in two different modes: the broadband frequency swept mode for profile measurements or the fixed-frequency mode for fluctuation measurements.
The hopping frequency reflectometer system consists of two O-mode channels launching Q-band and V-band waves on the LFS. This system is optimized for density fluctuation measurements, since it is equipped with in phase and quadrature sensitive heterodyne detection that can provide a quantitative analysis of plasma fluctuations with an acquisition frequency of 2 MHz [134]. It operates in a fixed frequency mode that can be tuned during the discharge to probe different cutoff layers in the plasma. In this work, reflectometer diagnostics will be used to measure electron density fluctuations in the plasma edge.

4.4.5 Lithium beam emission spectroscopy

The lithium beam emission spectroscopy (Li-BES) is a technique used in many tokamaks to measure edge electron density profiles with high-spatial and temporal resolution. This diagnostics exploits the interaction between the plasma and neutral lithium atoms. At ASDEX Upgrade a 45 keV neutral lithium beam is injected into the plasma. After collisions with the plasma electrons, the lithium atoms are excited to higher atomic states or ionized. The most populated excited state is Li(2p), which, after a short lifetime, decays to the Li(2s) state, emitting the Li I (2p→2s) line radiation at 670.8 nm. This radiation is detected along the beam path by an optical system. From the spatial distribution of the line intensity, the electron density profile can be obtained using a probabilistic data analysis method [136], which is based on a collisional-radiative model that includes electron-impact excitation, ionization and charge exchange processes [137]. Once the Li beam is ionized, it cannot penetrate further into the plasma as the ions will gyrate around the magnetic field lines. At AUG, the 45 keV Li beam provides high-enough signal until $\rho_{\mathrm{pol}} = 0.95$. For this reason the diagnostics is mainly used to determine the edge electron density profile.
Figure 4.4 shows the measurement position projected on the poloidal plane. The present Li beam system installed [138] provides electron density profiles with a time resolution of 200 kHz and with a spatial resolution of 6 mm. During each discharge the Li beam undertakes a 70 % duty-cycle, i.e. it is switched on and off for 56 ms and 24 ms, respectively. This is done to calculate the background contribution of the 670.8 nm line that does not originate from the interaction between the Li beam and the plasma. This background contribution is then subtracted from the measured signal to obtain the active contribution.

4.4.6 Thermal helium beam emission spectroscopy

In a similar way, injection of helium into a hot plasmas is a technique to measure simultaneously electron temperature and density with high spatial and temporal resolution. This diagnostics is based on the interaction of neutral helium with the plasma (mainly the electrons). Helium atoms are excited by electron collision to higher atomic singlet and triplet states. Each of these excited states, after a short lifetime, decays to a lower one, emitting radiation in the visible range.
Since the population density of these excited states depends differently on the background T_e and n_e, a combination of their light emission can be used to determine electron density and temperature [139]. At AUG, the ratio of the 667.8 and 728.1 nm line emissions, which are emitted in two de-excitation processes involving singlets (1s3d→1s2p and 1s3s→1s2p, respectively), is used for the electron density evaluation. On the other hand, the ratio of the 706.5 and 728.1 nm line intensities, which are from de-excitations involving triplets

(1s3s→1s2p) and another involving singlets (1s3s→1s2p), is used for the electron temperature evaluation. The thermal helium beam system installed at AUG is able to provide edge electron density and temperature profiles with a spatial resolution of 3 mm and a temporal resolution of 900 kHz [140]. In particular the high-temporal resolution makes this diagnostics suitable to study turbulent fluctuations at the plasma edge. The low-energy helium beam can penetrate into the plasma up to $\rho_{\mathrm{pol}} = 0.98$, being thus mainly a SOL diagnostics. The 32 lines of sight of the diagnostics are depicted in Fig 4.4 for both a LSN and an USN configurations at AUG.

4.4.7 Integrated data analysis of electron density and temperature profiles

Integrated data analysis (IDA) [141] is used to reconstruct the electron density and temperature profiles combining different diagnostics measurements. Depending on the required time resolution it uses different combinations of data. When a fast time resolution is required, laser interferometry and Li-BES data are used to reconstruct the electron density, while the ECE is used for the electron temperature. On the other hand, when a few ms time resolution is enough, the Thomson scattering is added to the above-mentioned diagnostics, giving additional input data for both electron temperature and density. The IDA approach uses Bayesian probability theory to reconstruct the profiles. This approach has the advantage of calculating consistent error bars, reducing uncertainties by combining multiple information from different diagnostics and of easily identifying outliers and/or systematic errors. The reconstructed profiles are parameterized with the exponential of a cubic B-spline [141].
Figure 4.5 shows examples of reconstructed IDA electron temperature and

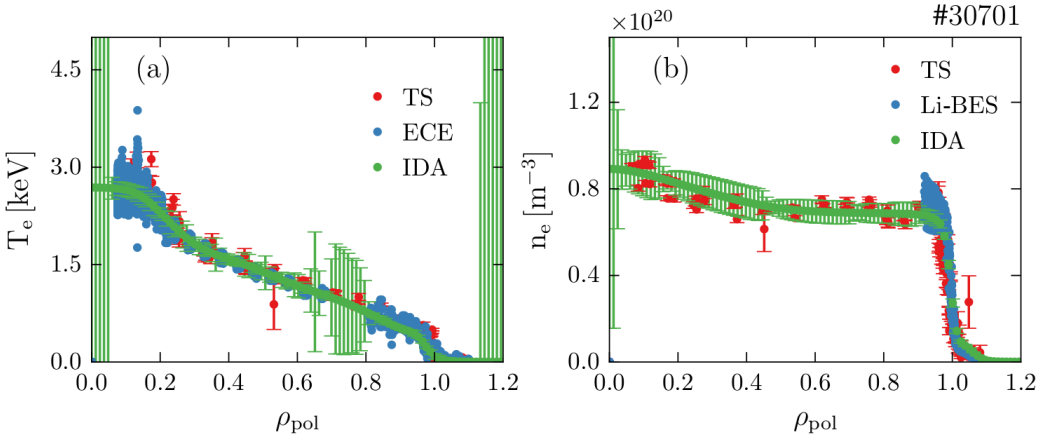

Figure 4.5: Reconstructed IDA electron temperature (a) and density (b) radial profiles (green). (a) T_e from Thomson scattering (red) and ECE (blue). (b) n_e from Thomson scattering (red) and Li-BES (blue). Interferometer data are not shown as they are line-integrated measurements. Figure adapted from [142].

density profiles at AUG. Profiles are plotted against the normalized radius ρ_{pol} (Eq. 1.4). The IDA T_e profile is compared to electron temperature measurements from TS and ECE diagnostics, while the IDA n_e profile is compared to electron density data from TS and Li-BES diagnostics. As interferometer data are line integrated measurements, they are not plotted here.

4.4.8 Bolometers

Bolometers are devices used to measure the electromagnetic radiation emitted by the plasma, which is usually in the vacuum ultraviolet (VUV) region. Bolometers measure the total radiated power along a specific line of sight (LOS) and, since they are sensitive to a wide range of wavelengths, they do not retain any spectral information. There are two main kinds of bolometers installed at ASDEX Upgrade: Foil bolometers and diode bolometers.
Foil bolometers use thin (4.5 µm-thick) foils of chemically inert material (gold or platinum) with a resistor on the backside. The incoming radiation heats up the foil, increasing its temperature. By measuring the resistance change, the foil temperature increase and the deposited power can be calculated. At AUG, the foil bolometer system consists of 112 LOSs from 6 pinhole cameras [143]. Foil bolometers have a time resolution of 2 ms and they are absolutely calibrated [144]. For the latter reason they are used for tomographic inversion and calculation of the radiated power.
Diode bolometers work with Absolute eXtended UltraViolet (AXUV) diodes. The incident radiation creates electron-hole pairs in the semiconductor and, thus, the resulting photocurrent is proportional to the incident radiation energy. They are characterized by a high time resolution, i.e. 5 µs at AUG [143], however their responsitivity is wavelength dependent and deprecates over time. Therefore they cannot be absolutely calibrated. The diode bolometer system at AUG is composed of 256 LOSs from 8 pinhole cameras.
In this work, diode bolometers will be used to monitor fast transient events. The LOSs of the used bolometers are in the divertor region (upper or lower depending on the plasma configuration) and are shown in Fig 4.4.

4.4.9 Magnetic coils

Magnetic induction coils are used to measure equilibrium quantities, such as the total plasma current or plasma position, or magnetic fluctuations. The latter application is of particular interest for this thesis. These coils are called pickup coils and their poloidal and toroidal positions in AUG are shown in Fig 4.6. They are installed inside the vacuum vessel to avoid the shielding effect of the conductive vessel wall [145]. The pickup coils "B31-xx" (red in Fig. 4.6) are oriented to measure only the radial component of the magnetic field fluctuation, $\dot{B}_r$. Conversely, the "Cxx-xx" coils (green in Fig. 4.6) are oriented to measure only the poloidal component of the magnetic field fluctu-

ation, $\dot{B}_\theta$. These coils are often called Mirnov coils, in honor of the Russian scientist who first reported on their use [146]. The data are collected by analog-to-digital converters that measure 512 kHz low-pass filtered voltages from the coils with a sample rate of 2 MHz [147].

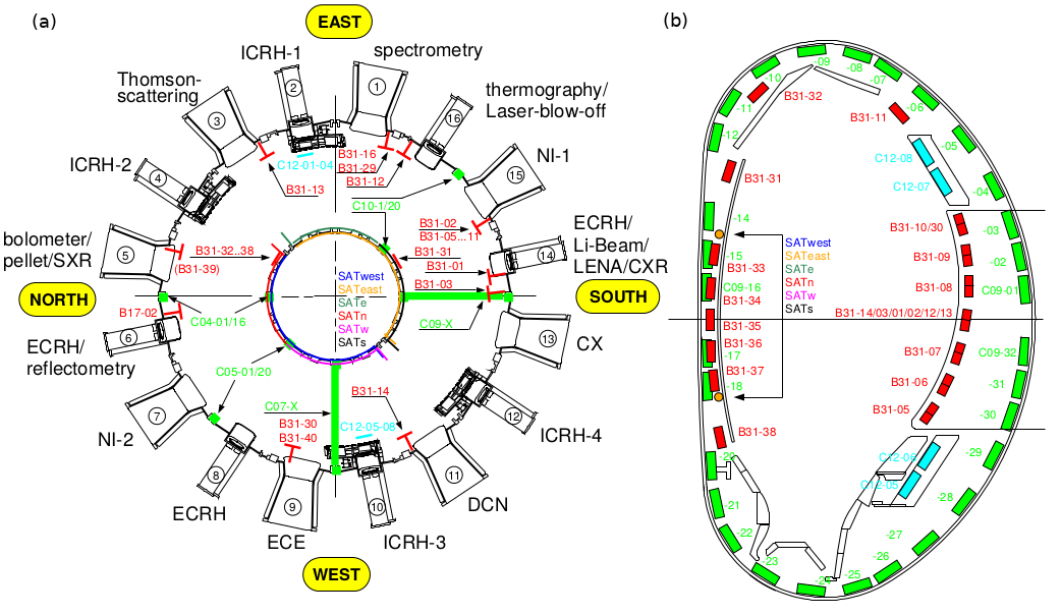

Figure 4.6: Bird's eye view (a) and poloidal overview (b) of the magnetic pickup coils installed at ASDEX Upgrade. Red and green coils measure the radial and poloidal component of the magnetic fluctuation, $\dot{B}_r$ and $\dot{B}_\theta$, respectively.

Chapter 5

Steady-state heat fluxes and SOL decay lengths in L, I and H-mode plasmas

In this chapter, steady-state heat fluxes in different confinement regimes (L-mode, I-mode, inter type-I-ELM H-mode and EDA H-mode) are analyzed[1]. As already mentioned previously, the scrape-off layer (SOL) power decay length λ_q is a crucial quantity to assess the heat flux distribution in the SOL and on the divertor targets. Therefore, it is important to be able to predict this quantity for the design of future devices. In this chapter a cross-regime scaling law of λ_q will be derived based on ASDEX Upgrade data and compared to results from the Alcator C-Mod tokamak [54]. Based on this scaling law, predictions of λ_q in I-mode and H-mode plasmas are carried out for future devices such as ITER.
In addition to that, also SOL electron temperature, density and pressure decay lengths across confinement regimes are analyzed, together with pedestal gradient lengths. These plasma parameters will be for the first time correlated with λ_q in a broad database, shedding light on the physical origin behind the scaling law found in this thesis. Moreover, this analysis will reveal a correlation between electron pressure gradient lengths in the confined region and in the SOL. Gradient lengths in the SOL are relevant for power exhaust, since they set λ_q. On the other hand, edge gradient lengths in the confined region are fundamental for the achievement of high core plasma pressure, since high-confinement modes rely on the pedestal formation at the plasma edge. Therefore, the correlation between these two regions of the plasma tightly bounds the power exhaust problem to the achievement of high energy confinement.
As also discussed in the previous chapters, the power exhaust problem will become more challenging if the heat flux is distributed asymmetrically between the inner and outer divertor targets. For this reason, heat flux inn-out asymmetries are also investigated in different confinement regimes for both

[1]Part of the content of this chapter is published in Ref. [148]

favorable and unfavorable configurations.
To carry out such investigations, a database has been assembled and a consistent analysis technique has been applied to experimental data from all confinement regimes. Before presenting the results, the database and the analysis technique are described in the following sections.

5.1 Database

The database gathered for this study is composed of L-mode, I-mode, and H-mode discharges. I-mode discharges are all in USN configuration, because of the easier operation in reversed-field configuration in USN (see section 4.2). L-mode and H-mode discharges are in both LSN and USN configurations. This allowed us to study L-mode and H-mode plasmas with different ion ∇B drift directions (pointing to and away from the active X-point) and with different divertor geometries (closed lower divertor vs. open upper divertor). The L-mode discharges in LSN described in [93] are reexamined here. H-mode data were taken between type-I-ELMs in LSN and USN, and in EDA H-mode plasmas [33] recently achieved at AUG in LSN.
The database consists of 34 discharges, among which 12 are in LSN, while 22 are in USN. 16 discharges exhibit both L-mode and I-mode phases. To guarantee high-quality IR measurements, discharges with impurity seeding and divertor detachment have not been considered. Only deuterium discharges are included in this study.

	L-mode	I-mode	Type-I-ELM H-mode	EDA H-mode
Configuration	USN/LSN	USN	USN/LSN	LSN
Discharges	20	22	5	2
τ_{E} (ms)	32–192	38–140	53–213	180–210
W_{MHD} (kJ)	68–310	204–394	259–611	270–300
β_{pol}	0.2–1.1	0.4–1.2	0.6–1.0	0.7
$H_{98\mathrm{y},2}$	0.5–0.9	0.7–0.9	0.8–1.3	0.9–1.0
P_{heat} (MW)	0.5–4.2	2.1–4.2	1.4–6.6	1.4–1.7
P_{sep} (MW)	0.2–2.6	1.7–2.8	0.5–3.7	0.5–0.8
n_e (10^{19} m^{-3})	1.4–5.5	2.4–6.0	4.9–9.4	7.8–8.4
I_{p} (MA)	0.6–1	0.6–1	0.8–1	0.8
$\langle B_{\mathrm{pol}} \rangle$ (T)	0.2–0.4	0.2–0.4	0.3–0.4	0.3
B_{t} (T)	2.5	1.8–3	2.5	2.5
δ	0.1–0.4	0.2–0.3	0.1–0.4	0.3

Table 5.1: Parameter range of the ASDEX Upgrade discharges analyzed.

Table 6.1 shows the parameter range covered in the database for the following quantities: the energy confinement time τ_{E}, the plasma stored energy determined from the reconstructed magnetic equilibrium W_{MHD}, the poloidal beta β_{pol}, the energy confinement time normalized to the IPB98(y,2) scaling law $H_{98\mathrm{y},2}$ [40], the heating power P_{heat}, the power crossing the separatrix given

by $P_{\mathrm{sep}} = P_{\mathrm{heat}} - \mathrm{d}W_{\mathrm{MHD}}/\mathrm{d}t - P_{\mathrm{rad}}$ where P_{rad} is the power radiated within the separatrix, the line averaged electron density n_e from the DCN interferometer channel H-1 (see subsection 4.4.3), the plasma current I_{p}, the toroidal magnetic field on the magnetic axis B_{t}, the plasma triangularity δ, and the average poloidal magnetic field $\langle B_{\mathrm{pol}} \rangle$, defined as

$$\langle B_{\mathrm{pol}} \rangle = \frac{\mu_0 I_{\mathrm{p}}}{2\pi a \sqrt{\frac{1+\kappa^2}{2}}} = \frac{\mu_0 I_{\mathrm{p}}}{2\pi a \hat{\kappa}}, \tag{5.1}$$

where a is the minor radius, κ is the elongation of the plasma and $\hat{\kappa} = \sqrt{\frac{1+\kappa^2}{2}}$.

5.2 Analysis technique

In this work, the most important measured quantities are (i) the heat flux reaching the divertor targets, (ii) the scrape-off layer (SOL) electron pressure, temperature and density decay lengths and (iii) the electron pressure profile in the confined region of the plasma.
The heat flux onto the divertor targets is inferred from surface temperature measurements obtained with infrared (IR) cameras via the procedure described in section 4.3. The sampling frequencies of the IR cameras are sufficient to resolve inter-ELM phases, as the ELM frequency of the analyzed H-mode discharges ranges between 10 and 70 Hz.
Figure 5.1 (e) shows an example of a heat flux profile measured at the upper outer divertor target during an L-mode phase of a discharge which later on develops an I-mode phase followed by a H-mode phase. The solid line is the resulting fit with the function 2.6. In order to evaluate λ_q and S within a certain time window Δt (about 50 ms), the following method is carried out: First, the fitting function is applied to each heat flux profile within the time interval. Second, only pairs of λ_q and S satisfying the condition $\lambda_q/S \geq 1.5$ are taken into account. This condition is chosen because when $\lambda_q \simeq S$, the λ_q measured at the divertor target is strongly influenced by the diffusive broadening taking place in the divertor chamber. Lastly, the medians of all the λ_q and S values within the time window are calculated. The λ_q and S time evolutions calculated with this method for the same discharge are shown in Figs. 5.1(a) and (b).
Other important quantities used in this work are the SOL electron pressure, temperature and density decay lengths. SOL profiles are routinely measured by a vertical Thomson Scattering (TS) system (see section 4.4.1), from which electron temperature and density decay lengths $\lambda_{T_e}^{\mathrm{SOL}}$ and $\lambda_{n_e}^{\mathrm{SOL}}$ can be calculated. From here on, the subscript 'SOL' is omitted for reading purposes and it will be used only when necessary.

The separatrix position is evaluated using Eq. 2.17:

$$T_e^{\mathrm{sep}} = T_{\mathrm{u}} = \left(\frac{7}{4} \frac{P_{\mathrm{sep}} L}{\kappa_0^e A_{||}^{\mathrm{SOL}}} \right)^{\frac{2}{7}}. \tag{5.2}$$

The connection length L from the outer midplane to the divertor target can be expressed as

$$L \simeq \pi q_{\mathrm{cyl}} R, \tag{5.3}$$

where

$$q_{\mathrm{cyl}} = \frac{B_{\mathrm{tor}}}{\langle B_{\mathrm{pol}} \rangle} \frac{\hat{\kappa}}{A} \tag{5.4}$$

is the safety factor for a cylindrical plasma with the aspect ratio $A = R/a$. From Eq. 2.1, the cross-sectional area of the SOL perpendicular to the magnetic field line $A_{||}^{\mathrm{SOL}}$ can be expressed as

$$A_{||}^{\mathrm{SOL}} \simeq 4\pi R \langle \lambda_q \rangle \frac{\langle B_{\mathrm{pol}} \rangle}{B_{\mathrm{tor}}}, \tag{5.5}$$

with $\langle \lambda_q \rangle$ being the poloidally averaged λ_q ($\lambda_q \simeq 0.56 \langle \lambda_q \rangle$ for typical AUG geometries [149]). By using Eqs. 5.3, 5.4 and 5.5, we rewrite Eq. 5.2 as:

$$T_e^{\mathrm{sep}} \approx \left(\frac{7}{16} \frac{P_{\mathrm{sep}} q_{\mathrm{cyl}}^2 A}{\kappa_0^e \hat{\kappa} \langle \lambda_q \rangle} \right)^{\frac{2}{7}}. \tag{5.6}$$

The separatrix temperature is evaluated with Eq. 5.6 using λ_q from IR measurements. Once T_e^{sep} is known, the separatrix position (r_{sep}) can be estimated and the subset of data between $r_{\mathrm{sep}} - 5$ mm and $r_{\mathrm{sep}} + 9$ mm is fitted with an exponential, i.e. $T_e(r) = T_e^{\mathrm{sep}} \exp(-\frac{r - r_{\mathrm{sep}}}{\lambda_{T_e}})$, to find the SOL electron temperature decay length λ_{T_e}. A similar approach is used to evaluate the SOL electron density decay length λ_{n_e}. In order to have a more robust ensemble of datapoints to minimize fitting errors, several TS profiles within a time window of about 300 ms are collected before carrying out the fit. Figures 5.1(f) and (g) show an example of edge electron temperature and density profiles mapped to the outer midplane. Once the SOL λ_{T_e} and λ_{n_e} are known, the electron pressure decay length is obtained using the relation

$$1/\lambda_{p_e} = 1/\lambda_{T_e} + 1/\lambda_{n_e}. \tag{5.7}$$

At AUG, electron temperature, density and pressure profiles within the confined region of the plasma are evaluated through integrated data analysis (IDA), see section 4.4.7. IDA profiles will be used in this work to evaluate electron temperature, density and pressure values at $\rho_{\mathrm{pol}} = 0.95$.

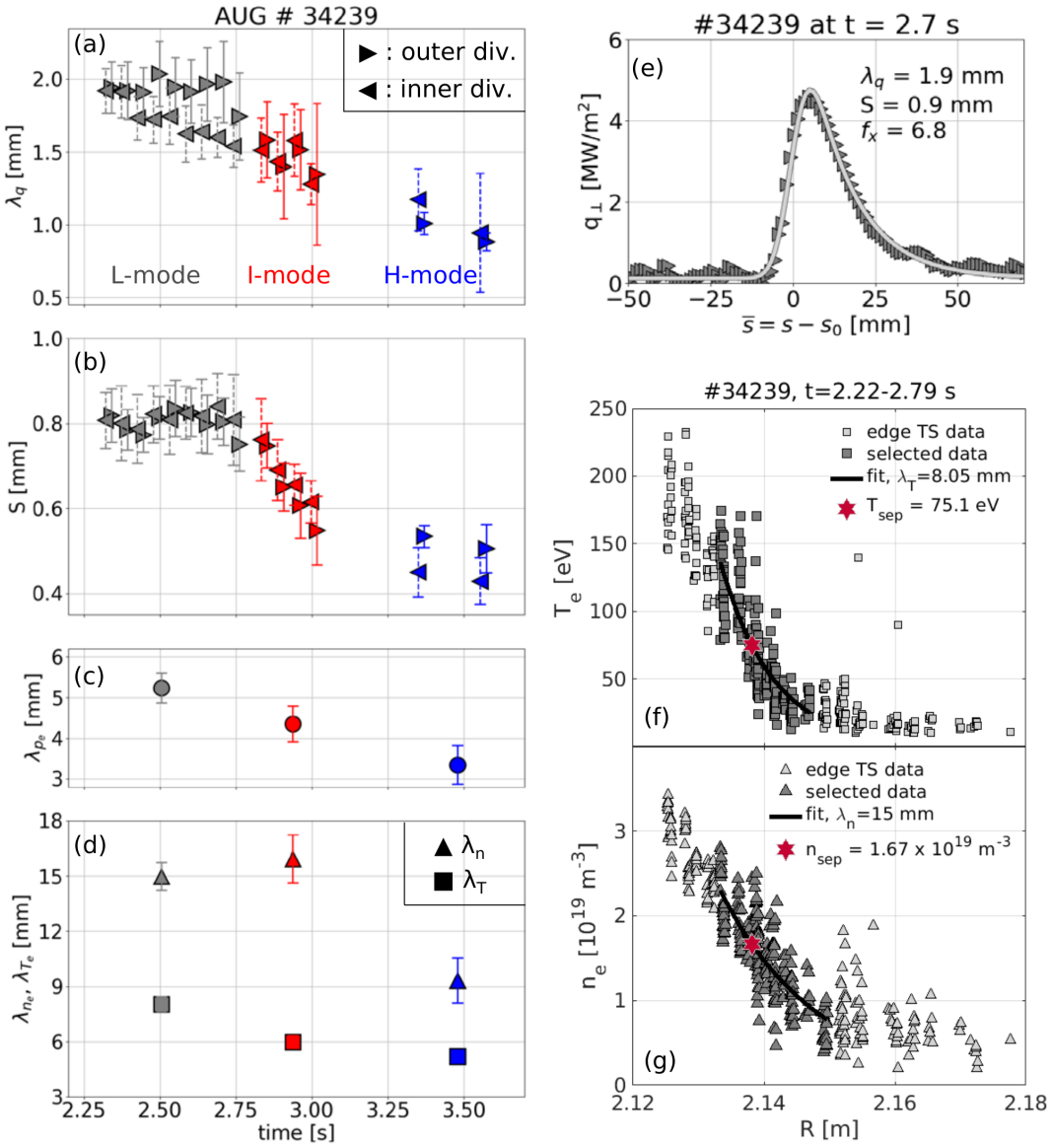

Figure 5.1: Temporal evolution of SOL and divertor parameters along discharge #34239 exhibiting different confinement regimes. Power fall-off length (a) and broadening (b) obtained from inner (◁ with dashed error bars) and outer (▷ with line error bars) divertor heat fluxes. L-mode, I-mode and H-mode phases are represented in gray, red and blue, respectively. (c) Electron pressure near-SOL decay length. (d) Near-SOL decay lengths of electron density (triangles) and temperature (squares). Panel (e) shows the perpendicular heat flux profile along the upper outer divertor and its fit with Eq. 2.6. Panels (f) and (g) show, respectively, edge electron temperature and density profiles measured by Thomson Scattering (TS). Data selected for the exponential fit are depicted in dark gray. The red stars represent the separatrix electron temperature and density.

Figure 5.1 shows an example of how SOL and divertor quantities evolve together along a discharge characterized by L-mode, I-mode and type-I-ELMy H-mode phases. Panels (a) and (b) show λ_q and S, respectively, measured at the inner ($\triangleleft$) and outer ($\triangleright$) upper divertor target and then mapped to the outer midplane. It can be seen that λ_q gradually decreases when passing from L to I-mode and it is reduced even more after the I-H transition. Note that H-mode λ_q values are about a factor of 1.8 smaller than those predicted by the scaling law in [149], which was obtained in a carbon wall environment. Further studies to address the dependency of λ_q on such plasma conditions are envisaged at AUG.
During the L-mode inner and outer divertor λ_q values show a small discrepancy, with $\lambda_q^{\text{out}} > \lambda_q^{\text{inn}}$, as already found in [57]. The observed asymmetry could be due to the vertical magnetic drifts of ions and the plasma triangularity [57,93,150]. The broadening parameter S does not show a large asymmetry between inner and outer divertors across all confinement regimes, extending to I-mode and H-mode what has been already observed in USN L-mode discharges [57]. The variation of S along the three confinement regimes is reminiscent of the λ_q change: It stays roughly constant during the L-mode phase, then it decreases during the I-mode and eventually remains constant at low values during the H-mode phase.
The SOL electron pressure decay length evolution, panel (c), closely resembles the λ_q evolution, exhibiting a constant gradual decrease going from L to I-mode and from I to H-mode. Likewise, λ_{T_e} (squares in panel (d)) shows a similar behavior to λ_{p_e}, even though its reduction passing from I to H-mode is less marked. On the other hand, λ_{n_e} (triangles in panel (d)) evolves differently: it stays roughly constant passing from L to I-mode, whereas it drops only after the I-H transition [111]. In the following, error bars will be omitted for visibility purposes. The relative error of λ_{T_e} and λ_{n_e} ranges between 5 and 15 %, while the one of λ_q varies approximately between 5 and 30 %.

5.3 Cross-regime scaling of the SOL power decay length

One of the goals of this study is to investigate whether a cross-regime λ_q scaling is better described by global or local edge plasma parameters. Global parameters are often used to describe the power decay length [54, 85, 151], since they are easier to assess and therefore provide an easy way to predict λ_q. However, they might contain less physical information, as they connect a SOL quantity to core-related parameters. On the other hand, edge local parameters might retain additional physical information and provide further insights into SOL physics; however, they are harder to evaluate, making the λ_q prediction dependent on codes or models.
A global parameter recently used for a λ_q scaling law is the volume-averaged

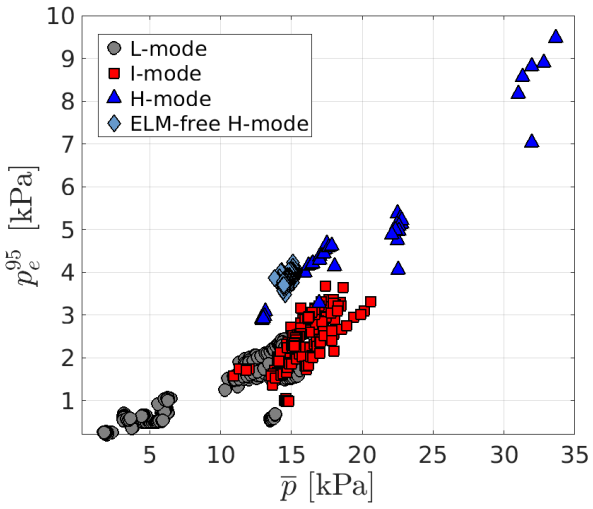

Figure 5.2: Edge electron pressure evaluated at $\rho_{\mathrm{pol}} = 0.95$ against volume-averaged plasma pressure. The database allows us to break the dependence between global and local (edge) pressure quantities.

plasma pressure defined as $\overline{p} = \frac{2}{3} W_{\mathrm{MHD}}/V$, where V is the plasma volume. A local edge parameter is for instance the edge electron pressure evaluated at $\rho_{\mathrm{pol}} = 0.95$, p_e^{95}, which represents the pedestal top electron pressure in I-mode and H-mode plasmas. Figure 5.2 illustrates the relation between these edge and core parameters for discharges in different confinement regimes, namely L-mode, I-mode, type-I ELM H-mode and ELM-free EDA H-mode. From here on, different confinement regimes will be depicted with the color and symbol code used in Fig. 5.2. Due to the H-mode data and a few L and I-mode data,

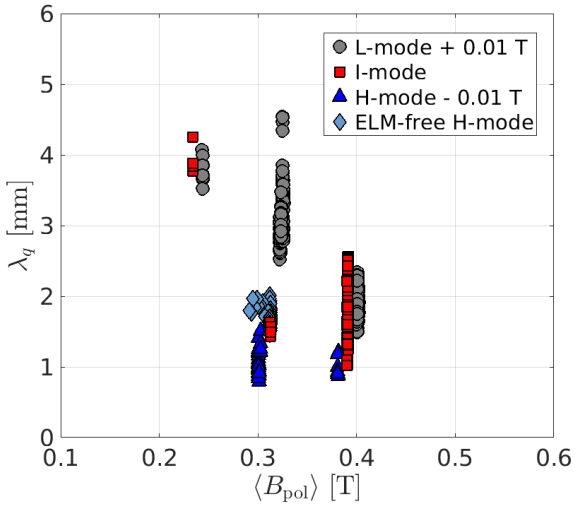

Figure 5.3: SOL power decay length λ_q against the average poloidal magnetic field. L-mode (H-mode) $\langle B_{\mathrm{pol}} \rangle$ values are shifted by + (-) 0.01 T for visibility purposes. At a fixed $\langle B_{\mathrm{pol}} \rangle$, λ_q spans over a broad range of values depending on the confinement regime.

the database allows us to disentangle the dependency between volume-averaged and edge plasma parameters.
Figure 5.3 shows the relation between the average poloidal magnetic field and λ_q. For the same $\langle B_{\mathrm{pol}} \rangle$, λ_q can assume different values depending on the confinement regime. In particular, for $\langle B_{\mathrm{pol}} \rangle = 0.31$ T, $\lambda_q \in [0.8, 4.5]$ mm, spanning from L to H-mode. This is in accordance with different pre-factors in front of H-mode and L-mode λ_q scaling laws [54, 93, 149].
Figure 5.4 (a) shows the SOL power fall-off length against the volume-averaged plasma pressure $\overline{p}$. Note that the definition of $\overline{p}$ is equivalent to the one used for the C-Mod studies in [54], which led to the scaling $\lambda_q[\mathrm{mm}] = 8.35\,(\,\overline{p}\ [\mathrm{kPa}]\,)^{-0.48}$. A nonlinear regression of the form $\lambda_q = C \times \overline{p}^{\alpha}$ is carried out and the result is shown in Fig. 5.4 (a) as a light green line. λ_q shows a correlation with $\overline{p}$ ($R^2 = 0.62$) with a similar exponent and coefficient as in the C-Mod scaling (at AUG $\alpha = -0.52$ and $C = 7.57$). However, for a volume-averaged plasma pressure of 15 kPa, λ_q shows a large scatter in the range 0.9–4 mm.

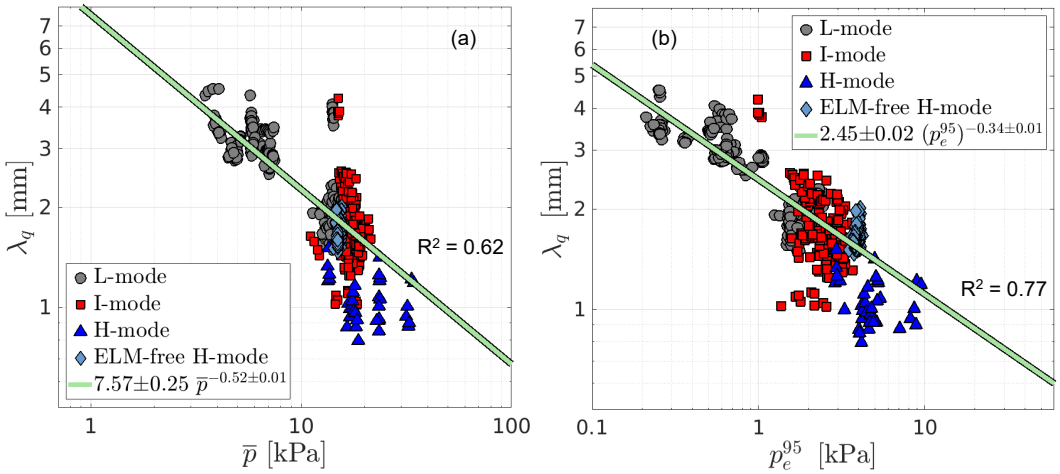

Figure 5.4: Power decay length λ_q against (a) the volume-averaged plasma pressure $\overline{p}$ and (b) edge electron pressure evaluated at $\rho_{\mathrm{pol}} = 0.95$, p_e^{95}. Light green lines represent the results of a nonlinear regression of the form $\lambda_q = C \times X^{\alpha}$. The respective R^2 values are shown in the picture.

Figure 5.4 (b) shows the relation between λ_q and the edge electron pressure, p_e^{95}. A nonlinear regression yields ($R^2 = 0.77$):

$$\lambda_q[\mathrm{mm}] = 2.45 \pm 0.02 \times (\,p_e^{95}\ [\mathrm{kPa}]\,)^{-0.34\pm0.01}. \tag{5.8}$$

The regression describes L-mode, I-mode and stationary ELM-free H-mode data well, while representing an upper boundary for inter-type-I ELM H-mode data. A conservative scaling for the inter-type-I ELM H-mode data is given by halving the regression coefficient. Overall, this regression is broadly consistent with the scaling found at Alcator C-Mod, since all data from different confinement regimes correlate well with one plasma parameter related to the plasma pressure; however, at AUG the edge electron pressure is found to be a more

suitable parameter for a λ_q scaling than a volume-averaged plasma quantity, such as $\overline{p}$. Indeed, as an edge local plasma parameter, p_e^{95} should be more related to the SOL physics setting λ_q than a global quantity such as $\overline{p}$. This consideration is also supported by recent simulations with a fluid turbulence code HESEL, which show that simulated L-mode λ_q values scale remarkably well with the electron or ion pressure gradient across the separatrix [152].
It should be also noted that the present scaling law has been obtained with discharges characterized by attached divertor conditions and no impurity seeding. However, within these two operational constraints, which were necessary to guarantee high-quality heat flux measurements, plasma conditions were strongly varied. The database contains not only a large variety of pedestal profiles, but also L-mode and H-mode discharges with different ion ∇B drift directions and different divertor geometries. Therefore, it is important to notice the generality of this scaling, which may highlight a possible unified physics mechanism setting λ_q across different confinement regimes.

#	C	p_e^{95} [kPa]	$\overline{p}$ [kPa]	T_e^{95} [keV]	n_e^{95} [10^{19} m^{-3}]	$\langle B_{\mathrm{pol}} \rangle$ [T]	R^2
1	2.45	−0.34	—	—	—	—	0.77
2	7.57	—	−0.52	—	—	—	0.62
3	0.95	—	—	−0.67	—	—	0.29
4	3.37	—	—	—	−0.43	—	0.71
5	0.55	—	—	—	—	−1.23	0.19

Table 5.2: Overview of selected regression results.

Table 5.2 summarizes the results of nonlinear regressions of the form $\lambda_q = C \times X^{\alpha}$ applied to different parameters. In particular, the low R^2 value obtained when T_e^{95} is used in the nonlinear regression ($R^2 = 0.29$) should be noted, in contrast to the high values obtained with p_e^{95} ($R^2 = 0.77$) and n_e^{95} ($R^2 = 0.71$). Therefore, the edge electron temperature is found to be a weak parameter for describing a cross-regime λ_q scaling, in contrast to what has been found when analyzing L-mode data alone [93, 153].

5.4 Correlation between SOL and pedestal electron pressure gradients

To further investigate the reasons for the λ_q correlation with p_e^{95}, Fig. 5.5 shows the relation between λ_q and two edge electron pressure quantities: the SOL electron pressure decay length at the outer midplane $\lambda_{p_e}^{\mathrm{SOL}}$ (panel (a)), which has been calculated with Eq. 5.7, and the pedestal electron pressure gradient length $L_{p_e}^{\mathrm{ped}}$ (panel (b)). If the pedestal profile is best described by a straight line, as suggested in [154], $L_{p_e}^{\mathrm{ped}}$ can be simply estimated by:

$$L_{p_e}^{\mathrm{ped}} = -\frac{p_e}{\nabla p_e} \approx \frac{p_e^{95} + p_e^{\mathrm{sep}}}{2} \cdot \frac{R^{\mathrm{sep}} - R^{95}}{p_e^{95} - p_e^{\mathrm{sep}}}, \tag{5.9}$$

where the subscripts 'sep' and '95' denote values taken at the separatrix and $\rho_{\mathrm{pol}} = 0.95$, respectively. Both p_e^{sep} and R_{sep} are calculated with the method described in section 5.2.

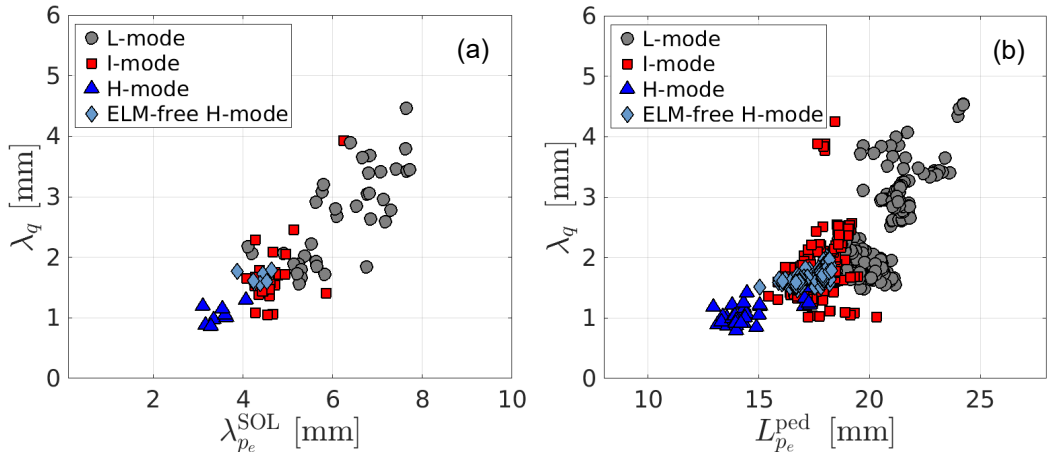

Figure 5.5: SOL power decay length λ_q against (a) SOL electron pressure decay length and (b) pedestal electron pressure gradient length, $L_{p_e}^{\mathrm{ped}}$. L-mode, I-mode, inter-ELM H-mode and EDA H-mode data are represented in gray circles, red squares, blue triangles and light blue diamonds, respectively.

A clear correlation can be noted between λ_q and both $\lambda_{p_e}^{\mathrm{SOL}}$ and $L_{p_e}^{\mathrm{ped}}$, in particular, λ_q rises as the gradients get more shallow. Also, the correlations show a similar trend: Above the values of $\lambda_{p_e}^{\mathrm{SOL}} \simeq 5.5$ mm and $L_{p_e}^{\mathrm{ped}} \simeq 19$ mm λ_q increases more strongly. This change coincides with the transition from I to L-mode and could reflect the larger transport coefficients usually found at the edge of L-mode plasmas. Also, it is worth noting the different absolute values of the pedestal and SOL gradient lengths, with the gradient in the SOL being steeper than in the pedestal. This observation is in accordance with what was previously found at Alcator C-Mod [91] and with 2D-fluid edge simulations [155], namely that the electron pressure gradient exhibits a maximum in the near-SOL. What should be retained from Fig. 5.5 is that the steepening of edge pressure profiles (i.e. an increase of pedestal and core pressures) is statistically associated with a reduction of λ_q. Note that this relation is present across all regimes analyzed.

This observation may have important consequences for next step devices, since the ultimate goal of a fusion power plant is to combine high core plasma pressure (which means steep pedestal pressure gradients, as core profiles are mainly stiff) with a viable power exhaust solution, which largely depends on λ_q [156–158].

Figure 5.6 shows the relation between pedestal and SOL electron pressure gradients $1/L_{p_e}^{\mathrm{ped}}$ and $1/\lambda_{p_e}^{\mathrm{SOL}}$, respectively, here normalized to the AUG major radius of $R = 1.65\,\mathrm{m}$. Remarkably, SOL and pedestal gradients appear to be linearly correlated across all confinement regimes, namely an increase of $R/\lambda_{p_e}^{\mathrm{SOL}}$ corresponds to an according increase of $R/L_{p_e}^{\mathrm{ped}}$. To quantify their

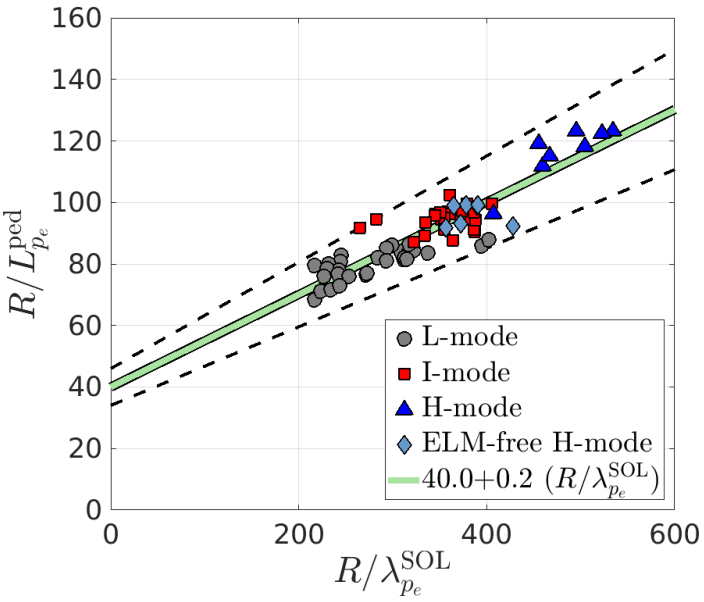

Figure 5.6: Normalized pedestal electron pressure gradient against the normalized SOL electron pressure gradient. The result of a linear fit is depicted as a green line. Dashed black lines represent the 15 % error boundaries that encompass all data. Remarkably, SOL and pedestal electron pressure gradients are correlated across all confinement regimes.

relationship, a linear fit is applied to the data yielding ($R^2 = 0.83$)

$$\frac{R}{L_{p_e}^{\mathrm{ped}}} = 39.4 + 0.2 \cdot \frac{R}{\lambda_{p_e}^{\mathrm{SOL}}}. \tag{5.10}$$

Data are all contained within the 15 % error boundaries plotted in Fig. 5.6 as black dashed lines. The reasons for the existence of an offset are unclear at this stage.

5.5 SOL electron temperature and density decay lengths

In this section, the relationship between experimental λ_q, λ_{T_e} and λ_{n_e} values in the SOL is studied across different confinement regimes. As already shown in Fig. 5.1(d) and in [111, 159], SOL electron temperature and density decay lengths behave differently in L-mode, I-mode and H-mode discharges. Figure 5.7 (a) shows the relation between electron temperature λ_{T_e} and density λ_{n_e} decay lengths across all analyzed confinement regimes. H-mode discharges (both ELMy and stationary ELM-free H-mode) are characterized by short temperature and density decay lengths, whereas L-mode discharges usually exhibit longer decay lengths. L-mode discharges close to the L-H transition, however, can feature short temperature decay lengths, similar to those of H-mode

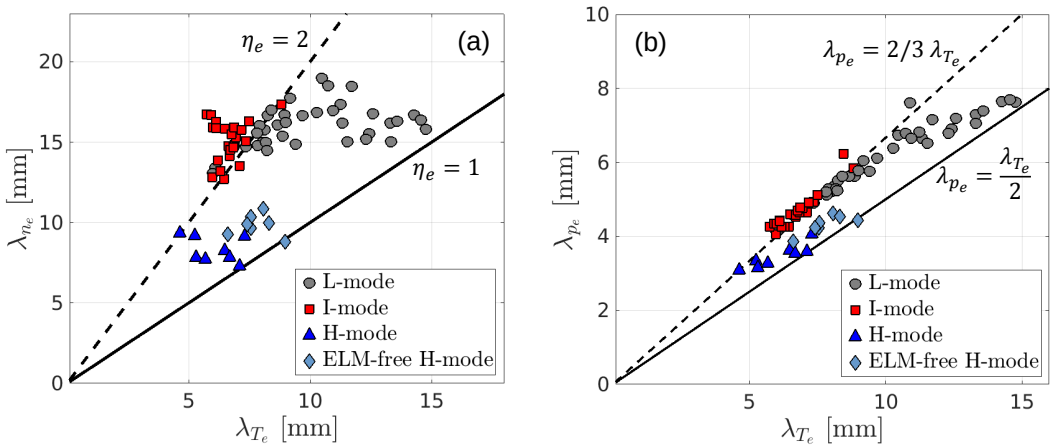

Figure 5.7: SOL electron density decay length (a) and SOL electron pressure decay length (b) against SOL electron temperature decay length across different confinement regimes. In panel (a) dashed and solid lines represent $\eta_e = 2$ and $\eta_e = 1$, respectively, with $\eta_e = \lambda_{n_e}/\lambda_{T_e}$ being the gradient length ratio. In panel (b), the relations $\lambda_{p_e} = 2/3\,\lambda_{T_e}$ and $\lambda_{p_e} = \lambda_{T_e}/2$ are depicted as a dashed and solid line, respectively.

discharges close to the L-H transition, such as stationary ELM-free H-mode discharges. On the other hand, I-mode discharges show small λ_{T_e} and large λ_{n_e} values. This general behavior is reminiscent of the electron temperature and density pedestal evolution. In Fig. 5.7 (a), two lines representing different gradient length ratios $\eta_e = \lambda_{n_e}/\lambda_{T_e} = 1$ and $\eta_e = 2$ are depicted. L-mode and H-mode discharges exhibit $1 \leq \eta_e \leq 2$. This is in line with previous studies conducted at AUG for the type-I ELMy H-mode regime [56]; however, I-mode discharges are characterized by $\eta_e \geq 2$, due to their H-mode-like λ_{T_e} value of about 7 mm and L-mode-like λ_{n_e} values around 15 mm. This is highlighting the decoupling of SOL electron density and temperature transport that occurs in I-mode plasmas.

Figure 5.7 (b) shows the relation between λ_{p_e} and λ_{T_e}, which are linked through $1/\lambda_{p_e} = 1/\lambda_{T_e} + 1/\lambda_{n_e}$. Substituting $\eta_e = 1$ and $\eta_e = 2$ in the previous formula, one can find the corresponding relations between SOL electron pressure and temperature decay lengths, which are $\lambda_{p_e} = \frac{1}{2}\,\lambda_{T_e}$ and $\lambda_{p_e} = \frac{2}{3}\,\lambda_{T_e}$, respectively. As expected, most of the dataset lies between those two lines except for the I-mode discharges, which have $\eta_e > 2$.

What should be retained from this graph is that λ_{p_e} and λ_{T_e} remain interconnected, even though I-mode discharges have allowed us to enlarge the variation in the λ_{n_e}-λ_{T_e} diagram. For this reason, disentangling λ_{T_e} and λ_{p_e} dependencies in the SOL with the present database is not possible. Nevertheless, the variety of combinations of density and temperature SOL decay lengths, obtained thanks to the cross-regime analysis, allows us to study their single effect on λ_q.

Figure 5.8 (a) shows the relation between experimentally measured λ_q and the electron temperature SOL decay length λ_{T_e} across the different confinement

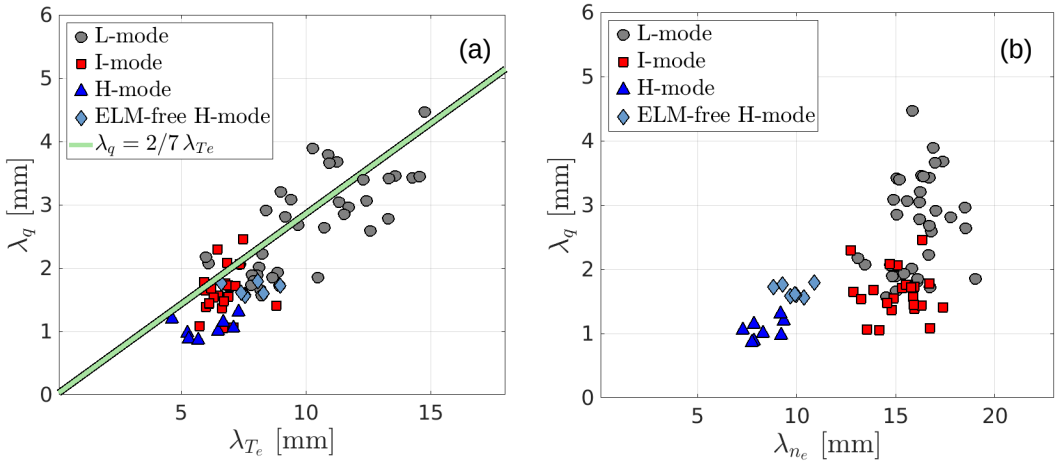

Figure 5.8: SOL power decay length λ_q against SOL electron temperature (a) and electron density (b) decay lengths. The light green line in panel (a) represents expected values of λ_q in the Spitzer-Härm electron heat conduction regime.

regimes. If in the SOL most of the parallel heat transport is due to electron conduction, λ_q and λ_{T_e} are related by the formula $\lambda_q = \frac{2}{7}\lambda_{T_e}$ [45]. Previous studies at AUG have shown that this relation holds in L-mode [57], in a single I-mode discharge [111] and H-mode discharges [56] (in the latter case λ_{T_e} was compared with λ_q estimated by scaling laws). Figure 5.8 (a) shows that all data from different confinement regimes cluster around the line $\lambda_q = \frac{2}{7}\lambda_{T_e}$. Therefore, it can be concluded that at ASDEX Upgrade the Spitzer-Härm electron heat conduction assumption can explain the connection between λ_{T_e} measured upstream and λ_q measured at the target. Figure 5.8 (b) shows the relation between λ_q and λ_{n_e}. For $\lambda_q \approx 1.5$ mm, λ_{n_e} ranges between 7 and 20 mm. On the other hand, for $\lambda_{n_e} \approx 17$ mm, λ_q shows a large variation from 1 mm to about 4.5 mm. This plot suggests a weaker role of the SOL electron density decay length in setting λ_q, when compared to that of λ_{T_e}.

5.6 Out-in divertor heat flux asymmetries

In this section, heat flux asymmetries between the inner and outer divertor targets are investigated across different confinement regimes. To carry out this analysis, the database described in section 5.1 has been restricted to the discharges with both inner and outer divertor data. Those are USN plasma discharges, since in this configuration the IR camera is able to measure on both inner and outer targets, as shown in section 4.3. Moreover, here a further distinction in our dataset is introduced: not only different confinement regimes but also discharges in favorable and unfavorable configurations are differentiated. This is because out-in divertor asymmetries are highly dependent on the direction of SOL $\vec{E} \times \vec{B}$ drifts, which change from favorable to unfavorable configuration as discussed in section 2.1.6.

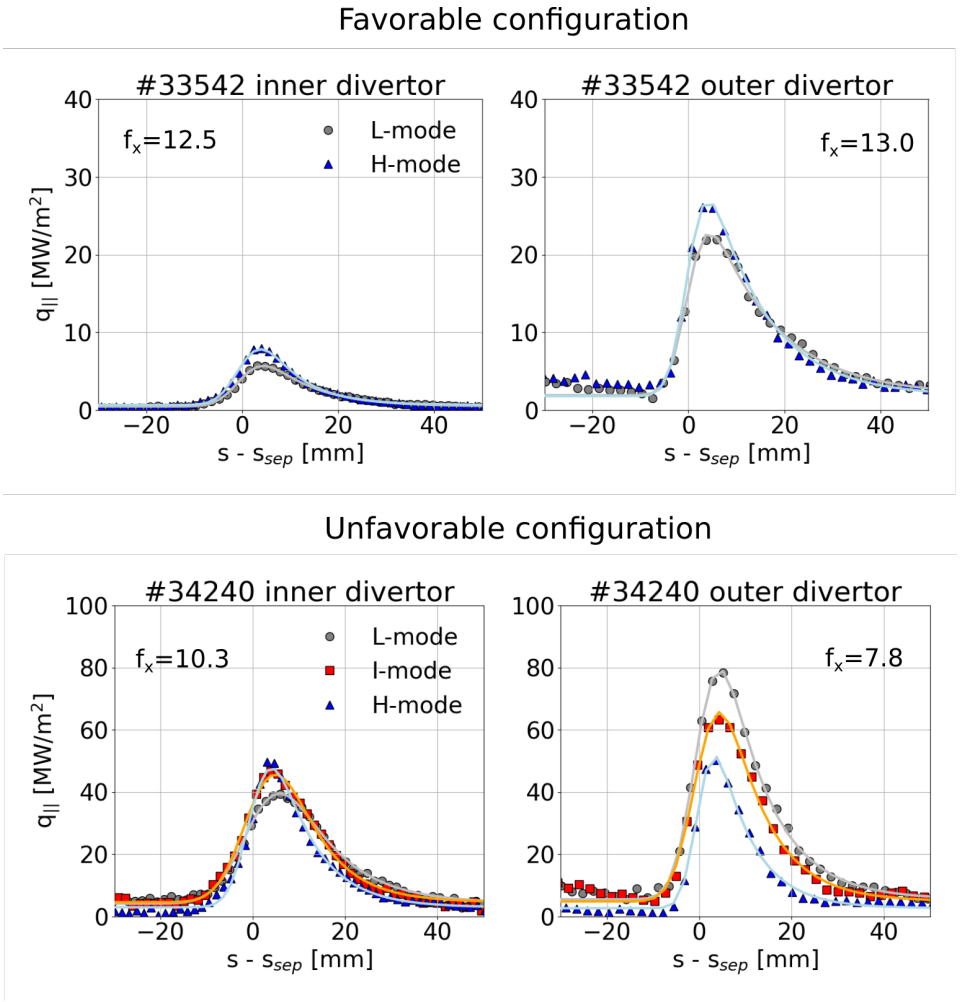

Figure 5.9: Parallel heat flux profiles onto the inner (left) and outer (right) upper divertor targets in favorable (top) and unfavorable (bottom) configuration. Different confinement regimes are compared: L-mode (gray circles), I-mode (red squares) and H-mode (blue triangles). Solid lines represent the profile fit with Eq. 2.6. The flux espansion f_x from the outer midplane to the target is specified in each panel.

Figure 5.9 shows an example of parallel heat flux profiles onto the inner and outer divertor targets in different confinement regimes. In favorable configuration (top panels), a large out-in asymmetry is observed, i.e. the parallel peak heat flux is about 3 times larger on the outer target than on the inner one. Also, going from L to H-mode the out-in asymmetry is largely unchanged; the peak heat flux increases on both targets due to the slight increase of external heating power needed to enter H-mode.
In unfavorable configuration (bottom panel), the out-in asymmetry is reduced. However, in this case the out-in asymmetry changes with confinement regimes; going from L to I-mode, the peak heat flux reduces on the outer and increases on the inner target. This phenomenon repeats after the I-H transition, almost equalizing the peak parallel heat flux on inner and outer targets. Also, note

that the power decay length λ_q decreases while transiting from L to H-mode, as already shown in Fig. 5.1 (a). Since both λ_q and the peak heat flux decrease on the outer target after the L-I and I-H transition, the power on the outer target is reduced going from L to I-mode and from I to H-mode.

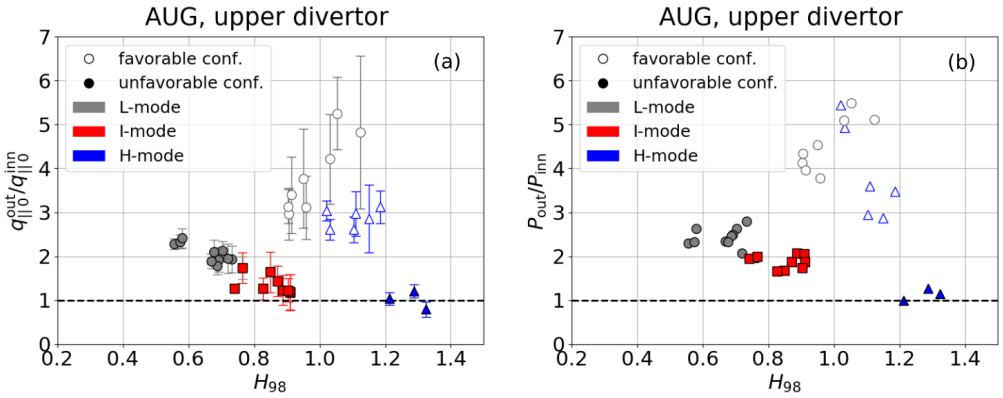

Figure 5.10: Out-in ratio of the parallel peak heat flux at the divertor entrance (a) and of the power reaching the divertor targets (b) vs. confinement factor H_{98} for L-mode (gray circles), I-mode (red squares) and H-mode (blue triangles) discharges. Empty and filled symbols represent discharges in favorable and unfavorable configuration, respectively. I-mode plasmas feature a reduced out-in asymmetry w.r.t. H-mode plasmas in favorable configuration.

Figure 5.10 shows the out-in ratio of the parallel peak heat flux at the divertor entrance $q_{||0}$ (a) and of the power reaching the divertor (b) against H_{98} for the entire analyzed database. Overall, the strongly unbalanced asymmetry towards the outer divertor target observed in favorable configuration is reduced in unfavorable configuration. This result is in agreement with previous studies carried out at the JET tokamak with discharge-integrated thermocouple measurements [58], and can be explained by the effect of $\vec{E} \times \vec{B}$ drifts, see Fig. 2.6 (b). In unfavorable configuration, SOL $\vec{E} \times \vec{B}$ drifts contribute to reduce the temperature and density asymmetry between inner and outer targets. As a consequence, also the heat flux asymmetries are reduced.
However, the present dataset allows us to go in more detail, since it contains information on the heat flux profile on both divertor targets. In favorable configuration, the out-in ratio of the parallel peak heat flux at the divertor entrance ranges between 2.5 and 5. There is no substantial variation of this ratio between L-mode and H-mode discharges within the error bars. Conversely, in unfavorable configuration the out-in ratio of the parallel peak heat flux at the divertor entrance varies between 2.3 and 0.8, and a significant variation of this ratio is observed across confinement regimes: In L-mode it is around 2, in I-mode around 1.3 and in H-mode around 1. In other words, $q_{||0}^{\mathrm{out}}/q_{||0}^{\mathrm{inn}}$ is approaching 1 from L-mode to I-mode and it reaches 1 in H-mode.
The overall picture is largely unchanged when the out-in power ratio is considered, see Fig. 5.10 (b). In favorable configuration the out-in power ratio ranges

between 3 and 5.5, whereas in unfavorable configuration varies between 3 and 1. From Eq. 2.9 the power onto the divertor targets can be expressed as

$$P_{\mathrm{div}} = 2\pi R_{\mathrm{div}} q_{\perp\,\mathrm{max}} f_{\mathrm{tor}} \lambda_{\mathrm{int}} f_x, \tag{5.11}$$

where $q_{\perp\,\mathrm{max}}$ is the perpendicular peak heat flux on the target and f_x is the flux expansion from the outer midplane to the target. In the upper divertor of AUG $f_{\mathrm{tor}} = 1$, since the tiles are not toroidally tilted. The power on the divertor can be rewritten as a function of the peak heat flux at the divertor entrance q_0 by noting that

$$q_{\perp\,\mathrm{max}} \lambda_{\mathrm{int}} = q_{\perp 0} \lambda_q, \tag{5.12}$$

as the convolution of the exponential with the Gaussian function in Eq. 2.4 leaves unchanged the value of the integral over the profile [151]. Therefore, the power on the divertor can be calculated as

$$P_{\mathrm{div}} = 2\pi R_{\mathrm{div}} q_{||0} \lambda_q f_x \sin(\alpha), \tag{5.13}$$

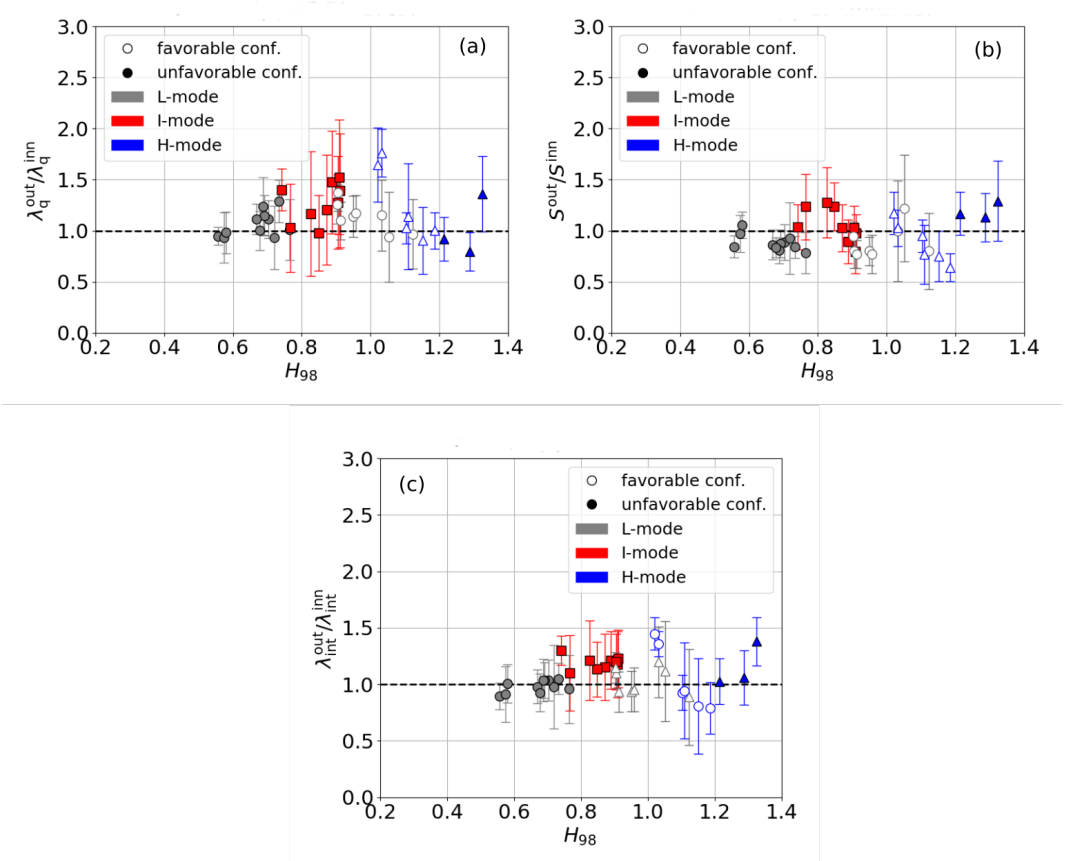

Figure 5.11: Out-in ratio of the power decay length λ_q (a), the broadening parameter S (b) and the integral power decay length λ_{int} (c) mapped to the outer midplane vs. H_{98} for L-mode (gray circles), I-mode (red squares) and H-mode (blue triangles) discharges in USN configuration. Empty and filled symbols represent discharges in favorable and unfavorable configuration, respectively.

where $q_{\perp 0} = q_{||0}\sin(\alpha)$ has been used. In AUG, $R^{\text{out}}_{\text{div}}/R^{\text{inn}}_{\text{div}} = 1.1$ and this is contributing to slightly increase $P_{\text{out}}/P_{\text{inn}}$ w.r.t. $q^{\text{out}}_{||0}/q^{\text{inn}}_{||0}$. The out-in ratio of $f_x\sin(\alpha)$ is very close to one due to the interconnection between f_x and $\sin(\alpha)$, see section 2.1.1 for more details. The out-in ratio of λ_q, S and λ_{int} can be different from 1, as shown in Fig. 5.11; however, deviations from 1 are pretty small and, overall, the out-in ratio of these quantities ranges between 0.5 and 1.5. For these reasons, the $P_{\text{out}}/P_{\text{inn}}$ ratio is mainly set by $q^{\text{out}}_{||0}/q^{\text{inn}}_{||0}$, as confirmed by Fig. 5.10.

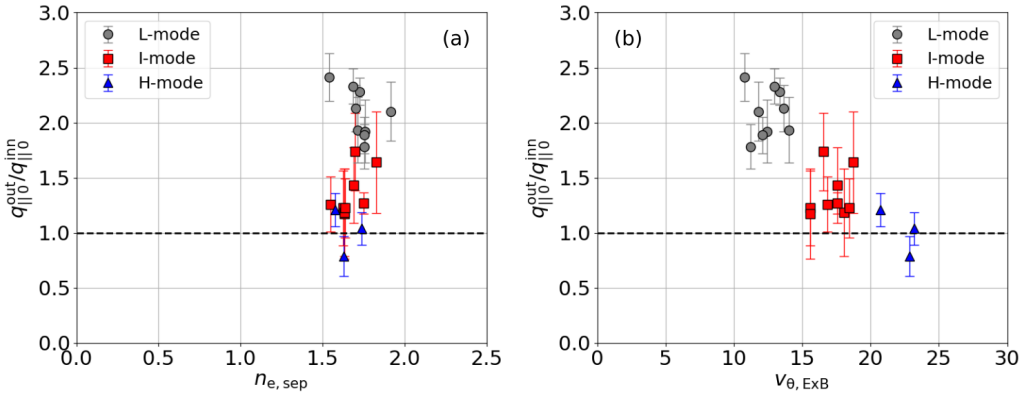

Figure 5.12: Out-in ratio of the parallel peak heat flux at the divertor entrance vs. (a) the separatrix density and (b) the poloidal $\vec{E}\times\vec{B}$ drift velocity in the SOL, calculated with Eq. 2.23. Data for L-mode, I-mode and H-mode in unfavorable configuration are shown.

An interesting finding is the change of out-in asymmetry at the L-I and I-H transitions in unfavorable configuration. This change is not due to a variation of the SOL density, as shown in Fig. 5.12 (a). The separatrix density stays approximately constant across these different plasma phases. What varies considerably, though, is the electron temperature SOL decay length and the separatrix electron temperature; the former becomes shorter from L to I-mode and reduces further from I to H-mode, the latter increases going from L to H-mode due to the reduction of λ_q. These two changes in the SOL contribute to an increase in the poloidal $\vec{E}\times\vec{B}$ drift velocity (see Eq. 2.23), which doubles going from L-mode to H-mode as shown in Fig. 5.12. In unfavorable configuration, the poloidal $\vec{E}\times\vec{B}$ drift is directed along the SOL from the outer to the inner target, see Fig. 2.6. Therefore, it is speculated that this increase in the poloidal $\vec{E}\times\vec{B}$ drift strength contributes to balance further the out-in asymmetry at the targets. More detailed analysis with SOL 2D multi-fluid transport codes, such as SOLPS [160], are necessary to investigate this hypothesis.

Fig. 5.10 (a) compares the different confinement regimes w.r.t. two figures of merit: H_{98}, which is a measure of energy confinement quality, and $q^{\text{out}}_{||0}/q^{\text{inn}}_{||0}$, which is a measure of power sharing between the divertor targets. The higher H_{98}, the better energy confinement and hence fusion energy production. The

more $q_{||0}^{\text{out}}/q_{||0}^{\text{inn}}$ is close to 1, the better the power exhaust is distributed between the targets. H-mode plasmas in unfavorable configuration are the discharges that better optimize these two figures of merit, as they reach high H_{98} values and $q_{||0}^{\text{out}}/q_{||0}^{\text{inn}}$ close to 1. However, H-mode plasmas in unfavorable configuration require about double of the external heating power to be accessed than in favorable configuration [102]. For this reason, they are not considered as a viable scenario for a fusion power plant.
It is interesting to compare I-mode and H-mode plasmas in favorable configuration, as they require comparable external heating power to be accessed in present-day machines. The I-mode has a slightly lower H_{98} value than the H-mode; however, it has a more favorable out-in sharing than the H-mode, namely $q_{||0}^{\text{out}}/q_{||0}^{\text{inn}} \simeq 1.3$ in I-mode while $\simeq 2.9$ in H-mode in favorable configuration. Indeed, in a fusion power plant the divertor targets will be detached; however, in case of a transient plasma re-attachment the peak divertor heat flux will be more tolerable if $q_{||0}^{\text{out}}/q_{||0}^{\text{inn}} \simeq 1$.

5.7 Discussion

Results from previous sections highlight a correlation between SOL and pedestal electron pressure gradients that holds across all analyzed confinement regimes (Fig. 5.6). This finding allows us to address two main points: The nature of the λ_q scaling with p_e^{95} and the connection between SOL and edge confined regions.

5.7.1 The nature of λ_q scaling with p_e^{95}

In this chapter, it has been shown that pedestal and SOL electron pressure gradient lengths exhibit a linear correlation $L_{p_e}^{\text{ped}} \propto \lambda_{p_e}^{\text{SOL}}$, see Fig. 5.6. Additionally, assuming a fixed pedestal width, $p_e^{95} \propto L_{p_e}^{\text{ped}}$. From these two considerations, a correlation between the pedestal top electron pressure and the SOL electron pressure gradient length follows, $p_e^{95} \propto \lambda_{p_e}^{\text{ped}}$. This correlation is shown in Fig. 5.13, where $\lambda_{p_e}^{\text{SOL}}$ is plotted against p_e^{95}
Note that data in Fig. 5.13 are displayed in log-log scale, hence a power relationship is present:

$$\lambda_{p_e}^{\text{SOL}}[\text{mm}] = 5.89 \pm 0.03 \times (\, p_e^{95}\,[\text{kPa}]\,)^{-0.25\pm0.01}. \tag{5.14}$$

Considering now that λ_q and $\lambda_{p_e}^{\text{SOL}}$ are related to each other (see Fig. 5.5(a)), the correlation between λ_q and p_e^{95} is thus a consequence. Therefore, the link between SOL and pedestal electron pressure gradients ultimately leads to a scaling of the power decay length λ_q with the pressure at the pedestal top p_e^{95}. The Alcator C-Mod scaling of λ_q with $\bar{p}$ could be due to the same link between pedestal and SOL electron pressure gradients, as also supported by their observation of a correlation between λ_q, λ_{p_e} and the pedestal pressure evolution [161].

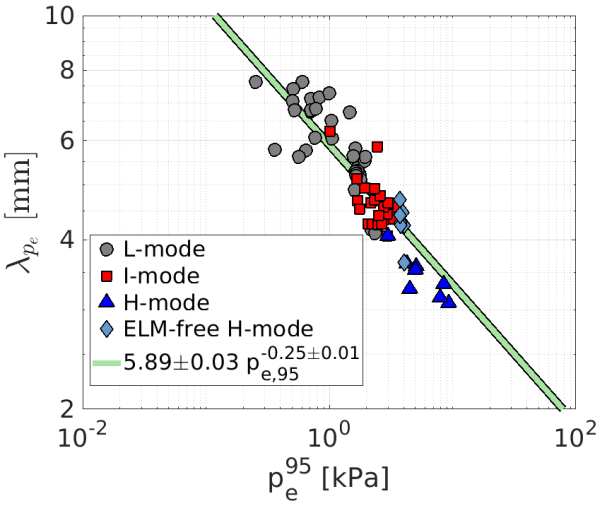

Figure 5.13: SOL electron pressure decay length against the electron pressure at $\rho_{\mathrm{pol}} = 0.95$ across different confinement regimes. Data are plotted in logarithmic scale. A correlation is present between the edge electron pressure and the SOL pressure decay length.

5.7.2 The connection between SOL and edge region

It is remarkable that a SOL quantity ($\lambda_{p_e}^{\mathrm{SOL}}$), which is set by the competition between parallel and perpendicular transport, and $L_{p_e}^{\mathrm{ped}}$, a quantity of the plasma confined region that is set by perpendicular transport alone, are related; however, experimental profiles measured around the separatrix show one characteristic decay length when plotted in logarithmic scale [56,91]. Also, simulations carried out with the 2D drift-fluid turbulence code ESEL [155] show no abrupt change of edge temperature and density profiles around the separatrix. These experimental and numerical evidences point towards a connection between near-SOL and pedestal regions.
For completeness, it should be mentioned that in nitrogen seeded discharges at AUG, a de-correlation between pedestal top electron pressure and SOL electron temperature decay length has been observed [159]; however, it could be that the aforementioned correlation between SOL and pedestal electron pressure gradients is still retained, with the difference being that in this case, a larger pedestal top value is achieved due to the inward shift of the pedestal profile, which is typical of N seeded discharges [162].
Evidence of a connection between SOL and confined edge region is also given by recent experiments carried out at the TJ-II stellarator [163]. It was observed that turbulence spreading in the SOL, i.e. nonlocal turbulent transport, decreases when a transport barrier in the plasma edge is present, i.e. when turbulence is reduced at the edge plasma. This suggests that the turbulence in the SOL comes from the confined edge, tightly binding the two regions.
An interesting physical picture that allows us to interpret the observed correlation between SOL and pedestal pressure gradients is given in [91, 161]. As

shown in these papers, the edge pressure gradient appears to be set by a critical gradient determined by electromagnetic fluid drift turbulence, rather than a classical diffusive-like transport. In other words, the edge electron pressure gradient adjusts to satisfy a marginal stability constraint. In such a picture, the correlation between near-SOL and pedestal gradients can be interpreted as the need for both gradients to satisfy the same marginal stability constraints.

In conclusion, the main consequence of these observations is that the pedestal electron pressure gradient and the SOL power decay length λ_q are linked. In other words, across the confinement regimes analyzed, it is difficult to combine a large λ_q with a steep pedestal electron pressure gradient. This would not be an obstacle to obtain high core pressures if the pedestal width could be freely enlarged and, consequently, high pedestal top values could be reached. Unfortunately, the pedestal width is not largely varying, except for some particular cases [162,164]. Therefore, the highlighted coupling of SOL and pedestal electron pressure gradients may be an obstacle to finding a stable scenario that couples high core performances and a relaxed power exhaust solution.
Turning our attention to ITER, the scaling law presented here (Eq. 5.8) predicts for the baseline H-mode scenario with $Q = 10$ $\lambda_{q,\mathrm{ITER}} \simeq 0.6\,\mathrm{mm}$. This adds up to other experimental scaling laws [53, 54] that foresee $\lambda_{q,\mathrm{ITER}}$ to be in the same range of values. With regard to I-mode plasmas, they exhibit a lower edge electron pressure than H-mode due to the lack of a density pedestal. Therefore, from this analysis a larger λ_q is expected in I-mode than in H-mode. However, when reactor-relevant pedestal top electron pressures are considered [165], the scaling law presented here predicts only a marginal increase of λ_q, which passes from about 0.6 mm to 0.65 mm. Hence, to make steady-state divertor heat loads tolerable, similar challenges will need to be faced for both I-mode and H-mode plasmas.

Chapter 6

I-mode pedestal relaxation events

This chapter presents a detailed investigation of the I-mode 'ELM-like' events recently observed in ASDEX Upgrade, shedding light on their appearance, characteristics and divertor heat loads[1].
First of all, it is worth clarifying that these events exhibit macroscopic differences with respect to the previously studied I-mode bursts in AUG [104, 110], described in section 3.2.2. Unlike the latter, the events considered here exhibit ELM-like timescales, a characteristic frequency of appearance, and an ELM-like divertor signature. In addition, they cause a full relaxation of edge profiles, observed in both the electron temperature and density. No statement can be made with regard to the ion temperature due to diagnostic time resolution restrictions. Therefore, hereinafter they are referred to as I-mode pedestal relaxation events (PREs).

6.1 Domain of existence

In this section, the domain of existence of I-mode PREs in AUG w.r.t. local plasma parameter (n_e, T_e) is investigated both in deuterium and hydrogen plasmas. In each subsection, time traces of several plasma quantities during typical discharges with PREs are shown.

6.1.1 Appearance in deuterium I-mode plasmas

Figure 6.1 shows a plasma discharge in the typical I-mode parameter range of ASDEX Upgrade, i.e. $I_p = 1\,\mathrm{MA}$, $B_\mathrm{t} = -2.5\,\mathrm{T}$ and with a line-averaged core electron density of about $5 \times 10^{19}\mathrm{m}^{-3}$ (see panel (c)). The deuterium plasma is heated with 1.5 MW of ECRH power and (modulated) co-current NBI power (see panel (a)). The NBI power is ramped linearly until $t = 2\,\mathrm{s}$ when the NBI feedback control on the β_pol value takes over (panel (b)), similarly to [111]. At

[1] Part of the content of this chapter is published in Ref. [166]

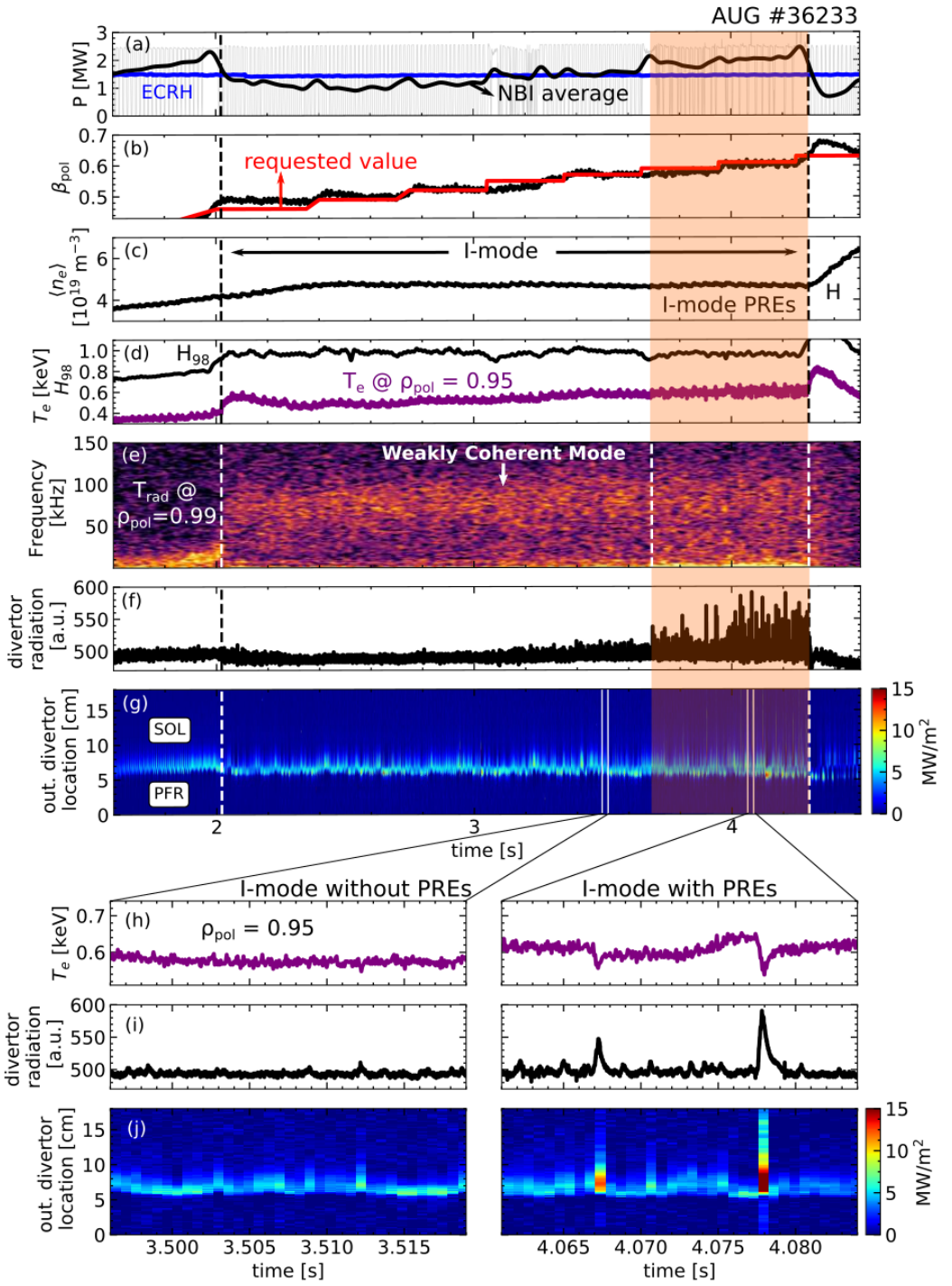

Figure 6.1: Appearance of I-mode PREs in an AUG USN discharge. (a) ECRH (blue) and NBI (black) power. (b) Requested β_{pol} (red) and measured value (black). (c) Line-averaged core electron density. (d) Electron temperature at $\rho_{\mathrm{pol}} = 0.95$ (purple) and H_{98} (black). (e) Spectrogram of ECE temperature measured at $\rho_{\mathrm{pol}} = 0.99$. (f) Radiation measured by a diode bolometer with line of sight in the upper divertor region. (g) Heat flux onto the upper outer divertor target. Panels (h), (i) and (j) show a magnification of the pedestal top electron temperature, divertor radiation and outer divertor heat flux, respectively, in two different time windows with and without PREs.

$t = 2.02\,\mathrm{s}$ the transition from L to I-mode occurs, which is seen from the sudden increase in the electron temperature at $\rho_{\mathrm{pol}} = 0.95$ and from the increase in the confinement quality factor H_{98} (panel (d)). The weakly coherent mode (WCM) appears in the spectrogram of the ECE temperature (panel (e)) measured at $\rho_{\mathrm{pol}} = 0.99$. Simultaneously, since due to improved confinement the measured β_{pol} becomes larger than the requested one, the NBI power is reduced to match the two values. This reduction in the NBI power is crucial for achieving stationary NBI-heated I-mode plasmas in AUG, as has already been shown in [111]. Later in the discharge, the request value of β_{pol} is increased in a stepwise manner; both β_{pol} and the pedestal top electron temperature rise accordingly, while the electron density stays constant.
At $t = 4.3\,\mathrm{s}$ the transition to H-mode takes place, which can be seen from the simultaneous rise of both the pedestal top electron temperature and the line-averaged density. Also, the WCM disappears from the spectrogram when the H-mode begins. In AUG, I-mode PREs appear before the I-H transition, in this case when $\beta_{\mathrm{pol}} \approx 0.58 - 0.61$. This can be seen in the radiation measured with an AXUV diode bolometer [143] having a line of sight in the upper divertor region (panel (f)). The radiation is characterized by several spikes in this phase and the heat flux onto the upper outer divertor inferred from infrared cameras exhibits transient rises (panel (g)).
When I-mode PREs appear, low frequency fluctuations ($< 50\,\mathrm{kHz}$) with larger amplitudes than in a typical I-mode without PREs (see e.g. #36233 at 2.5 s) are present in the spectrogram. A clearer view of edge plasma parameters during I-mode PREs is shown in the magnification in the bottom right panel of Fig. 6.1. The pedestal top electron temperature drops during these events (panel (h)). The plasma expelled from the confined region enters the SOL and reaches the divertor, causing a strong increase in the radiation signal (panel (i)). Ultimately, it hits the divertor target, leading to a substantial increase in the divertor heat fluxes (panel (j)). For comparison, a magnification of the same time traces of an I-mode without PREs is shown in the bottom

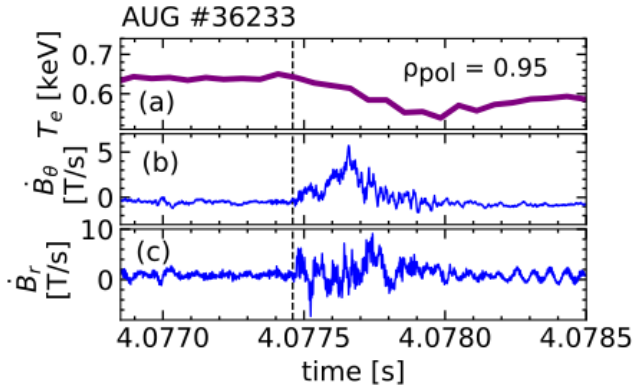

Figure 6.2: Time evolution of the pedestal top electron temperature (a), the $\dot{B}_\theta$ (b) and $\dot{B}_r$ (c) signal measured by magnetic pick-up coils during an I-mode PRE. No magnetic precursors are detected before the onset of a PRE.

left panel of Fig. 6.1. The pedestal top electron temperature is rather constant and does not exhibit a large drop. This is reflected in the divertor radiation and heat flux values that do not change substantially.
Figure 6.2 shows the temporal derivative of the poloidal and radial component of the magnetic field measured by magnetic pick-up coils during an I-mode PRE. After the PRE onset (indicated by a vertical dashed line), both the poloidal and radial component of the magnetic field are perturbed. Moreover, no precursor oscillations are detected by magnetic pick-up coils before the onset of PREs, marking a difference with type-I, type-II and type-III ELMs, which are characterized by detectable magnetic precursors [25, 66, 167].

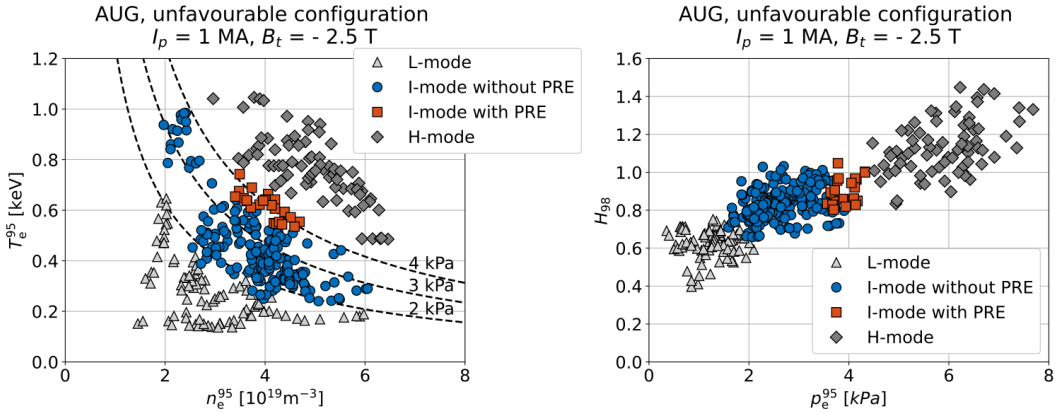

Figure 6.3: Left: Electron temperature vs. electron density (both evaluated at $\rho_{\mathrm{pol}} = 0.95$) of AUG L-mode, I-mode and H-mode discharges at $I_p = 1\,\mathrm{MA}$ and $B_t = -2.5\,\mathrm{T}$. For $n_e^{95} \approx 4 \times 10^{19}\,\mathrm{m}^{-3}$, I-mode PREs appear just before the I-H transition. Dashed lines indicate isobars. Right: confinement factor H_{98} against electron pressure at $\rho_{\mathrm{pol}} = 0.95$. I-mode discharges with and without PREs can reach $H_{98} = 1$.

Figure 6.3 (a) shows the AUG I-mode discharges obtained at $I_p = 1\,\mathrm{MA}$ and $B_t = -2.5\,\mathrm{T}$ in the T_e-n_e operational space. Also L-mode and H-mode discharges obtained at the same plasma current and toroidal magnetic field are plotted. Electron temperature and density at $\rho_{\mathrm{pol}} = 0.95$ have been obtained through integrated data analysis, see section 4.4.7.
I-mode with PREs appear only in a small portion of the T_e-n_e diagram, namely around the isobar at 4 kPa for $3 \times 10^{19} < n_e^{95} < 5 \times 10^{19}\,\mathrm{m}^{-3}$. This isobar lies very close to the I-H transition. Figure 6.3 (b) shows the same database plotted in the H_{98}-p_e^{95} space, where p_e^{95} is the electron pressure at $\rho_{\mathrm{pol}} = 0.95$. When I-mode PREs appear, no substantial enhancement of H_{98} is observed with increasing p_e^{95}, i.e. I-mode discharges with and without PREs can reach high confinement with $H_{98} \simeq 0.8$–1.0. This indicates that in AUG stationary and high-confinement I-mode plasmas without PREs can be regularly achieved. At this stage, it is not clear whether PREs are present in I-mode at higher densities. For $n_e^{95} \approx 2.4 \times 10^{19}\,\mathrm{m}^{-3}$, which is close to the lowest density at which I-mode is achieved, I-mode PREs have not been found at 1 MA and 2.5 T.

6.1.2 Appearance in hydrogen I-mode plasmas

I-mode plasmas are also achieved by using hydrogen as the main species in ASDEX Upgrade. Figure 6.4 shows a typical I-mode discharge in upper single null configuration using hydrogen. The discharge parameters are $I_p = 1\,\mathrm{MA}$, $B_\mathrm{t} = -2.5\,\mathrm{T}$ and a line-averaged core electron density of about $6 \times 10^{19}\mathrm{m}^{-3}$ (see panel (e)). The plasma is heated with 2.2 MW of ECRH power and modulated co-current NBI power which is increasing linearly, as shown in panel (a) of Fig. 6.4. Around $t = 2.95\,\mathrm{s}$, when the total heating power is $P_\mathrm{heat} = 5\,\mathrm{MW}$, the transition to I-mode occurs. This is seen from the appearance of the WCM in the spectrogram of the reflectometry signal detected at $\rho_\mathrm{pol} \simeq 0.98$ (panel (d)), which is a measure of electron density fluctuations. Simultaneously H_{98} slightly increases. The line-averaged density stays constant, while the electron temperature at $\rho_\mathrm{pol} = 0.95$ T_e^{95} rises due to a combination of the slightly improved energy confinement and additional heating power. At $t = 4.07\,\mathrm{s}$ the plasma

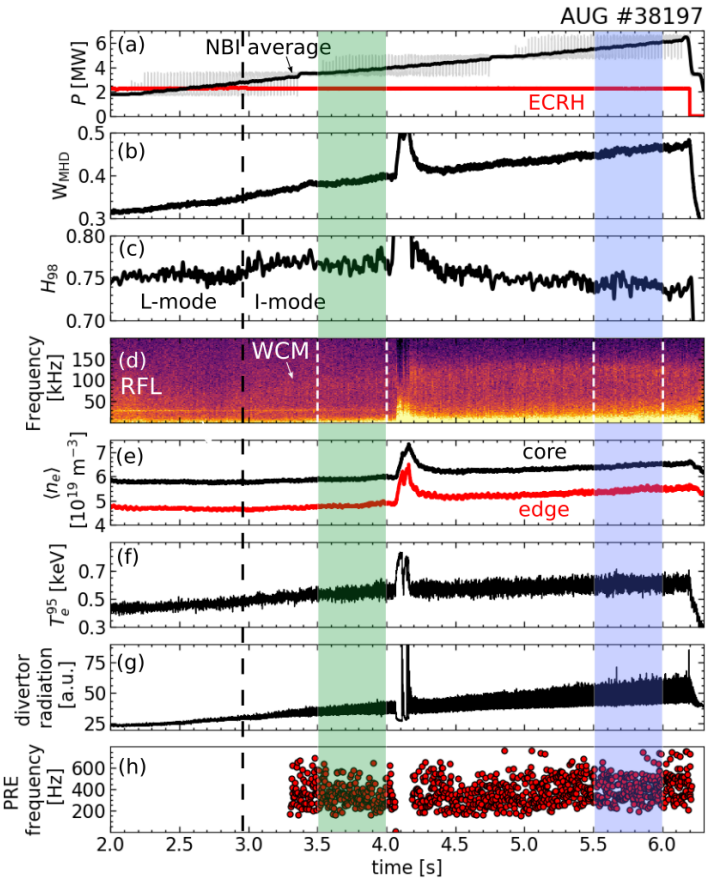

Figure 6.4: I-mode hydrogen USN discharge. (a) ECRH (red) and NBI (black) power. (b) Plasma stored energy W_MHD. (c) H_{98}. (d) O-mode reflectometry homodyne signal spectrogram caused by density fluctuations at about $\rho_\mathrm{pol} \simeq 0.98$. (e) Line-averaged core (black) and edge (red) electron density. (f) Electron temperature at $\rho_\mathrm{pol} = 0.95$ measured by ECE radiometers. (g) Radiation measured by a diode bolometer with line of sight in the upper divertor region. (h) Frequency of occurrence of I-mode PREs.

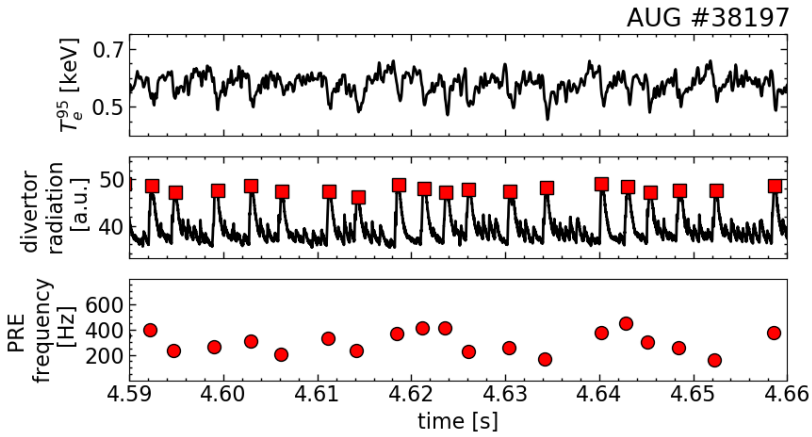

Figure 6.5: Magnification of electron temperature at $\rho_{\mathrm{pol}} = 0.95$, divertor radiation and PRE frequency of occurrence during #38197. The maxima of the divertor radiation signal (red squares) are used to detect the PRE time of occurrence and to compute the corresponding frequency.

transiently enters H-mode. After about 100 ms the plasma returns to I-mode conditions and it stays in this confinement regime until the end of the discharge (when $P_{\mathrm{heat}} = 8.3\,\mathrm{MW}$). Throughout the entire I-mode phase PREs are present. They are identified by the divertor radiation signal measured by a diode bolometer looking at the upper divertor region (panel (g)). Their frequency of occurrence is displayed in panel (h) and it ranges between 200 Hz and 600 Hz.

A magnification of the edge electron temperature, the divertor radiation signal and the corresponding PRE frequency is shown in Fig. 6.5. Each PRE can be detected from the drop of the edge electron temperature measured by ECE radiometers and by the corresponding rise of the divertor radiation measured by diode bolometers. The maxima of the divertor radiation signal (red squares) are used to detect the PRE's time of occurrence. In this way, the temporal separation Δt_{PRE} between two PREs is calculated as well as the frequency of occurrence $f_{\mathrm{PRE}} = 1/\Delta t_{\mathrm{PRE}}$. Note that the small events appearing sometimes between two PREs are not considered in the frequency calculation.

In hydrogen I-mode plasmas, PREs occur in a broader power window than in deuterium plasmas. For instance, in the deuterium discharge shown in section 6.1.1, PREs occurred in the power range $P_{\mathrm{heat}} = 3.4 - 3.8\,\mathrm{MW}$, while in the hydrogen discharge shown here PREs appear in the power range $P_{\mathrm{heat}} = 5.0 - 8.3\,\mathrm{MW}$. Such enlarged power window of existence allows us to study the PRE frequency change with heating power and to compare it to the corresponding behaviour of ELMs, as listed in section 2.2.1. Figure 6.6 shows the histogram of the PRE frequency in two time windows during discharge #38197: for $t = 3.5 - 4.0\,\mathrm{s}$ when $P_{\mathrm{heat}} = 5.9\,\mathrm{MW}$ and $T_e^{95} = 0.55\,\mathrm{keV}$, and for $t = 5.5 - 6.0\,\mathrm{s}$ when $P_{\mathrm{heat}} = 8.0\,\mathrm{MW}$ and $T_e^{95} = 0.61\,\mathrm{keV}$. The two time windows are also highlighted in green and blue in Fig. 6.4. Going from low to high heat-

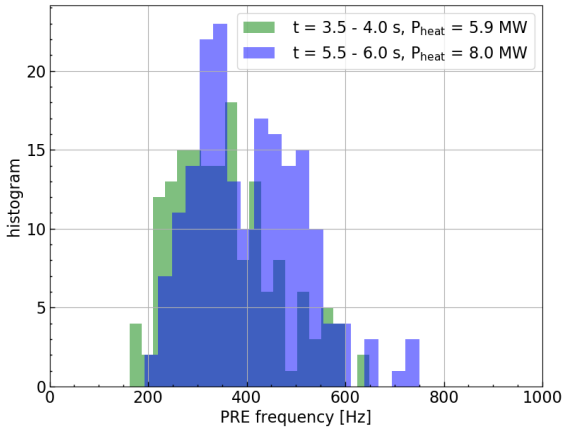

Figure 6.6: Histograms of the PRE frequency of occurrence in two time windows during discharge #38197; at low heating power (green) and at high heating power (blue). The two time windows are highlighted in Fig. 6.4.

ing power, the PRE frequency distribution covers the same frequency range, i.e. from about 200 Hz to 600 Hz. However, at high power the PRE frequency distribution is broadened towards higher frequencies. This marks a difference to type-III ELMs, which are characterized by a frequency of occurrence that decreases with increasing heating power or, equivalently, with increasing edge electron temperature [25].

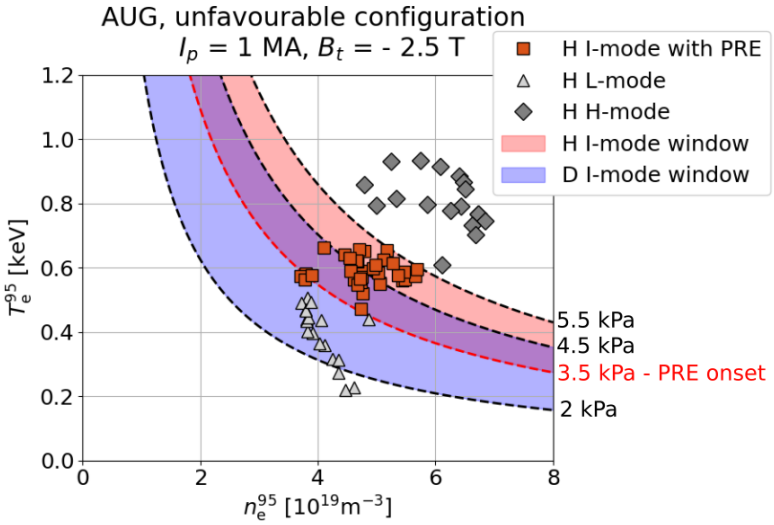

Figure 6.7: Electron temperature vs. electron density (both evaluated at $\rho_{\mathrm{pol}} = 0.95$) of hydrogen AUG L-mode, I-mode and H-mode discharges at $I_p = 1\,\mathrm{MA}$ and $B_t = -2.5\,\mathrm{T}$ in unfavorable configuration. The I-mode window of existence in deuterium (hydrogen) is displayed in light blue (red). Dashed lines represent isobars. The I-mode window of existence in hydrogen is above the pressure threshold for the occurrence of PREs (red dashed line).

Figure 6.7 shows hydrogen L-mode, I-mode and H-mode discharges in unfavorable configuration obtained at $I_p = 1\,\mathrm{MA}$ and $B_t = -2.5\,\mathrm{T}$ in the T_e-n_e operational space. Several isobars are displayed as dashed lines. The window of existence of deuterium I-mode plasmas (see Fig. 6.3) is plotted in blue, while the hydrogen I-mode window is highlighted in red. In hydrogen, the I-mode exists at higher edge electron pressures than in deuterium. Hydrogen I-mode plasmas exist for $3.5 < p_e^{95} < 5.5\,\mathrm{kPa}$, whereas deuterium I-mode plasmas appear for $2.0 < p_e^{95} < 4.5\,\mathrm{kPa}$. Consistently, L-mode hydrogen plasmas can reach higher edge electron pressure than deuterium ones. I-mode hydrogen plasmas appear for $p_e^{95} > 3.5\,\mathrm{kPa}$, which is the threshold value for the appearance of PREs in deuterium (see Fig. 6.3). Interestingly all hydrogen I-mode plasmas obtained so far in AUG exhibit PREs.

6.2 Edge parameter profiles

In this section, the plasma parameter profiles in the edge of deuterium I-mode discharges are analyzed and their dynamics during PREs is shown. Later, the energy and particle losses associated to the relaxation of the pedestal are studied. Last, the magnetohydrodynamic (MHD) stability of the I-mode pedestal during PREs is investigated and is compared to that of type-I ELMs.

6.2.1 Temporal evolution

Thanks to the β_{pol} feedback control by means of the NBI power as actuator, stationary deuterium I-mode discharges with several PREs have been obtained. Figure 6.8 shows the time trace of different quantities during such an I-mode discharge (in USN plasma $I_p = 1\,\mathrm{MA}$ and $B_{\mathrm{t}} = -2.5\,\mathrm{T}$, see e.g. [104]). The heating power (panel (a)) is a mixture of constant ECRH power and modulated NBI power, with the latter feedback controlled on the requested value of $\beta_{\mathrm{pol}} = 0.61$, (panel (b)). Both the core and edge line-averaged electron density (panel (c)) are constant in this phase. The WCM is present during the entire I-mode at a frequency of 75 kHz, as can be seen in the spectrogram of the reflectometry signal detected at $\rho_{\mathrm{pol}} \simeq 0.98$ (panel (d)). The divertor radiation is used as a PRE monitor, as it shows a clear peak during each PRE event (panel (e)). The frequency of occurrence of I-mode PREs ranges between 100 and 400 Hz (panel (f)) in this discharge.
The constant plasma parameters and PRE behavior found in this I-mode discharge allowed us to obtain the conditionally averaged temporal evolution of edge electron temperature and density profiles during PREs. Fast measurements of electron density were obtained from DCN interferometry and lithium beam emission spectroscopy (Li-BES), while the electron temperature was measured with ECE radiometers. These diagnostics measurements were combined through the integrated data analysis (IDA) described in section 4.4.7, providing electron temperature and density profiles with a time reso-

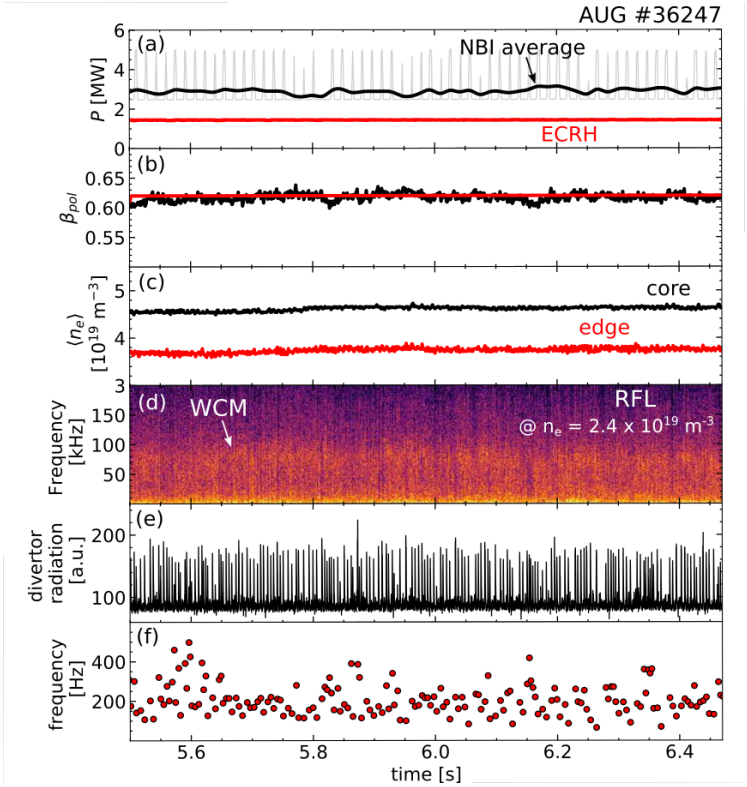

Figure 6.8: Stationary I-mode discharge with PREs. (a) ECRH (red) and NBI (gray) heating power. The solid black line is the averaged NBI power. (b) Requested β_{pol} (red) and measured value (black). (c) Line-averaged core (black) and edge (red) electron densities. (d) O-mode reflectometry homodyne signal spectrogram caused by density fluctuations at $n_{\mathrm{e}} = 2.4 \times 10^{19}\,\mathrm{m}^{-3}$, i.e. $\rho_{\mathrm{pol}} \simeq 0.98$. (e) Radiation in the upper divertor region. (f) Frequency of PREs.

lution of 0.1 ms. The reconstructed IDA temperature profiles have a separatrix temperature around 60–80 eV, which is the typical I-mode value measured at AUG by the edge Thomson scattering system. Similar separatrix temperatures follow also from Eq. 2.17. Li-BES data were corrected by subtracting the enhanced passive radiation observed during the PRE phase, with the same method as used in [168] to analyze the type-I ELM cycle. For details refer to [168]. Hereinafter, the time synchronization of each PRE was obtained using a diode bolometer channel with the line of sight in the upper divertor, as it has been found to be the best PRE monitor signal in USN plasma discharges. Then, different plasma quantities were conditionally averaged using the above-mentioned time synchronization in the time window between $t_{\mathrm{start}} = 5.5\,\mathrm{s}$ and $t_{\mathrm{end}} = 6.47\,\mathrm{s}$. Only PREs occurring when the Li-BES diagnostics was switched on are considered, giving a total number of 105 events.
Figure 6.9 shows the time evolution of conditionally averaged electron temperature, density and pressure evaluated around the temperature pedestal top position, i.e. $\rho_{\mathrm{pol}} = 0.94$. Error bars represent the 50 % confidence interval of the 105 events analyzed. All quantities are normalized to their values at the

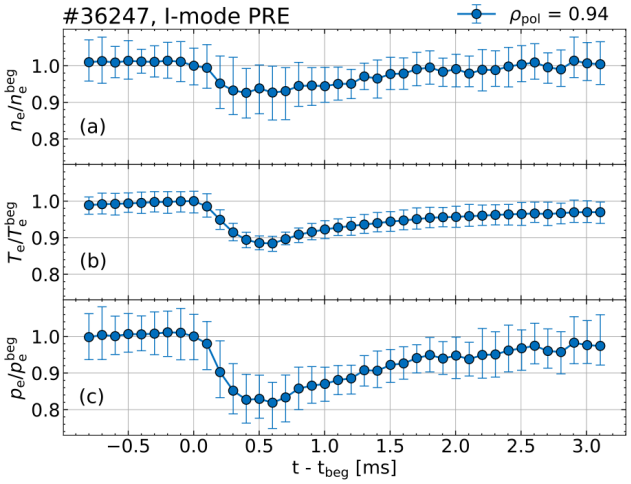

Figure 6.9: Temporal evolution of conditionally averaged electron density (a) temperature (b) and pressure (c) at $\rho_{pol} = 0.94$ (i.e. around the electron temperature pedestal top position). Each quantity is normalized to its value at the PRE onset.

PRE onset. The relative drop of the electron density is about 7 %, whereas the electron temperature reduces by 12 %. As a consequence, the electron pressure decreases by about 18 % during the PRE. The relative drop of the pedestal top electron temperature and density during I-mode PREs in #36247 is lower than the corresponding reduction during type-I ELMs, which ranges between 20 and 50 % (for the electron temperature) and between 10 and 40 % (for the electron density) across different devices [168–171]. It is also worth noting that the electron temperature and density exhibit different recovery times: 2.5 ms after the PRE onset, the electron density is back to its value before the PRE, while the electron temperature has not recovered yet. The different recovery times are also a typical feature of the type-I ELM cycle, as reported in [168,170,172].

Figure 6.10 shows a comparison of the electron density (panel (a)), temperature (panel (b)) and pressure (panel (c)) radial profiles before and 0.6 ms after the PRE onset. The envelopes around each profile represent the 50 % confidence interval. The error envelopes of the electron density profiles are larger at the pedestal top because at that position the lithium beam signal is weaker. After 0.6 ms the electron density profile shows a decrease in the edge density gradient, with the density for $\rho_{pol} < 0.98$ reducing and the SOL density increasing. This results in the formation of a pivot point around $\rho_{pol} = 0.99$. The electron density at the pivot point is approximately equal to half of the density at $\rho_{pol} = 0.95$. Both the aforementioned features are similar to what happens during type-I ELMs in AUG [173]. The reconstructed IDA electron temperature radial profile during PREs suffers from the so-called ECE "shine-through" effect at the plasma edge [131], which makes the evaluation of electron temperature edge gradients around the separatrix impossible in this particular case. For this reason the pivot point of the electron temperature profiles cannot be eval-

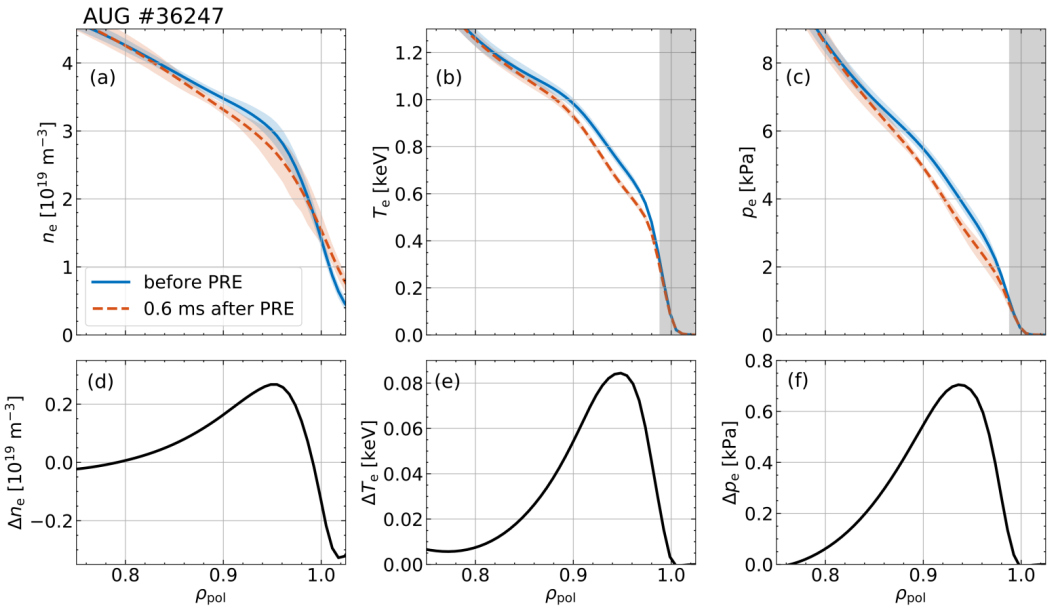

Figure 6.10: Top: Conditionally averaged radial profiles of electron density (a), temperature (b) and pressure (c) before and 0.6 ms after I-mode PREs. The shaded gray area indicates the ECE "shine-through" region. Bottom: difference between the before PRE and after PRE radial profiles of the electron density (d), temperature (e) and pressure (f).

uated. Nonetheless, outside the "shine-through" region (shaded gray area in Fig 6.10 (b)), ECE data are reliable, as they display very good agreement with TS data. In this region ($\rho_{\mathrm{pol}} < 0.98$), the electron temperature shows a clear reduction after the PRE onset, as it is observed for the density. Additionally, the bottom panels of Fig. 6.10 show the radial profiles of the electron density (panel (d)), temperature (panel (e)) and pressure (panel (f)) collapses, defined as the profile difference before and after the PRE. They all show a maximum around $\rho_{\mathrm{pol}} = 0.95$, i.e. around the I-mode electron temperature pedestal top position.

From Fig. 6.10 the PRE profile affected depth can be evaluated, i.e. the distance between the pivot point and the inner radial point where no substantial difference between before and after PRE profile is detected. The PRE affected depth is about 0.2 in terms of normalized poloidal flux radius and 10 cm in terms of radial distance, similar to the ELM affected depth in AUG [174], JET [175], D-IIID [72] and JT-60U [176].

6.2.2 Energy and particle losses

Knowing the radial profiles' temporal evolution, the I-mode PRE energy and particle losses can be calculated, as can the convective and conductive components of the energy loss. Definitions introduced in section 2.2.2 are used here. The PRE particle loss is calculated directly from the measured Δn_e shown in Fig. 6.10 (d). In the analyzed discharge, the PRE particle loss is 8.6×10^{18} m^{-3},

which is about 2 % of the pedestal particle content N_{ped}. This percentage is close to the lower range of observed values for $\Delta N/N_{\mathrm{ped}}$ during ELMs, which varies between 2 % and 13 % in AUG [174] and JET [70].
To calculate the energy losses, the ion contribution also needs to be considered. As no fast measurements of T_i and n_i were available to temporally resolve PREs, assumptions need to be introduced. In this low-impurity content discharge, $n_i = n_e$ is assumed. Also, since in I-mode discharges at AUG the pedestal top ion and electron temperature are very close [104], $T_i = T_e$ is considered. Moreover, it is also conjectured that $\Delta n_e = \Delta n_i$ and $\Delta T_e = \Delta T_i$. While the first equality has been proven to hold at different collisionalities for type-I ELMs, the second one can be broken at low collisionalities, with $\Delta T_i < \Delta T_e$ [171]. Therefore, the following energy losses should be regarded as an upper limit.
Considering the above-mentioned assumptions, the conductive and convective energy losses during I-mode PRE are 4.2 kJ (3.3 % of W_{ped}) and 3.2 kJ (2.5 % of W_{ped}), respectively. For the same pedestal collisionality, ELM conductive and convective relative losses range between $6-11$ % and $6-18$ % [72], respectively, and are thus larger than the I-mode PREs losses.

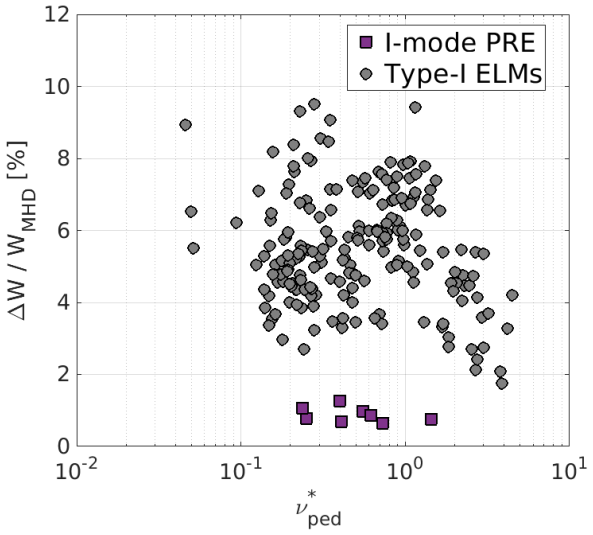

Figure 6.11: Relative energy loss against pedestal collisionality for type-I ELMs and I-mode PREs. I-mode PREs exhibit relative energy losses lower than those of type-I ELMs.

The PRE energy loss obtained from Eq. 2.26 is 7.2 kJ, which is 1.8 % of the total energy W_{MHD} and 5.7 % of the pedestal energy content W_{ped}. This quantity is compared to the energy loss calculated from the conditionally averaged W_{MHD} signal, which yields $\Delta W_{\mathrm{MHD}}/W_{\mathrm{MHD}} \approx 1.1$ % and $\Delta W_{\mathrm{MHD}}/W_{\mathrm{ped}} \approx 3.3$ %. This discrepancy may be explained by the assumptions made on the ion contribution, which leads to an overestimation of the relative energy loss.
Figure 6.11 shows the relative energy loss of I-mode PREs and type-I ELMs against the pedestal collisionality. I-mode PRE energy losses are calculated

from conditionally averaged W_{MHD} signals. I-mode PRE relative energy losses are on average around 1 %. Type-I ELM data used for the multimachine study in [26] are reexamined here. For the same pedestal collisionality, type-I ELM relative energy losses range between $3-10\,\%$, and are thus larger than those of I-mode PREs.

6.2.3 MHD stability

Figure 6.12 shows the peeling-ballooning pedestal stability diagram calculated with the MISHKA code [177] for an AUG discharge with I-mode PREs that later enters the H-mode. The MHD stability is parameterized here in terms of the maximum normalized edge pressure gradient α_{max} [178] and flux-surface averaged edge current density $\langle j_{\mathrm{tor}} \rangle$. The lines show the stability boundary defined with the criterion used in [179] for both I-mode and H-mode. Above the stability boundary, peeling-ballooning modes are unstable and type-I ELMs occur. The H-mode pedestal is close to the stability boundary and this agrees with the observation of type-I ELMs in the analyzed discharge. On the contrary, the I-mode pedestal with PREs is far from the ideal peeling-ballooning stability boundary, which is usually the case in I-mode [104, 112]. This shows clearly that I-mode PREs are not type-I ELMs.

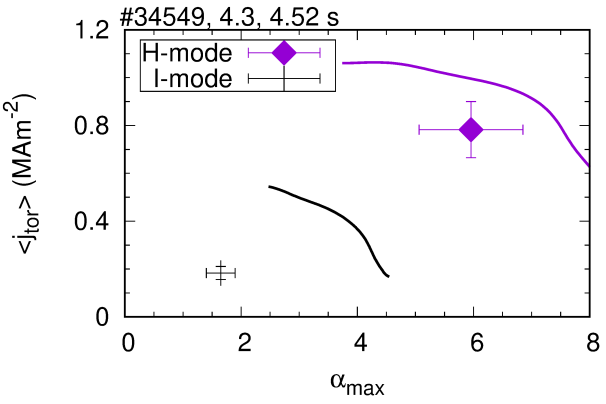

Figure 6.12: Ideal peeling-ballooning stability diagram of the I-mode pedestal with PREs (black cross) and the H-mode pedestal with type-I ELMs (purple diamond) in #34549. The black and purple lines represent the stability boundary in I-mode and H-mode, respectively. The I-mode pedestal with PREs is ideal peeling-ballooning stable.

6.3 Transport in the scrape-off layer

In this section, it is investigated how perturbations of plasma parameters caused by PREs are transported in the SOL. To begin, the temporal evolution of SOL and divertor plasma quantities is analyzed. Later, SOL filamentary

transport is studied as well as the toroidal structure of PRE induced perturbations.

6.3.1 SOL radiation, electron temperature and density temporal evolution

The energy lost during PREs from the confined region enters the SOL and is transported both along and across the open magnetic field lines, i.e. both in the parallel and perpendicular directions. This sets the characteristic temporal evolution of different SOL plasma quantities and of the energy reaching the divertor targets. Figure 6.13 shows the conditionally averaged temporal evolutions of the outer midplane SOL electron density and temperature (top panel) and of the divertor radiation (bottom panel) during I-mode PREs. The conditional average was carried out over the same 105 PREs analyzed in section 6.2.1. In Fig. 6.13 three time instants are marked: the PRE beginning time t_{beg} (green), the PRE ending time t_{end} (gray) and the time instant of the maximum value t_{max} (magenta). They are defined in section 2.2.5 along with the decay time τ_{decay} and rise time τ_{rise}. The SOL electron density and temperature have been measured by the helium beam system [140] installed at AUG with a time resolution of 17 µs. The radiation is measured in the upper divertor region by a diode bolometer with a time resolution of 2.5 µs. This

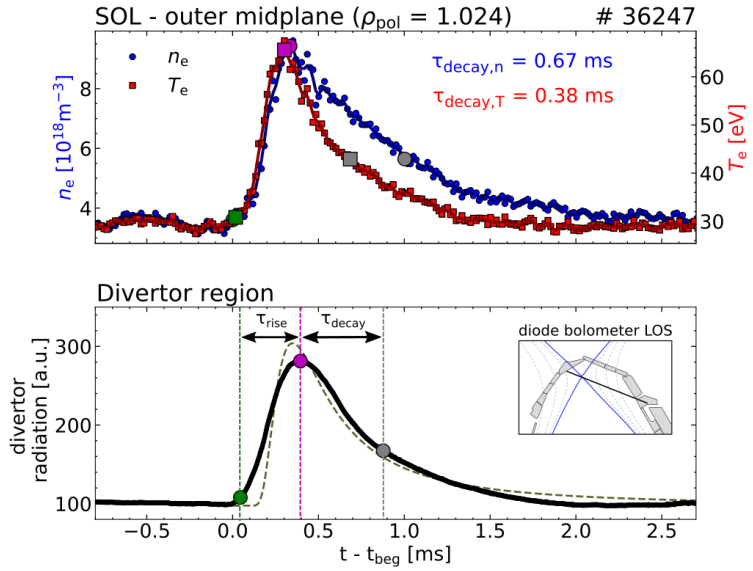

Figure 6.13: Top: Conditionally averaged temporal evolution of electron temperature (red) and density (blue) at the outer midplane in the SOL ($\rho_{\mathrm{pol}} = 1.024$) measured by the helium beam diagnostics during I-mode PREs. Bottom: Conditionally averaged divertor radiation during I-mode PREs measured by a diode bolometer. The line of sight (LOS) of the diode bolometer is depicted in the upper right corner. The dashed line is the fit of the data using Eq. 2.41. Green and gray markers represent the beginning and ending time of the PRE, respectively.

highly temporally resolved signal is used as a proxy for the energy deposited onto the divertor target plates. IR cameras provide a direct measurement of the energy deposited onto the divertor targets, however, their time resolution (about 0.6 ms) is not high enough to resolve the temporal shape. The drawback of using the radiation measurements is that the line of sight of the diode bolometer (which is depicted in the bottom panel of Fig. 6.13) crosses both the outer and inner divertor regions. Therefore, the data shown here should be considered as an "integral" of both inner and outer divertor radiation.
The top panel of Fig. 6.13 shows that electron temperature and density exhibit a different temporal behavior. While their rise time is almost equal ($\tau_{\mathrm{rise},n/T} \approx 0.3\,\mathrm{ms}$), their decay time differs substantially ($\tau_{\mathrm{decay},T} = 0.38\,\mathrm{ms}$ and $\tau_{\mathrm{decay},n} = 0.67\,\mathrm{ms}$). This may be due to the fact that conductive transport takes place on a faster timescale than the convective one, thus giving rise to a faster temperature decay than that of the density, as also predicted by the "free-streaming-particle" model introduced in section 2.2.5. The bottom panel of Fig. 6.13 shows that the divertor radiation exhibits a temporal evolution as it is typical for the power deposition onto the divertor targets during type-I ELMs [87]: After an initial sharp rise, a slow exponential decay is present.
In Fig. 6.13, the "free-streaming-particle" model is used to fit the radiation data ($\propto \mathrm{kW/m^2}$) with Eq. 2.41. The model describes the temporal evolution of the divertor radiation during I-mode PREs. Hence, the temporal evolution of the power deposition caused by PREs does not substantially differ from that of type-I ELMs. This points to the universality of energy transport in the SOL during any pedestal relaxation event. In addition, Fig. 6.13 shows that the average PRE deposition time (defined as $\tau_{\mathrm{dep}} = \tau_{\mathrm{rise}} + \tau_{\mathrm{decay}}$) is about 0.8 ms. This marks a difference with respect to the previously analyzed I-mode density "bursts" in AUG, which showed turbulence timescales of the order of µs both in the confined region and in the SOL [104, 110]. These longer "type-I-ELM-like"

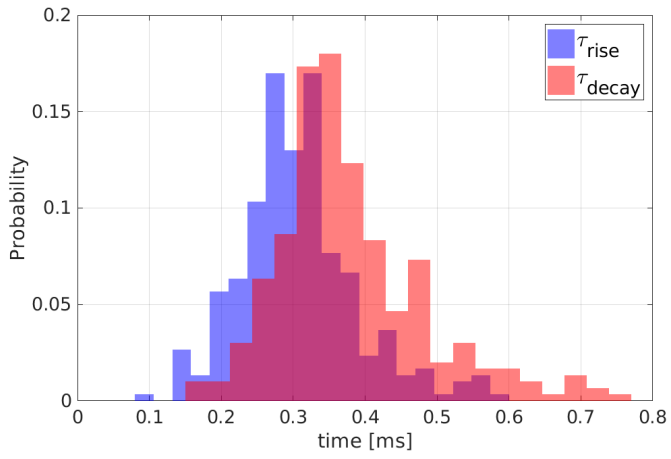

Figure 6.14: Probability distribution of rise time (blue) and decay time (red) of the divertor radiation signal measured by a diode bolometer during PREs.

timescales reduce the divertor transient thermal load when compared to the shorter turbulence timescales, as they cause a smaller surface temperature rise for the same deposited energy fluence (see Eq. 2.33).
Figure 6.14 shows the statistical distribution of the rise time (blue histograms) and decay time (red histograms) of the divertor radiation signal measured by a diode bolometer for about 300 PREs. While the rise time distribution peaks around 0.3 ms, the decay time distribution reaches its maximum value around 0.35 ms. Also, the τ_{decay} distribution is shifted to longer duration times than the τ_{rise} distribution. Both findings indicate that $\tau_{\mathrm{decay}} > \tau_{\mathrm{rise}}$. Also, from this statistical analysis it results that the average deposition time $\langle \tau_{\mathrm{dep}} \rangle$ is about 0.7 ms, which is similar to the conditionally-averaged deposition time obtained in #36247.

6.3.2 Filament propagation and precursor

During I-mode PREs, plasma filaments are generated in the plasma edge and travel through the SOL until reaching the divertor target plates, as is the case for type-I ELMs. The formation and propagation of several filaments during an I-mode PRE are shown in Fig. 6.15 (a). The time evolution of the He 587.6 nm line intensity measured at different normalized radial position ρ_{pol} at the outer midplane by the thermal helium beam system is depicted. The line intensity of each channel is normalized to its maximum value. After the onset of the PRE ($t > 5.7456$ s), plasma filaments are expelled into the SOL and propagate both in the radial and toroidal direction. Viewed from a fixed location, the combined effect of toroidal and radial propagation results in a succession of structures moving radially outwards over time. From each detected filament a radial velocity can be calculated. By analyzing an ensemble of filaments, a probability distribution function of the radial velocity that peaks around 0.5 km/s is found. This velocity is also similar to the typical filament radial velocities measured during type-I ELMs ($0.5 - 1$ km/s) [180–182], while it is larger than the typical filament velocity measured in L-mode, in the inter-ELM H-mode phase and during the I-phase bursts ($0.2 - 0.3$ km/s) [183–185]. Plasma filaments are generated throughout the entire duration of the PRE (of about 0.7 ms) until the pedestal recovers.
Figure 6.15 (a) shows also, a precursor oscillation before the PRE onset, which is localized in the confined region of the plasma. This precursor can be seen more clearly in Fig 6.15 (b), where the time evolution of the He 587.6 nm line intensity measured at $\rho_{\mathrm{pol}} = 0.988$ is depicted. The spectrogram of this He line (shown in panel (c)) illustrates that the precursor oscillates around $f_{\mathrm{prec}} = 75$ kHz, which is the frequency of the weakly coherent mode (WCM) in discharge #36247 that is shown in Fig. 6.8 (d). However, it should be mentioned that these precursors in the He 587.6 nm line intensity are not always observed before the PRE onset. Also, no precursors in the $\dot{B}_{\mathrm{r}}$ and $\dot{B}_{\theta}$ signals measured by magnetic pick-up coils were identified before the onset of I-mode

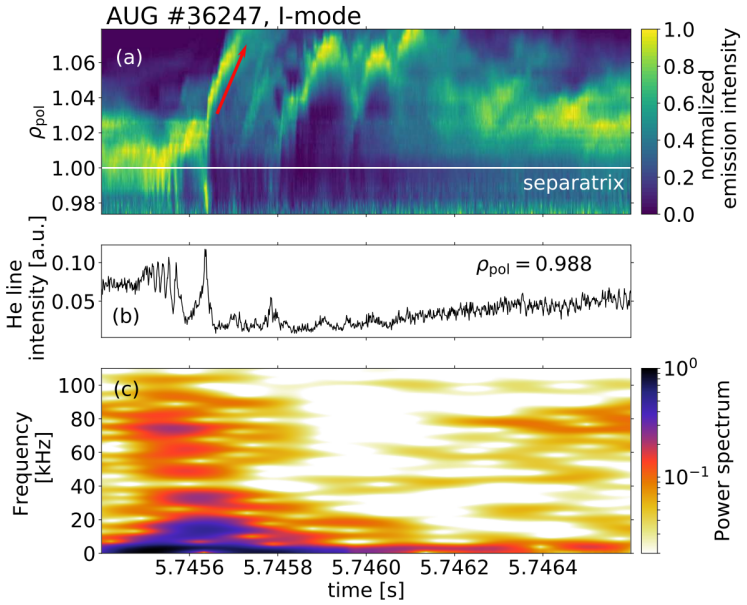

Figure 6.15: (a) Helium 587.6 nm line intensity measured at different ρ_{pol} at the outer midplane by the thermal helium beam system during an I-mode PRE. The line intensity at each value of ρ_{pol} has been normalized to its maximum value. Plasma filaments are generated and propagate in the SOL during I-mode PREs. (b) Helium 587.6 nm line intensity at $\rho_{pol} = 0.988$ and (c) its spectrogram. A precursor oscillation at the WCM frequency and localized in the confined region is observed before the onset of this PRE.

PREs (see Fig. 6.1 (m)). The visibility of a precursor in a local edge diagnostic and the absence of a detectable magnetic precursor from the pick-up coils appears also during oscillations present in the early I-phase [99].

6.3.3 Quasi mode number

The filaments observed at the outer midplane ultimately reach the divertor target and are measured via the IR camera system installed at AUG. Figure 6.16 (a) shows an example of the heat flux profile measured on the upper divertor during an I-mode PRE. The peak heat flux is usually observed around the strike point location (s_0). However, several additional peaks are measured in the far SOL. These substructures are the result of plasma filaments that are generated at the midplane at different torodial locations and that propagate in the SOL in the parallel B-field direction until they hit the divertor targets. The same phenomenon has been observed during type-I ELMs in several devices, as described in section 2.2.3.
Magnetic field line mapping from the outer midplane to the divertor target can be used to identify the toroidal displacement of the filaments generated upstream. The procedure is the following: First, the location of the peaks in the far-SOL region is detected as shown in Fig. 6.16 (a). Then, magnetic field lines at different radial positions (from the separatrix to the far-SOL) at the outer midplane and at the same torodial position are mapped to the upper di-

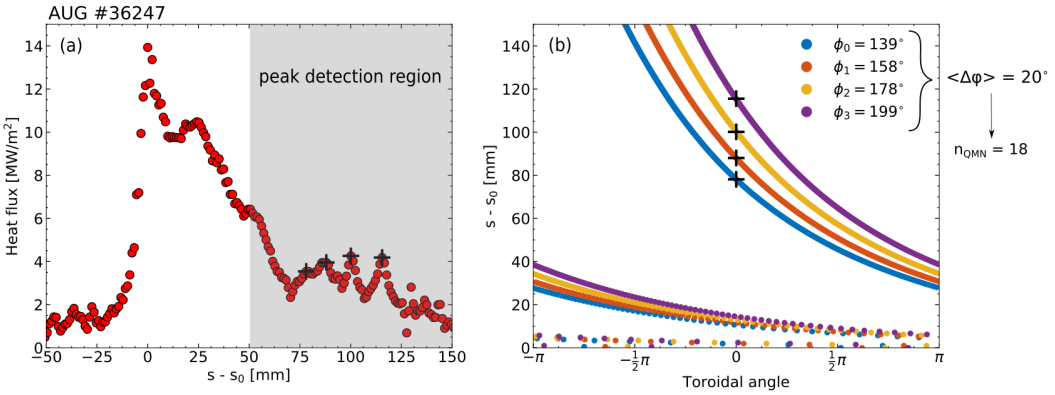

Figure 6.16: (a) Detected peaks (black crosses) of a heat flux profile during a PRE from IR measurements. The gray region indicates the far-SOL region where the peak detection is carried out. (b) Intersecting structures of the field lines originating in the outer midplane (at different toroidal angles ϕ) on the upper outer divertor targets. The toroidal angle of the IR tile is set to zero, as a reference. The starting torodial angle of the field lines at the outer midplane is chosen to intersect the location of each peak measured on the outer divertor target.

vertor target. We will refer to such cluster of magnetic field lines as magnetic flux bundle. The connection length of the field lines depend on the radial position and becomes much longer when approaching the separatrix. Therefore, magnetic field lines that started near the separatrix will have a larger toroidal displacement than those from the far-SOL. As a consequence, the intersecting structure of the magnetic flux bundle with the divertor target becomes more displaced in the toroidal direction when approaching the separatrix, resulting in a spiral geometry.

Figure 6.16 (b) shows the intersection of the field lines with the upper outer divertor tiles at different torodial angles. The toroidal angle of the IR divertor tile is set to zero. Each coloured line represents the field-line tracing originating from a different toroidal angle at the outer midplane. The starting torodial angle of the field lines at the outer midplane is chosen to intersect the position of each peak measured on the outer divertor target. In the case shown in Fig. 6.16 (b), the toroidal angles of the field lines at the outer midplane that are intersecting the peaks are $\phi_0 = 139°$, $\phi_1 = 158°$, $\phi_2 = 178°$, $\phi_3 = 199°$. Once we have identified a subset of several toroidally displaced origins of energy release in the midplane, the "quasi mode number" defined in section 2.2.3 is calculated. In the example shown in Fig. 6.16 (b), $n_{\mathrm{QMN}} = 18$ is obtained. It should be noted that the peak detection is carried out only in the far SOL, i.e. for $s - s_0 > 50\,\mathrm{mm}$ (which corresponds to $r - r_{\mathrm{sep}} > 7\,\mathrm{mm}$ at the outer midplane). This is because, for $s - s_0 < 50\,\mathrm{mm}$, toroidally displaced energy effluxes from the midplane are not sufficiently spaced out at the divertor target, as can be seen from Fig. 6.16 (b), making it difficult to identify a univocal correspondence between the peaks measured at the divertor and the toroidal location at the midplane.

For the I-mode PREs analyzed in discharge #36247, the quasi mode number ranges between 10 and 28, and has a mean value of $\langle n_{\mathrm{QMN}} \rangle = 20$. Interestingly, magnetic probes in the Alcator C-Mod tokamak showed that the WCM has a toroidal mode number between 15 and 25 [109]. For comparison, the quasi mode number during type-I ELMs ranges between 5 and 20 [74, 75, 79].

6.4 Divertor transient heat loads

In this section, PREs divertor heat loads are investigated. First of all, divertor in-out energy asymmetries during PREs are analyzed. After that, the peak parallel energy fluence during PREs is studied. Finally, projections to future devices are outlined and compared to present-day divertor material limits.

6.4.1 Energy in-out asymmetry

In section 5.6 the in-out heat load asymmetry in steady state conditions during I-mode discharges without PREs was studied. In this section, the in-out divertor heat load asymmetry during I-mode PREs is described. The PRE energy deposited onto the divertor can be evaluated directly from heat flux measurements inferred by the IR camera. The heat flux deposited onto the divertor tile changes across the tile in the toroidal direction, as the incident angle between the magnetic field lines and the divertor target changes due to the geometry of the tile. Therefore, heat fluxes are evaluated at the toroidal position where the "tile-average" heat flux is deposited onto the tile. The power partition to the inner and outer divertor is calculated by integrating the tile-averaged heat flux over the toroidal angle and over the s-coordinate of the tile which is the mapping of a radial coordinate on the divertor tile.
Panel (a) in Fig. 6.17 shows the temporal evolution of the inner (red) and outer (blue) divertor power load during a PRE. Both inner and outer divertor power exhibit a substantial increase during the PRE, which is captured in a single time point. This is consistent with the average PRE deposition time evaluated in section 6.3.1 of about 0.7 ms and the IR camera measurement frequency of 1500 Hz (i.e., once every 0.66 ms).
Panels (b) and (c) in Fig. 6.17 show the time evolution of the cumulative energy reaching the outer and inner divertor target, respectively. The cumulative energy is defined as:

$$E_{\mathrm{x,div}}(t) = \int_0^t P_{\mathrm{x,div}}\, \mathrm{d}t, \tag{6.1}$$

where the subscript "x" can refer to the inner or outer divertor target. The cumulative energy rises linearly over time; however during a PRE, an additional amount of energy reaches the divertor targets, causing $E_{\mathrm{x,div}}$ to jump. The energy increase due to the PRE, E_{PRE}, is then calculated as shown in Fig. 6.17 (b) – (c). Figure 6.17 (d) shows the difference between the outer and inner divertor PRE energy compared to the total PRE energy reaching the

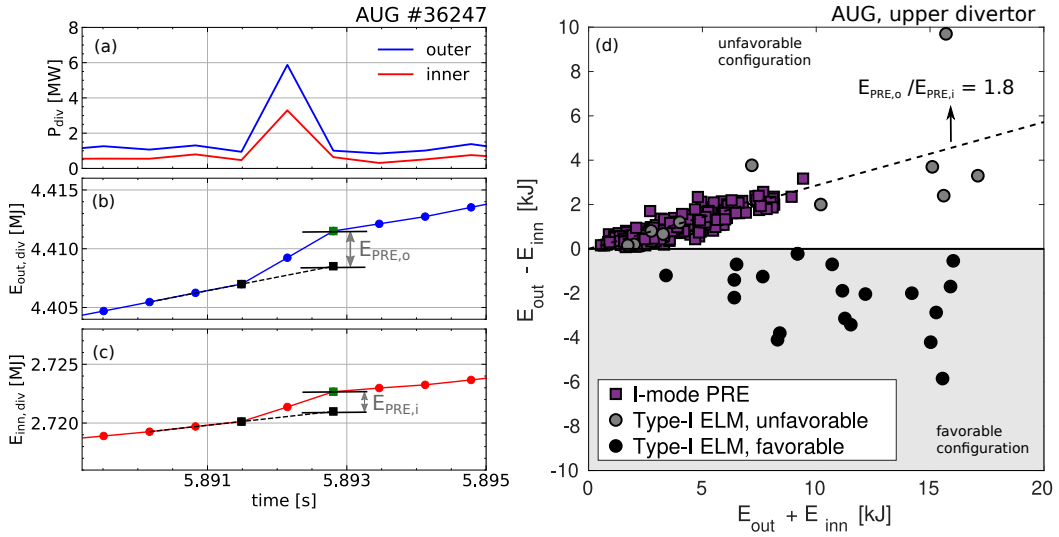

Figure 6.17: Temporal evolution of outer (blue) and inner (red) power to the upper divertor (panel (a)) and of the cumulative energy reaching the outer (panel (b)) and inner (panel (c)) divertor targets. (d) Difference between the outer and inner divertor energy against the total energy reaching the divertor targets for both I-mode PREs and type-I ELMs. A clear asymmetry in favor of the outer divertor target is observed for I-mode PREs and for type-I ELMs in the unfavorable configuration.

divertor targets for several discharges. In addition, type-I ELM data obtained from upper single null H-mode discharges in favorable and unfavorable configuration (Fig. 2.13) are plotted. All the PREs analyzed exhibit $E_{\mathrm{PRE,o}} > E_{\mathrm{PRE,i}}$, i.e. an energy asymmetry in favor of the outer divertor target. The out/in target energy ratio is about $E_{\mathrm{PRE,o}}/E_{\mathrm{PRE,i}} = 1.8$ in the analyzed discharges. This result is in line with the energy asymmetry previously found in type-I ELM and shown again in Fig. 6.17 (d): In the favorable configuration, more energy is deposited onto the inner divertor target [82, 90, 186, 187], whereas in the unfavorable configuration the asymmetry reverses in favor of the outer target [90]. Hence, the SOL transport during I-mode PREs does not seem to substantially differ from what has been previously found for type-I ELMs. Also, the out/in divertor energy ratio during I-mode PREs is equal to the out/in divertor power ratio during steady-state conditions in I-mode without PREs, see Fig. 5.10 (b). The practical consequence of this observation is that the outer divertor target is the more vulnerable to damage due to I-mode PREs.

6.4.2 Peak energy fluence

As described in section 2.2.4, the divertor energy fluence ϵ is a crucial parameter to asses thermomechanical stresses induced by transient heat loads in the divertor tile. In this section, the divertor energy fluence during PREs is analyzed. Figure 6.18 shows a typical parallel energy fluence profile measured onto the outer lower divertor tile by means of IR cameras. Between two PREs

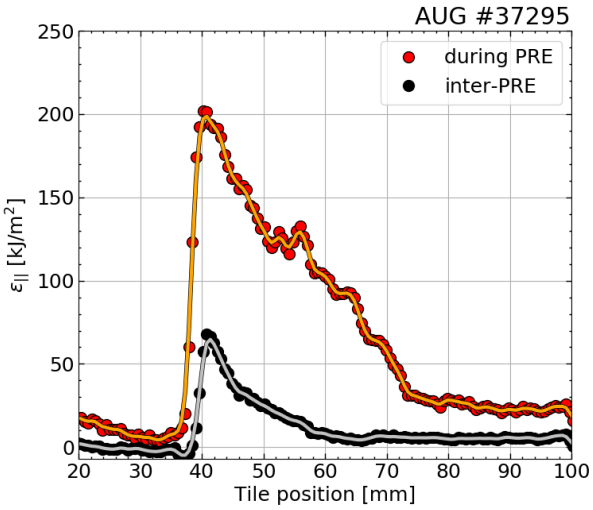

Figure 6.18: Parallel energy fluence onto the lower outer divertor during one PRE (red) and in the inter-PRE phase (black).

the energy fluence profile (black circles) has the typical shape already introduced in section 2.1.2. During a PRE (red circles), the profile shape broadens and the peak energy fluence increases. From such profiles, the peak parallel energy fluence is calculated using the approach described in section 2.2.6. Measurements were carried out in both I-mode USN and LSN discharges. Due to the wide view of the IR camera over the upper open divertor, both inner and outer parallel energy fluences are available in USN plasmas. In contrast, only outer divertor heat fluxes are available for the LSN I-mode discharges. The main parameters of the analyzed discharges are summarized in table 6.1.

	LSN	USN
Discharges	4	4
W_{MHD} (kJ)	174–242	388–397
$\overline{n}_e$ (10^{19} m^{-3})	3.3–4.5	4.6–5.2
$p_{\mathrm{e}}^{\mathrm{ped}}$ (kPa)	1.8–3.1	3.5–4.3
$T_{\mathrm{e}}^{\mathrm{ped}}$ (keV)	0.4–0.6	0.6–0.8
q_{95}	5.2–7.2	4.1
I_{p} (MA)	0.6–0.8	1.0
β_{pol}	0.5–0.9	0.6
B_{t} (T)	2.5	2.5
δ	0.2	0.2
κ	1.7	1.7

Table 6.1: Parameter range of the I-mode ASDEX Upgrade discharges analyzed.

The plasma stored energy W_{MHD}, as well as the line-averaged electron density $\overline{n}_e$, is lower for the LSN discharges than for the USN pulses. In addition, a variation in the pedestal top electron pressure and temperature, p_e^{ped} and T_e^{ped}, is present.

The peak energy fluence shown below is the average value of an ensemble of PREs taken in phases with constant plasma parameters. These data are plotted in Fig. 6.19 versus the parallel energy fluence predicted by the model introduced for type-I ELMs (see Eq. 2.44). Type-I ELM peak energy fluence

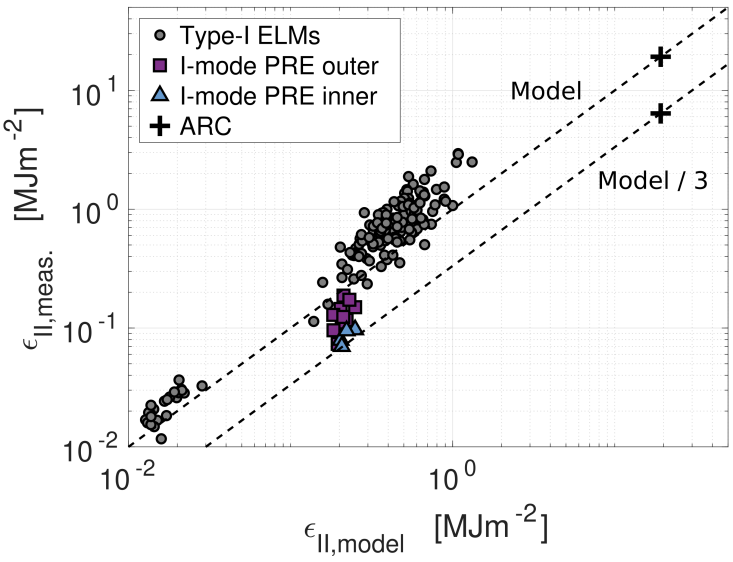

Figure 6.19: Measured parallel peak energy fluence against the model prediction. The peak energy fluence of I-mode PREs is lower than that of type-I ELMs for the same $\epsilon_{||,\mathrm{model}}$. The model prediction gives an upper boundary of the I-mode PRE energy fluences, while a lower boundary is found dividing the model prediction by three.

data from several devices [26] are also plotted for comparison. I-mode PREs exhibit energy fluences that are smaller than those of type-I ELMs for the same $\epsilon_{||,\mathrm{model}}$. Also inner divertor energy fluences are consistently lower than the outer divertor ones, for the USN discharges analyzed here. In Fig. 6.19 we additionally draw a line that shows a 1/3 of the model prediction. The I-mode PRE energy fluence data fall between these two lines. In particular, Eq. 2.44 represents an upper boundary for I-mode PREs, while it is a lower boundary for type-I ELMs.

The restricted dataset available so far does not allow us to conclude that I-mode PRE energy fluences scale similarly to type-I ELMs, although these data show a similar dependency. In particular, there is no large variation (when compared to a multi-machine study) of the pedestal top electron pressure. Therefore, achievement and study of I-mode PREs in other devices is fundamental for any robust extrapolation to future devices. Nonetheless, preliminary projections may be attempted assuming that the energy fluence model introduced for type-I ELMs also represents I-mode PREs. In support of this assumption is not only the overall correspondence between first I-mode PRE energy fluence measurements and the model, but also the similarities in SOL transport of type-I ELMs and I-mode PREs shown in this work.

6.4.3 Projections to ARC

ARC [165] is a concept of a compact tokamak ($R = 3.3\,\mathrm{m}$ and $a = 1.13\,\mathrm{m}$) at high $B = 9.2\,\mathrm{T}$ that could potentially operate in I-mode. The envisaged I-mode pedestal top electron pressure in ARC is around 64 kPa [165] for the $q_{95} = 6$ scenario. This leads to a projected parallel peak energy fluence that ranges between $6 - 19\,\mathrm{MJ/m^2}$, with the upper and lower boundaries given by Eq. 2.44 and its 0.33-times lower value. Divertor material limits strongly depend on the divertor target geometry and on the plasma facing component's material. The conceptual design of the ARC divertor [188] has to date been based on the ITER divertor design [189, 190], therefore ITER material limits are used in the following discussion. In this respect, a deposited energy fluence limit of about $0.3\,\mathrm{MJ/m^2}$ has been found after exposure of ITER divertor monoblocks to 10^5 cycles of 500 µs long transient events [88]. A most recent study that took into account geometrical effects of the castellated structure further lowered this limit to $\epsilon_{\perp,\mathrm{lim}} = 0.15\,\mathrm{MJ/m^2}$ [89]. This limit may be further refined for ARC, given the presence of molten salt coolant instead of water, which needs corrosion issues to be taken into account. Nevertheless, using the actual ITER material limit and an optimistic perpendicular-to-parallel conversion factor of 20, the limit parallel energy fluence at the divertor target is $3\,\mathrm{MJ/m^2}$. The lower and higher PRE projected peak energy fluences are a factor of 2 and 6 above the limit, respectively. However, it should be noted that ARC will benefit from the double null configuration that includes a long-leg and a secondary X-point divertor geometry in both the upper and lower divertor chambers [188]. This configuration will introduce enhanced SOL dissipation effects and a different heat flux distribution on the targets with respect to present-day machines. Therefore, it is expected that the above-mentioned projected values could be lowered by this divertor configuration.

6.5 Discussion

Throughout this chapter, several features of I-mode PREs have been studied and compared to ELMs. Because of the similarities in SOL transport shown in the previous sections, it is of interest to review the differences between PREs and the known classes of ELMs.

To begin with, while type-I ELMs occur only when the pedestal is close to the ideal peeling-ballooning stability boundary, PREs appear when the pedestal is ideal peeling-ballooning stable. This marks a difference in the instability criterion which triggers PREs and type-I ELMs. Also, PREs exhibit characteristics different from type-III ELMs. While PREs have a frequency of occurrence which slightly increases with increasing heating power, type-III ELMs show a frequency which decreases with increasing heating power. Regarding the comparison with type-II ELMs, PREs are different in the plasma conditions in which they appear. Type-II ELMs appear only in high-shaping plasmas with

high separatrix densities ($n_e^{\text{sep}} = 4 - 5 \times 10^{19}\,\text{m}^{-3}$ at AUG [65]), while I-modes are obtained at low separatrix densities ($n_e^{\text{sep}} = 1.5 - 2 \times 10^{19}\,\text{m}^{-3}$ at AUG) and in less-shaped plasmas. Moreover, PREs are not accompanied by detectable magnetic precursors, while type-I, type-II and type-III ELMs do. For these reasons, PREs do not fall in a previously known class of ELMs.

In conclusion, some considerations on PREs compatibility with a fusion reactor can be outlined. Based on the projections shown in section 6.4.3, PRE divertor energy fluences might be above the divertor material limit in a fusion power plant operating in I-mode. For this reason, these transient events should be avoided in a fusion reactor. This can be achieved by operating the I-mode at a safe distance from the H-mode transition boundary, while retaining at the same time the high energy confinement, as shown in Fig. 6.3. Moreover, I-mode PREs could be used to monitor the proximity to H-mode and hence to avoid the plasma entering an undesired type-I ELMy H-mode.

Chapter 7

Summary, conclusions and outlook

The regime in which plasmas will be operated in a fusion power plant needs to be compatible with high energy confinement and the protection of the plasma facing components, in particular the divertor target plates. The presently favored regime for a reactor plasma is the high confinement (H-) mode, which is distinct from the low confinement (L-) mode by an edge particle and energy transport barrier. H-mode plasmas feature increased energy and particle confinement, along with the appearance of edge localized MHD instabilities, called type-I ELMs, which help to control the impurity content in the plasma by increasing their outward transport. However, intermittent high heat fluxes generated by type I ELMs are transported along the open magnetic field lines of the scrape-off layer (SOL) to the divertor, where they reduce the lifetime of the divertor targets. Therefore, type-I ELMs will not be accepted for a fusion power plant.
A confinement regime that does not have type-I ELMs is the improved confinement (I-) mode. It features high energy confinement and relatively poor particle confinement. In this way, it combines the desired properties of L-mode and H-mode plasmas, namely reduced impurity accumulation in the plasma core and high confinement for large fusion energy production. The compatibility of this confinement regime with the strict requirements of a fusion power plant still needs to be assessed. In this thesis, investigations of both stationary and transient I-mode power loads on the divertor target plates are carried out at the ASDEX Upgrade tokamak, to study the compatibility of such a confinement regime with the low divertor power loads required in a fusion power plant.

Summary

The first part of this thesis is devoted to analyzing steady-state divertor power loads in I-mode and in other confinement regimes at ASDEX Upgrade. A key parameter that sets the peak heat flux onto the divertor target is the power decay length λ_q. The larger λ_q, the lower is the peak heat flux on the divertor. To predict λ_q in future devices, it is important to understand how this

quantity scales with plasma parameters. In this regard, two research questions are addressed in this thesis: 1) How does λ_q scale with local edge parameters across different confinement regimes (and why)? 2) Are there simple transport models able to describe the parameter dependence of λ_q?
Another important aspect of steady-state power loads is the heat flux asymmetry between inner and outer divertor targets. For the same power entering the SOL, a strongly unbalanced out-in asymmetry will lead to more power reaching one divertor target and thus to a larger peak heat flux. In this respect, the following question is tackled: how symmetric are divertor heat loads in I-mode compared to other confinement regimes?
To answer these questions, a database has been assembled. It encompasses different confinement regimes (L-mode, I-mode, inter-ELM H-mode and ELM-free H-mode), different divertor geometries (open vs. closed) and different ion ∇B drift directions (pointing to and away from the active magnetic X-point). Moreover, in this database not only divertor heat flux quantities from infrared measurements, but also edge pedestal and SOL kinetic gradients from various plasma diagnostics are analyzed.
It is found that a simple SOL transport model gives a reasonable approximation to estimate λ_q in attached divertor regimes, i.e. $\lambda_q = 2/7\,\lambda_{T_e}$. In this model, it is assumed that the heat is mainly transported by electron heat conduction. Nevertheless, analyzing correlations with plasma parameters of the confined region, it is found that λ_q better correlates with edge electron pressure evaluated at a normalized radius of $\rho_{\mathrm{pol}} = 0.95$ (p_e^{95}), rather than with the edge electron temperature, see table 5.2. The scaling found is: $\lambda_q[\mathrm{mm}] = 2.45 \pm 0.02 \times (\, p_e^{95}\,[\mathrm{kPa}]\,)^{-0.34\pm0.01}$. It groups together all the confinement regimes analyzed. Considering the projected pedestal top electron pressure in H-mode and I-mode for a reactor [191], the scaling law predicts $\lambda_q^{\mathrm{H}} = 0.6\,\mathrm{mm}$ for H-mode plasmas and $\lambda_q^{\mathrm{I}} = 0.65\,\mathrm{mm}$ for I-mode plasmas. These values can be considered identical within the experimental errorbars.
In addition, it is found that edge electron pressure gradients, no matter if taken inside or outside the last closed flux surface, are robust local plasma parameters able to scale λ_q across all confinement regimes. Furthermore, SOL and pedestal electron pressure gradients are found to be correlated in the analyzed database. These observations explain why a SOL quantity such as λ_q is correlated to the edge electron pressure in the confined region p_e^{95}. Physically, this suggests that both near-SOL and pedestal pressure gradients adjust themselves to satisfy the same marginal stability constraint, as proposed in [91,161]. The same observation may also point towards an important role of turbulence spreading [105] (i.e. the non-local component of turbulence) in setting the radial transport in the SOL, as suggested in [163].
In addition, this database allowed us to study also out-in divertor asymmetries across different confinement regimes. It is found that I-mode plasmas have more balanced power and heat fluxes than H-mode plasmas in forward-field configuration. This is due to the role of $\vec{E} \times \vec{B}$ drifts in the SOL, which

contribute to reduce the out-in asymmetry in the reversed-field configuration, i.e. in the configuration where I-mode plasmas are obtained.

The second part of this thesis reports on a first extensive study of pedestal relaxation events (PREs) found in I-mode plasmas at AUG. These events induce transient heat loads on the divertor targets and, hence, need to be investigated to predict their compatibility with a fusion power plant. In this regard, the following research questions are addressed in this thesis: 1) When do PREs appear and how do they compare to previously known classes of ELMs? 2) Is PRE's transport different to that of type-I ELMs and how much energy do they transport to the divertor?
With regard to the first question, I-mode PREs appear close to the H-mode transition in the typical I-mode operational range at AUG. Also, no further enhancement of the energy confinement time is observed when PREs appear, i.e. I-mode discharges both with and without PREs can reach high confinement quality with a confinement factor of $H_{98} \simeq 0.8$–1.0. This indicates that stationary and high-confinement I-mode plasmas without PREs can be achieved. Additionally, since I-mode PREs are observed as the plasma nears the H-mode transition, they could be used to monitor the proximity to H-mode and hence to avoid the plasma entering an undesired ELMy H-mode regime.
Also, PREs do not belong to an already known class of ELMs. Indeed, they are not type-I ELMs, as the pedestal during PREs is ideal peeling-ballooning stable. They are not type-II ELMs, as PREs occur at low separatrix densities and in not-strongly-shaped plasmas. Also, they are not type-III ELMs, as their frequency of occurrence does not decrease with increasing heating power. Moreover, no magnetic precursors have been detected before PREs occur.
Regarding the second question, no major qualitative differences were found between the transport of type-I ELMs and I-mode PREs. The events share similar timescales of about 700 µs; they both feature the presence of filamentary structures propagating in the SOL; they are both characterized by toroidally asymmetric energy effluxes at the outer midplane, which, in the case of PREs, can be described by a quasi-mode number of $n_{\mathrm{QMN}}^{\mathrm{PRE}} = 10 - 28$. They also share the same asymmetry in the energy deposited at the inner and outer divertor targets. Indeed, in the reversed-field configuration, both I-mode PREs and type-I ELMs deposit more energy on the outer divertor target. This has the practical consequence that the outer divertor target is more stressed by I-mode PREs.
The relative PRE energy loss $\Delta W/W_{\mathrm{MHD}}$ is about 1 %, being lower than the corresponding type-I ELM loss for the same collisionality at the plasma edge. Also, the peak of the parallel energy fluence measured on the divertor during PREs is lower than that of type-I ELMs for the same edge electron pressure. The energy fluence predicted by the model introduced in [26] represents an upper boundary for I-mode PREs, while a lower boundary is found by dividing the model by a factor of three. Based on these two boundaries, projections to a

reactor-like tokamak were evaluated, finding a maximum heat fluence between 6–19 $\mathrm{MJ/m^2}$, which is above the material limit for the ITER divertor.

Conclusions

In conclusion, regarding steady-state divertor power loads, the main implication of these findings is that λ_q scales unfavorably with the edge electron pressure p_e^{95} and/or with the edge electron pressure gradient. I-mode plasmas exhibit a lower edge electron pressure than H-mode plasmas, due to the lack of a density pedestal. Therefore, from this analysis a broader λ_q is expected in I-mode. However, when reactor-like edge electron pressures are considered, the scaling law presented here predicts only a marginal increase of λ_q, from about 0.6 mm to 0.65 mm. Hence, to make steady-state divertor heat loads tolerable, similar challenges exist for both I-mode and H-mode plasmas.
In terms of risk-management, the more balanced out-in heat flux of I-mode is a desirable property of a confinement regime. Indeed, in a fusion power plant the divertor targets will be detached; however, in case of a transient plasma re-attachment the peak divertor heat flux will be more tolerable when it is symmetric, as it is in I-mode.
Concerning transient divertor power loads, the divertor energy fluences induced by PREs might be above material limits in a reactor. For this reason, the avoidance of these transient events should be envisaged. This can be achieved in AUG by operating the I-mode far from the H-mode transition, while retaining the high energy confinement. Moreover, in a fusion reactor I-mode PREs could be used to monitor the proximity to H-mode and hence to avoid the plasma entering an undesired ELMy H-mode.

Outlook

The correlation between SOL and pedestal electron pressure gradient lengths found in this work needs to be challenged by studies analyzing different plasma conditions. Other tokamaks with the same diagnostic capabilities as ASDEX Upgrade could verify such correlation in the same confinement regimes analyzed here.
Regarding I-mode PREs, carrying out a similar study in Alcator C-Mod is of particular interest. This would allow to explore a broader range of magnetic field strengths, plasma currents and electron densities which are inaccessible at AUG, and to add divertor energy fluence data which could improve the extrapolation capability to next-step devices.

Bibliography

[1] H. Cabal *et al.*, "Fusion power in a future low carbon global electricity system," *Energy Strategy Reviews*, vol. 15, pp. 1–8, 2017.

[2] A. Yaksic and J. E. Tilton, "Using the cumulative availability curve to assess the threat of mineral depletion: The case of lithium," *Resources Policy*, vol. 34, no. 4, pp. 185–194, 2009.

[3] C. Grosjean *et al.*, "Assessment of world lithium resources and consequences of their geographic distribution on the expected development of the electric vehicle industry," *Renewable and Sustainable Energy Reviews*, vol. 16, no. 3, pp. 1735–1744, 2012.

[4] J. Lawson, "Some criteria for a power producing thermonuclear reactor," *Proceedings of the Physical Society. Section B*, vol. 70, no. 1, p. 6, 1957.

[5] S. Pfalzner, *An Introduction to Inertial Confinement Fusion*. New York, USA: Taylor and Francis, 2006.

[6] Dolgov-Saveliev, "Investigations of the stability and heating of plasmas in toroidal chambers," *Proc. Second United Nations Intern. Conf. on the Peaceful Use of Atomic Energy*, p. 2527, 1958.

[7] Y. Xu, "A general comparison between tokamak and stellarator plasmas," *Matter and Radiation at Extremes*, vol. 1, no. 4, pp. 192–200, 2016.

[8] E. G. Highcock *et al.*, "Optimisation of confinement in a fusion reactor using a nonlinear turbulence model," *Journal of Plasma Physics*, vol. 84, no. 2, p. 905840208, 2018.

[9] P. Rebut, R. Bickerton, and B. Keen, "The Joint European Torus: installation, first results and prospects," *Nuclear Fusion*, vol. 25, pp. 1011–1022, sep 1985.

[10] H. Meyer *et al.*, "Overview of physics studies on ASDEX Upgrade," *Nuclear Fusion*, vol. 59, p. 112014, jul 2019.

[11] J. Harrison *et al.*, "Overview of new MAST physics in anticipation of first results from MAST Upgrade," *Nuclear Fusion*, vol. 59, p. 112011, jun 2019.

[12] S. Coda *et al.*, "Overview of the TCV tokamak program: scientific progress and facility upgrades," *Nuclear Fusion*, vol. 57, p. 102011, jun 2017.

[13] H. Takenaga, "Overview of JT-60U results for the development of a steady-state advanced tokamak scenario," *Nuclear Fusion*, vol. 47, pp. S563–S578, sep 2007.

[14] S. Wu, "An overview of the EAST project," *Fusion Engineering and Design*, vol. 82, no. 5, pp. 463–471, 2007. Proceedings of the 24th Symposium on Fusion Technology.

[15] J. L. Luxon, "A brief introduction to the DIII-D tokamak," *Fusion Science and Technology*, vol. 48, no. 2, pp. 828–833, 2005.

[16] I. H. Hutchinson *et al.*, "First results from Alcator-C-MOD," *Physics of Plasmas*, vol. 1, no. 5, pp. 1511–1518, 1994.

[17] K. Ikeda, "Progress in the ITER physics basis," *Nuclear Fusion*, vol. 47, jun 2007.

[18] G. Matthews, "Material migration in divertor tokamaks," *Journal of Nuclear Materials*, vol. 337-339, pp. 1 – 9, 2005. PSI-16.

[19] D. Yuang, *Modelling of the radiative power loss from the plasma of the Tore Supra tokamak*. Master thesis, Royal Institute of Technology, Stockholm, Sweden, 2008.

[20] L. Aho-Mantila, *Divertor plasma conditions and their effect on carbon migration in the ASDEX Upgrade tokamak*. PhD thesis, VTT Technical Research Centre of Finland, 2011.

[21] M. Keilhacker *et al.*, "The ASDEX divertor tokamak," *Nuclear Fusion*, vol. 25, pp. 1045–1054, sep 1985.

[22] F. Wagner *et al.*, "Regime of improved confinement and high beta in neutral-beam-heated divertor discharges of the ASDEX tokamak," *Phys. Rev. Lett.*, vol. 49, no. 19, p. 1408, 1982.

[23] M. Keilhacker *et al.*, "Confinement studies in L and H-type ASDEX discharges," *Plasma Physics and Controlled Fusion*, vol. 26, pp. 49–63, jan 1984.

[24] A. W. Leonard, "Edge-localized-modes in tokamaks," *Physics of Plasmas*, vol. 21, no. 9, p. 090501, 2014.

[25] H. Zohm, "Edge localized modes (ELMs)," *Plasma Phys. Control. Fusion*, vol. 38, no. 2, p. 105, 1996.

[26] T. Eich *et al.*, "ELM divertor peak energy fluence scaling to ITER with data from JET, MAST and ASDEX Upgrade," *Nuclear Materials and Energy*, vol. 12, pp. 84–90, 2017. Proceedings of the 22nd International Conference on Plasma Surface Interactions 2016, 22nd PSI.

[27] E. Viezzer, "Access and sustainment of naturally ELM-free and small-ELM regimes," *Nuclear Fusion*, vol. 58, p. 115002, sep 2018.

[28] K. H. Burrell *et al.*, "Quiescent H-mode plasmas in the DIII-D tokamak," *Plasma Physics and Controlled Fusion*, vol. 44, pp. A253–A263, apr 2002.

[29] W. Suttrop *et al.*, "ELM-free stationary H-mode plasmas in the ASDEX Upgrade tokamak," *Plasma Physics and Controlled Fusion*, vol. 45, pp. 1399–1416, jun 2003.

[30] Y. Sakamoto *et al.*, "Impact of toroidal rotation on ELM behaviour in the H-mode on JT-60U," *Plasma Physics and Controlled Fusion*, vol. 46, pp. A299–A304, apr 2004.

[31] E. R. Solano *et al.*, "Observation of confined current ribbon in JET plasmas," *Phys. Rev. Lett.*, vol. 104, p. 185003, May 2010.

[32] M. Greenwald *et al.*, "Characterization of enhanced D_α high-confinement modes in Alcator C-Mod," *Physics of Plasmas*, vol. 6, no. 5, pp. 1943–1949, 1999.

[33] L. Gil *et al.*, "Stationary ELM-free H-mode in ASDEX Upgrade," *Nuclear Fusion*, vol. 60, p. 054003, apr 2020.

[34] E. Marmar *et al.*, "Overview of the Alcator C-Mod Research Program," *Nuclear Fusion*, vol. 49, p. 104014, sep 2009.

[35] A. Kallenbach *et al.*, "Overview of ASDEX Upgrade results," *Nuclear Fusion*, vol. 51, p. 094012, aug 2011.

[36] F. Ryter *et al.*, "H-mode power threshold and transition in ASDEX Upgrade," *Plasma Physics and Controlled Fusion*, vol. 40, pp. 725–729, may 1998.

[37] D. Whyte *et al.*, "I-mode: an H-mode energy confinement regime with L-mode particle transport in Alcator C-Mod," *Nuclear Fusion*, vol. 50, p. 105005, aug 2010.

[38] J. Rice *et al.*, "Core impurity transport in Alcator C-Mod L-, I- and H-mode plasmas," *Nuclear Fusion*, vol. 55, p. 033014, feb 2015.

[39] M. Greenwald, "Density limits in toroidal plasmas," *Plasma Physics and Controlled Fusion*, vol. 44, pp. R27–R53, jul 2002.

[40] ITER Physics Expert Group on Confinement Transport *et al.*, "Chapter 2: Plasma confinement and transport," *Nuclear Fusion*, vol. 39, pp. 2175–2249, dec 1999.

[41] H. Zohm, "On the minimum size of DEMO," *Fusion Science and Technology*, vol. 58, no. 2, pp. 613–624, 2010.

[42] R. Wenninger *et al.*, "DEMO divertor limitations during and in between ELMs," *Nuclear Fusion*, vol. 54, p. 114003, nov 2014.

[43] B. Riccardi *et al.*, "Preliminary results of the experimental study of PFCs exposure to ELMs-like transient loads followed by high heat flux thermal fatigue," *Fusion Engineering and Design*, vol. 86, no. 9, pp. 1665–1668, 2011. Proceedings of the 26th Symposium of Fusion Technology (SOFT-26).

[44] A. Loarte *et al.*, "Power and particle control," *Nucl. Fusion*, vol. 47, no. 6, p. S203, 2007.

[45] P. Stangeby, *The Plasma Boundary of Magnetic Fusion Devices*. Bristol: Institute of Physics Publishing, 2000.

[46] T. Eich *et al.*, "Inter-ELM power decay length for JET and ASDEX Upgrade: Measurement and comparison with heuristic drift-based model," *Phys. Rev. Lett.*, vol. 107, p. 215001, Nov 2011.

[47] M. Faitsch, *Divertor power load studies in ASDEX Upgrade and TCV*. PhD thesis, Ludwig Maximilians University Munich, 2017.

[48] A. Loarte *et al.*, "Multi-machine scaling of the divertor peak heat flux and width for L-mode and H-mode discharges," *Journal of Nuclear Materials*, vol. 266-269, pp. 587–592, 1999.

[49] M. A. Makowski *et al.*, "Analysis of a multi-machine database on divertor heat fluxes," *Phys. Plasmas*, vol. 19, no. 5, p. 056122, 2012.

[50] R. Goldston, "Heuristic drift-based model of the power scrape-off width in low-gas-puff H-mode tokamaks," *Nucl. Fusion*, vol. 52, no. 1, p. 013009, 2011.

[51] C. S. Chang *et al.*, "Gyrokinetic projection of the divertor heat-flux width from present tokamaks to ITER," *Nuclear Fusion*, vol. 57, no. 11, p. 116023, 2017.

[52] X. Xu *et al.*, "Simulations of tokamak boundary plasma turbulence transport in setting the divertor heat flux width," *Nuclear Fusion*, vol. 59, p. 126039, oct 2019.

[53] T. Eich *et al.*, "Scaling of the tokamak near the scrape-off layer H-mode power width and implications for ITER," *Nuclear Fusion*, vol. 53, p. 093031, aug 2013.

[54] D. Brunner *et al.*, "High-resolution heat flux width measurements at reactor-level magnetic fields and observation of a unified width scaling across confinement regimes in the Alcator C-Mod tokamak," *Nuclear Fusion*, vol. 58, p. 094002, jul 2018.

[55] U. Stroth, *Plasmaphysik: Phänomene, Grundladen und Anwendungen.* Springer, 2018.

[56] H. J. Sun *et al.*, "Study of near scrape-off layer (SOL) temperature and density gradient lengths with Thomson scattering," *Plasma Physics and Controlled Fusion*, vol. 57, p. 125011, nov 2015.

[57] M. Faitsch *et al.*, "Change of the scrape-off layer power width with the toroidal B-field direction in ASDEX Upgrade," *Plasma Physics and Controlled Fusion*, vol. 57, p. 075005, may 2015.

[58] R. Pitts *et al.*, "Edge and divertor physics with reversed toroidal field in JET," *Journal of Nuclear Materials*, vol. 337-339, pp. 146–153, 2005. PSI-16.

[59] T. Eich *et al.*, "ELM resolved energy distribution studies in the JET MKII gas-box divertor using infra-red thermography," *Plasma Physics and Controlled Fusion*, vol. 49, pp. 573–604, mar 2007.

[60] P. Gohil *et al.*, "Study of giant edge-localized modes in DIII-D and comparison with ballooning theory," *Phys. Rev. Lett.*, vol. 61, pp. 1603–1606, Oct 1988.

[61] P. Snyder *et al.*, "Pedestal stability comparison and ITER pedestal prediction," *Nuclear Fusion*, vol. 49, p. 085035, jul 2009.

[62] W. Suttrop *et al.*, "Characteristics of edge localized modes in ASDEX Upgrade," *Plasma Physics and Controlled Fusion*, vol. 38, pp. 1407–1410, aug 1996.

[63] C. Perez *et al.*, "Type-I ELM precursor modes in JET," *Nuclear Fusion*, vol. 44, pp. 609–623, apr 2004.

[64] N. Oyama *et al.*, "Fast dynamics of type I ELMs and transport of the ELM pulse in JT-60U," *Nuclear Fusion*, vol. 44, pp. 582–592, apr 2004.

[65] G. Harrer *et al.*, "Parameter dependences of small edge localized modes (ELMs)," *Nuclear Fusion*, vol. 58, p. 112001, sep 2018.

[66] J. Stober *et al.*, "Type II ELMy H modes on ASDEX Upgrade with good confinement at high density," *Nuclear Fusion*, vol. 41, pp. 1123–1134, sep 2001.

[67] G. Saibene *et al.*, "Characterization of small ELM experiments in highly shaped single null and quasi-double-null plasmas in JET," *Nuclear Fusion*, vol. 45, pp. 297–317, apr 2005.

[68] W. Suttrop *et al.*, "Identification of plasma-edge-related operational regime boundaries and the effect of edge instability on confinement in ASDEX Upgrade," *Plasma Physics and Controlled Fusion*, vol. 39, pp. 2051–2066, dec 1997.

[69] R. Sartori *et al.*, "Study of type III ELMs in JET," *Plasma Physics and Controlled Fusion*, vol. 46, pp. 723–750, mar 2004.

[70] A. Loarte *et al.*, "Characteristics of type I ELM energy and particle losses in existing devices and their extrapolation to ITER," *Plasma Physics and Controlled Fusion*, vol. 45, pp. 1549–1569, aug 2003.

[71] M. Honda, "Coulomb logarithm formulae for collisions between species with different temperatures," *Japanese Journal of Applied Physics*, vol. 52, p. 108002, oct 2013.

[72] A. W. Leonard *et al.*, "ELM energy scaling in DIII-D," *Plasma Physics and Controlled Fusion*, vol. 44, pp. 945–954, may 2002.

[73] T. Eich, A. Herrmann, and J. Neuhauser, "Nonaxisymmetric energy deposition pattern on asdex upgrade divertor target plates during type-i edge-localized modes," *Phys. Rev. Lett.*, vol. 91, p. 195003, Nov 2003.

[74] T. Eich *et al.*, "Type-I ELM substructure on the divertor target plates in ASDEX Upgrade," *Plasma Physics and Controlled Fusion*, vol. 47, pp. 815–842, may 2005.

[75] S. Devaux *et al.*, "Type-I ELM filamentary substructure on the JET divertor target," *Journal of Nuclear Materials*, vol. 415, no. 1, Supplement, pp. S865 – S868, 2011. Proceedings of the 19th International Conference on Plasma-Surface Interactions in Controlled Fusion.

[76] A. Kirk *et al.*, "Spatial and temporal structure of edge-localized modes," *Phys. Rev. Lett.*, vol. 92, p. 245002, Jun 2004.

[77] R. J. Maqueda and R. Maingi, "Primary edge localized mode filament structure in the national spherical torus experiment," *Physics of Plasmas*, vol. 16, no. 5, p. 056117, 2009.

[78] N. B. Ayed *et al.*, "Inter-ELM filaments and turbulent transport in the mega-amp spherical tokamak," *Plasma Physics and Controlled Fusion*, vol. 51, p. 035016, jan 2009.

[79] A. J. Thornton *et al.*, "The role of ELM filaments in setting the ELM wetted area in MAST and the implications for future devices," *Plasma Physics and Controlled Fusion*, vol. 59, p. 014047, nov 2016.

[80] A. Herrmann, "Thermal properties of plasma exposed carbon and heat flux calculations on a spatial scale of a few microns," *Journal of Nuclear Materials*, vol. 337-339, pp. 907 – 911, 2005. PSI-16.

[81] B. Sieglin, *Experimental Investigation of Heat Transport and Divertor Loads of Fusion Plasmas in All Metal ASDEX Upgrade and JET*. PhD thesis, Techincal University Munich, 2014.

[82] A. Herrmann *et al.*, "Stationary and transient divertor heat flux profiles and extrapolation to ITER," *Journal of Nuclear Materials*, vol. 313-316, pp. 759 – 767, 2003. Plasma-Surface Interactions in Controlled Fusion Devices 15.

[83] T. Eich *et al.*, "Power deposition measurements in deuterium and helium discharges in JET MKIIGB divertor by IR-thermography," *Journal of Nuclear Materials*, vol. 313-316, pp. 919 – 924, 2003. Plasma-Surface Interactions in Controlled Fusion Devices 15.

[84] R. Pitts *et al.*, "ELM transport in the JET scrape-off layer," *Nuclear Fusion*, vol. 47, pp. 1437–1448, oct 2007.

[85] T. Eich *et al.*, "Type-I ELM power deposition profile width and temporal shape in JET," *Journal of Nuclear Materials*, vol. 415, no. 1, Supplement, pp. S856 – S859, 2011. Proceedings of the 19th International Conference on Plasma-Surface Interactions in Controlled Fusion.

[86] W. Fundamenski, R. A. Pitts, and J. E. contributors, "A model of ELM filament energy evolution due to parallel losses," *Plasma Physics and Controlled Fusion*, vol. 48, pp. 109–156, dec 2005.

[87] T. Eich *et al.*, "On the asymmetries of elm divertor power deposition in JET and ASDEX Upgrade," *Journal of Nuclear Materials*, vol. 390-391, pp. 760 – 763, 2009. Proceedings of the 18th International Conference on Plasma-Surface Interactions in Controlled Fusion Device.

[88] T. Loewenhoff *et al.*, "ITER-W monoblocks under high pulse number transient heat loads at high temperature," *Journal of Nuclear Materials*, vol. 463, pp. 202 – 205, 2015. PLASMA-SURFACE INTERACTIONS 21.

[89] J. Gunn *et al.*, "Ion orbit modelling of ELM heat loads on ITER divertor vertical targets," *Nuclear Materials and Energy*, vol. 12, pp. 75 – 83, 2017. Proceedings of the 22nd International Conference on Plasma Surface Interactions 2016, 22nd PSI.

[90] T. Eich *et al.*, "Divertor power deposition and target current asymmetries during type-I ELMs in ASDEX Upgrade and JET," *Journal of Nuclear Materials*, vol. 363-365, pp. 989 – 993, 2007. Plasma-Surface Interactions-17.

[91] B. LaBombard, J. Hughes, D. Mossessian, M. Greenwald, B. Lipschultz, J. Terry, and the Alcator C-Mod Team, "Evidence for electromagnetic fluid drift turbulence controlling the edge plasma state in the Alcator C-Mod tokamak," *Nuclear Fusion*, vol. 45, pp. 1658–1675, nov 2005.

[92] A. Scarabosio *et al.*, "Outer target heat fluxes and power decay length scaling in L-mode plasmas at JET and AUG," *Journal of Nuclear Materials*, vol. 438, pp. S426–S430, 2013. Proceedings of the 20th International Conference on Plasma-Surface Interactions in Controlled Fusion Devices.

[93] B. Sieglin, T. Eich, M. Faitsch, A. Herrmann, and A. Scarabosio, "Investigation of scrape-off layer and divertor heat transport in ASDEX Upgrade L-mode," *Plasma Physics and Controlled Fusion*, vol. 58, p. 055015, apr 2016.

[94] E.-j. Kim and P. H. Diamond, "Zonal flows and transient dynamics of the L−H transition," *Phys. Rev. Lett.*, vol. 90, p. 185006, May 2003.

[95] G. D. Conway *et al.*, "Mean and oscillating plasma flows and turbulence interactions across the L−H confinement transition," *Phys. Rev. Lett.*, vol. 106, p. 065001, Feb 2011.

[96] J. W. Connor and H. R. Wilson, "A review of theories of the L-H transition," *Plasma Physics and Controlled Fusion*, vol. 42, pp. R1–R74, dec 1999.

[97] M. Cavedon *et al.*, "Interplay between turbulence, neoclassical and zonal flows during the transition from low to high confinement mode at ASDEX Upgrade," *Nuclear Fusion*, vol. 57, p. 014002, oct 2016.

[98] D. Réfy *et al.*, "Identity of the JET M-mode and the ASDEX Upgrade I-phase phenomena," *Nuclear Fusion*, vol. 60, p. 056004, mar 2020.

[99] G. Birkenmeier *et al.*, "Magnetic structure and frequency scaling of limit-cycle oscillations close to L- to H-mode transitions," *Nuclear Fusion*, vol. 56, p. 086009, jul 2016.

[100] A. Hubbard *et al.*, "Physics and performance of the I-mode regime over an expanded operating space on Alcator C-Mod," *Nuclear Fusion*, vol. 57, p. 126039, oct 2017.

[101] A. E. Hubbard *et al.*, "Edge energy transport barrier and turbulence in the I-mode regime on Alcator C-Mod," *Physics of Plasmas*, vol. 18, no. 5, p. 056115, 2011.

[102] F. Ryter *et al.*, "I-mode studies at ASDEX Upgrade: L-I and I-H transitions, pedestal and confinement properties," *Nuclear Fusion*, vol. 57, p. 016004, oct 2016.

[103] Y. R. Martin *et al.*, "Power requirement for accessing the H-mode in ITER," *Journal of Physics: Conference Series*, vol. 123, p. 012033, jul 2008.

[104] T. Happel *et al.*, "The I-mode confinement regime at ASDEX Upgrade: global properties and characterization of strongly intermittent density fluctuations," *Plasma Physics and Controlled Fusion*, vol. 59, p. 014004, oct 2016.

[105] P. Manz *et al.*, "Geodesic oscillations and the weakly coherent mode in the I-mode of ASDEX Upgrade," *Nuclear Fusion*, vol. 55, p. 083004, jun 2015.

[106] X. Feng *et al.*, "I-mode investigation on the experimental advanced superconducting tokamak," *Nuclear Fusion*, vol. 59, p. 096025, jul 2019.

[107] P. Manz *et al.*, "Physical mechanism behind and access to the I-mode confinement regime in tokamaks," *Nuclear Fusion*, vol. 60, p. 096011, aug 2020.

[108] A. White *et al.*, "Electron temperature fluctuations associated with the weakly coherent mode in the edge of I-mode plasmas," *Nuclear Fusion*, vol. 51, p. 113005, oct 2011.

[109] Z. X. Liu *et al.*, "The physics mechanisms of the weakly coherent mode in the Alcator C-Mod tokamak," *Physics of Plasmas*, vol. 23, no. 12, p. 120703, 2016.

[110] T. Happel *et al.*, "Turbulence intermittency linked to the weakly coherent mode in ASDEX Upgrade I-mode plasmas," *Nuclear Fusion*, vol. 56, p. 064004, may 2016.

[111] T. Happel *et al.*, "Stationarity of I-mode operation and I-mode divertor heat fluxes on the ASDEX Upgrade tokamak," *Nuclear Materials and Energy*, vol. 18, pp. 159 – 165, 2019.

[112] J. R. Walk *et al.*, "Edge-localized mode avoidance and pedestal structure in I-mode plasmas," *Physics of Plasmas*, vol. 21, no. 5, p. 056103, 2014.

[113] A. Sykes and J. A. Wesson, "Relaxation instability in tokamaks," *Phys. Rev. Lett.*, vol. 37, pp. 140–143, Jul 1976.

[114] J. Wesson and D. Campbell, *Tokamaks*. Oxford University Press, 2011.

[115] T. N. Carlstrom *et al.*, "Comparison of a drift effect model with measured H-mode power thresholds," *Plasma Physics and Controlled Fusion*, vol. 40, pp. 669–672, may 1998.

[116] Y. R. Martin and T. team, "Synchronization of L-mode to H-mode transitions on the sawtooth cycle in ohmic TCV plasmas," *Plasma Physics and Controlled Fusion*, vol. 46, pp. A77–A85, apr 2004.

[117] L. Shao *et al.*, "L-mode to H-mode transition triggered by sawtooth-induced heat flux in EAST," *Physics Letters A*, vol. 384, no. 9, p. 126184, 2020.

[118] I. Cziegler *et al.*, "Fluctuating zonal flows in the I-mode regime in Alcator C-Mod," *Physics of Plasmas*, vol. 20, no. 5, p. 055904, 2013.

[119] J. Terry *et al.*, "Heat-flux footprints for I-mode and EDA H-mode plasmas on Alcator C-Mod," *Journal of Nuclear Materials*, vol. 438, pp. S212 – S215, 2013. Proceedings of the 20th International Conference on Plasma-Surface Interactions in Controlled Fusion Devices.

[120] D. Brunner *et al.*, "The dependence of divertor power sharing on magnetic flux balance in near double-null configurations on Alcator C-Mod," *Nuclear Fusion*, vol. 58, p. 076010, may 2018.

[121] R. Neu *et al.*, "Plasma wall interaction and its implication in an all tungsten divertor tokamak," *Plasma Physics and Controlled Fusion*, vol. 49, pp. B59–B70, nov 2007.

[122] B. Streibl *et al.*, "Chapter 2: Machine design, fueling, and heating in ASDEX Upgrade," *Fusion Science and Technology*, vol. 44, no. 3, pp. 578–592, 2003.

[123] Wagner, D. *et al.*, "Extension of the multi-frequency ECRH system at ASDEX Upgrade," *EPJ Web Conf.*, vol. 149, p. 03004, 2017.

[124] M. Planck, "Ueber das gesetz der energieverteilung im normalspectrum," *Annalen der Physik*, vol. 309, no. 3, pp. 553–563, 1901.

[125] A. Herrmann *et al.*, "Real-time protection of in-vessel components in ASDEX Upgrade," *Fusion Engineering and Design*, vol. 86, no. 6, pp. 530 – 534, 2011. Proceedings of the 26th Symposium of Fusion Technology (SOFT-26).

[126] A. Herrmann, W. Junker, K. Gunther, S. Bosch, M. Kaufmann, J. Neuhauser, G. Pautasso, T. Richter, and R. Schneider, "Energy flux to the ASDEX Upgrade diverter plates determined by thermography and calorimetry," *Plasma Phys. Control. Fusion*, vol. 37, no. 1, p. 17, 1995.

[127] B. Sieglin, M. Faitsch, A. Herrmann, B. Brucker, T. Eich, L. Kammerloher, and S. Martinov, "Real time capable infrared thermography for ASDEX Upgrade," *Rev. Sci. Instrum.*, vol. 86, no. 11, p. 113502, 2015.

[128] D. Nille, U. von Toussaint, B. Sieglin, and M. Faitsch, "Probabilistic inference of surface heat flux densities from infrared thermography," *Bayesian Inference and Maximum Entropy Methods in Science and Engineering*, 2018.

[129] I. H. Hutchinson, *Principles of Plasma Diagnostics*. Cambridge University Press, 2001.

[130] B. Kurzan and H. D. Murmann, "Edge and core thomson scattering systems and their calibration on the ASDEX Upgrade tokamak," *Review of Scientific Instruments*, vol. 82, no. 10, p. 103501, 2011.

[131] L. Barrera *et al.*, "Inboard and outboard electron temperature profile measurements in JET using ECE diagnostics," *Plasma Physics and Controlled Fusion*, vol. 52, p. 085010, jul 2010.

[132] A. Mlynek *et al.*, "Design of a digital multiradian phase detector and its application in fusion plasma interferometry," *Review of Scientific Instruments*, vol. 81, no. 3, p. 033507, 2010.

[133] A. Silva *et al.*, "Ultrafast broadband frequency modulation of a continuous wave reflectometry system to measure density profiles on ASDEX Upgrade," *Review of Scientific Instruments*, vol. 67, no. 12, pp. 4138–4145, 1996.

[134] L. Cupido *et al.*, "Frequency hopping millimeter-wave reflectometry in ASDEX Upgrade," *Review of Scientific Instruments*, vol. 77, no. 10, p. 10E915, 2006.

[135] P. Varela *et al.*, "Review of data processing techniques for density profile evaluation from broadband FM-CW reflectometry on ASDEX Upgrade," *Nuclear Fusion*, vol. 46, pp. S693–S707, aug 2006.

[136] R. Fischer, E. Wolfrum, J. Schweinzer, *et al.*, "Probabilistic lithium beam data analysis," *Plasma Phys. Control. Fusion*, vol. 50, no. 8, p. 085009, 2008.

[137] J. Schweinzer, E. Wolfrum, F. Aumayr, M. Pockl, H. Winter, R. Schorn, E. Hintz, and A. Unterreiter, "Reconstruction of plasma edge density

profiles from li i (2s-2p) emission profiles," *Plasma Phys. Control. Fusion*, vol. 34, no. 7, p. 1173, 1992.

[138] M. Willensdorfer *et al.*, "Characterization of the Li-BES at ASDEX Upgrade," *Plasma Physics and Controlled Fusion*, vol. 56, p. 025008, jan 2014.

[139] M. Griener *et al.*, "Qualification and implementation of line ratio spectroscopy on helium as plasma edge diagnostic at ASDEX upgrade," *Plasma Physics and Controlled Fusion*, vol. 60, p. 025008, dec 2017.

[140] M. Griener *et al.*, "Helium line ratio spectroscopy for high spatiotemporal resolution plasma edge profile measurements at ASDEX Upgrade," *Review of Scientific Instruments*, vol. 89, no. 10, p. 10D102, 2018.

[141] R. Fischer, C. J. Fuchs, B. Kurzan, W. Suttrop, and E. Wolfrum, "Integrated data analysis of profile diagnostics at ASDEX Upgrade," *Fusion Science and Technology*, vol. 58, no. 2, pp. 675–684, 2010.

[142] M. Cavedon, *The role of the radial electric field in the development of the edge transport barrier in the ASDEX Upgrade tokamak*. PhD thesis, Technical University of Munich, 2016.

[143] M. Bernert *et al.*, "Application of AXUV diode detectors at ASDEX Upgrade," *Rev. Sci. Instrum.*, vol. 53, no. 3, p. 104003, 2014.

[144] H. Meister *et al.*, "Broad-band efficiency calibration of ITER bolometer prototypes using Pt absorbers on SiN membranes," *Review of Scientific Instruments*, vol. 84, no. 12, p. 123501, 2013.

[145] E. J. Strait *et al.*, "Chapter 2: Magnetic diagnostics," *Fusion Science and Technology*, vol. 53, no. 2, pp. 304–334, 2008.

[146] S. V. Mirnov *et al.*, "The nature of large-scale instabilities in the tokamak," *Soviet Physics Journal of Experimental and Theoretical Physics*, vol. 33, p. 1134, jan 1971.

[147] F. Mink, *Structure and Nonlinear Development of Edge Localized Magnetohydrodynamic Instabilities on the ASDEX Upgrade Tokamak*. PhD thesis, Technical University of Munich, 2018.

[148] D. Silvagni *et al.*, "Scrape-off layer (SOL) power width scaling and correlation between SOL and pedestal gradients across L, I and H-mode plasmas at ASDEX Upgrade," *Plasma Physics and Controlled Fusion*, vol. 62, p. 045015, feb 2020.

[149] T. Eich, B. Sieglin, A. Scarabosio, W. Fundamenski, R. J. Goldston, and A. Herrmann, "Inter-ELM power decay length for JET and ASDEX Upgrade: Measurement and comparison with heuristic drift-based model," *Phys. Rev. Lett.*, vol. 107, p. 215001, Nov 2011.

[150] R. Goldston, "Heuristic drift-based model of the power scrape-off width in low-gas-puff H-mode tokamaks," *Nuclear Fusion*, vol. 52, p. 013009, dec 2011.

[151] B. Sieglin *et al.*, "Investigation of scrape-off layer and divertor heat transport in ASDEX Upgrade L-mode," *Plasma Phys. Control. Fusion*, vol. 58, no. 5, p. 055015, 2016.

[152] A. Nielsen *et al.*, "Synthetic edge and scrape-off layer diagnostics—a bridge between experiments and theory," *Nuclear Fusion*, vol. 59, p. 086059, jul 2019.

[153] M. Faitsch *et al.*, "Dependence of the L-mode scrape-off layer power fall-off length on the upper triangularity in TCV," *Plasma Physics and Controlled Fusion*, vol. 60, p. 045010, mar 2018.

[154] P. A. Schneider *et al.*, "Differences in the H-mode pedestal width of temperature and density," *Plasma Physics and Controlled Fusion*, vol. 54, p. 105009, aug 2012.

[155] F. Militello, W. Fundamenski, V. Naulin, and A. H. Nielsen, "Simulations of edge and scrape off layer turbulence in mega ampere spherical tokamak plasmas," *Plasma Physics and Controlled Fusion*, vol. 54, p. 095011, aug 2012.

[156] A. Kukushkin *et al.*, "Consequences of a reduction of the upstream power SOL width in ITER," *Journal of Nuclear Materials*, vol. 438, pp. S203 – S207, 2013. Proceedings of the 20th International Conference on Plasma-Surface Interactions in Controlled Fusion Devices.

[157] M. L. Reinke *et al.*, "Heat flux mitigation by impurity seeding in high-field tokamaks," *Nuclear Fusion*, vol. 57, no. 3, p. 034004, 2017.

[158] R. J. Goldston *et al.*, "A new scaling for divertor detachment," *Plasma Physics and Controlled Fusion*, vol. 59, no. 5, p. 055015, 2017.

[159] H. Sun *et al.*, "Relating the near SOL transport with plasma properties of the confined edge region in ASDEX Upgrade," *Plasma Physics and Controlled Fusion*, sep 2019.

[160] S. Wiesen *et al.*, "The new SOLPS-ITER code package," *Journal of Nuclear Materials*, vol. 463, pp. 480–484, 2015.

[161] B. LaBombard *et al.*, "Scaling of the power exhaust channel in Alcator C-Mod," *Physics of Plasmas*, vol. 18, no. 5, p. 056104, 2011.

[162] M. G. Dunne *et al.*, "Global performance enhancements via pedestal optimisation on ASDEX Upgrade," *Plasma Physics and Controlled Fusion*, vol. 59, p. 025010, dec 2016.

[163] G. Grenfell *et al.*, "Measurement and control of turbulence spreading in the scrape-off layer of TJ-II stellarator," *Nuclear Fusion*, vol. 59, p. 016018, dec 2018.

[164] X. Chen *et al.*, "Stationary QH-mode plasmas with high and wide pedestal at low rotation on DIII-D," *Nuclear Fusion*, vol. 57, p. 022007, sep 2016.

[165] B. Sorbom *et al.*, "ARC: A compact, high-field, fusion nuclear science facility and demonstration power plant with demountable magnets," *Fusion Engineering and Design*, vol. 100, pp. 378 – 405, 2015.

[166] D. Silvagni *et al.*, "I-mode pedestal relaxation events at ASDEX Upgrade," *Nuclear Fusion*, vol. 60, p. 126028, oct 2020.

[167] E. J. Doyle *et al.*, "Modifications in turbulence and edge electric fields at the L-H transition in the DIII-D tokamak," *Physics of Fluids B: Plasma Physics*, vol. 3, no. 8, pp. 2300–2307, 1991.

[168] M. Cavedon *et al.*, "Pedestal and E_r profile evolution during an edge localized mode cycle at ASDEX Upgrade," *Plasma Physics and Controlled Fusion*, vol. 59, p. 105007, aug 2017.

[169] L. Frassinetti *et al.*, "Effect of nitrogen seeding on the energy losses and on the time scales of the electron temperature and density collapse of type-I ELMs in JET with the ITER-like wall," *Nuclear Fusion*, vol. 55, p. 023007, jan 2015.

[170] E. Viezzer *et al.*, "Investigation of inter-ELM ion heat transport in the H-mode pedestal of ASDEX Upgrade plasmas," *Nuclear Fusion*, vol. 57, p. 022020, oct 2016.

[171] M. R. Wade *et al.*, "Edge impurity dynamics during an edge-localized mode cycle on DIII-D," *Physics of Plasmas*, vol. 12, no. 5, p. 056120, 2005.

[172] A. Burckhart *et al.*, "Inter-ELM behaviour of the electron density and temperature pedestal in ASDEX Upgrade," *Plasma Physics and Controlled Fusion*, vol. 52, p. 105010, sep 2010.

[173] I. Nunes *et al.*, "Characterization of the density profile collapse of type I ELMs in ASDEX Upgrade with high temporal and spatial resolution reflectometry," *Nuclear Fusion*, vol. 44, pp. 883–891, jul 2004.

[174] I. Nunes *et al.*, "Density profile analysis during an ELM event in ASDEX Upgrade H-modes," *Nuclear Fusion*, vol. 45, pp. 1550–1556, nov 2005.

[175] M. Beurskens *et al.*, "Pedestal and scrape-off layer dynamics in ELMy H-mode plasmas in JET," *Nuclear Fusion*, vol. 49, p. 125006, nov 2009.

[176] A. Chankin *et al.*, "Fast ELM dynamics in JT-60U," *Nuclear Fusion*, vol. 42, pp. 733–742, jun 2002.

[177] A. Mikhailovskii *et al. Plasma Physics Reports*, vol. 23, pp. 844–857, 1997.

[178] J. W. Connor *et al.*, "Magnetohydrodynamic stability of tokamak edge plasmas," *Physics of Plasmas*, vol. 5, no. 7, pp. 2687–2700, 1998.

[179] A. Burckhart *et al.*, "ELM behaviour and linear MHD stability of edge ECRH heated ASDEX Upgrade plasmas," *Nuclear Fusion*, vol. 56, p. 056011, apr 2016.

[180] A. Kirk *et al.*, "The spatial structure of type-i ELMs at the mid-plane in ASDEX upgrade and a comparison with data from MAST," *Plasma Physics and Controlled Fusion*, vol. 47, pp. 995–1013, may 2005.

[181] B. Goncalves *et al.*, "Edge localized modes and fluctuations in the JET SOL region," *Plasma Physics and Controlled Fusion*, vol. 45, pp. 1627–1635, aug 2003.

[182] A. Schmid *et al.*, "Experimental observation of the radial propagation of ELM induced filaments on ASDEX Upgrade," *Plasma Physics and Controlled Fusion*, vol. 50, p. 045007, feb 2008.

[183] G. Fuchert *et al.*, "Blob properties in L- and H-mode from gas-puff imaging in ASDEX Upgrade," *Plasma Physics and Controlled Fusion*, vol. 56, p. 125001, oct 2014.

[184] G. Birkenmeier *et al.*, "Magnetic field dependence of the blob dynamics in the edge of ASDEX Upgrade L-mode plasmas," *Plasma Physics and Controlled Fusion*, vol. 56, p. 075019, jun 2014.

[185] M. Griener *et al. In preparation*, 2020.

[186] M. E. Fenstermacher *et al.*, "ELM particle and energy transport in the SOL and divertor of DIII-D," *Plasma Physics and Controlled Fusion*, vol. 45, pp. 1597–1626, aug 2003.

[187] K. Itami *et al.*, "Characteristics of heat flux and particle flux to the divertor in H-mode of JT-60U," *Journal of Nuclear Materials*, vol. 220-222, pp. 203 – 207, 1995. Plasma-Surface Interactions in Controlled Fusion Devices.

[188] A. Kuang *et al.*, "Conceptual design study for heat exhaust management in the ARC fusion pilot plant," *Fusion Engineering and Design*, vol. 137, pp. 221 – 242, 2018.

[189] T. Hirai *et al.*, "ITER tungsten divertor design development and qualification program," *Fusion Engineering and Design*, vol. 88, no. 9, pp. 1798–1801, 2013. Proceedings of the 27th Symposium On Fusion Technology (SOFT-27); Liège, Belgium, September 24-28, 2012.

[190] S. Carpentier-Chouchana *et al.*, "Status of the ITER full-tungsten divertor shaping and heat load distribution analysis," *Physica Scripta*, vol. T159, p. 014002, apr 2014.

[191] F. Palermo *et al.*, "Scaling laws from theory-based modeling for different regimes in the DEMO fusion reactor," *Nuclear Fusion*, vol. 59, p. 096010, jul 2019.

Acknowledgments

I would like to thank everybody who supported me in these three years and made this work possible.
First, I am deeply grateful to my academic supervisor Ulrich Stroth, who allowed me to be part of the ASDEX Upgrade team and who constantly guided me throughout my entire Ph.D. work. Moreover, I would like to thank very much my supervisor Thomas Eich for being my best motivator and for having taught me so much about power exhaust. Furthermore, special thanks go to Michael Faitsch, who introduced me to infrared cameras and answered all my day-to-day questions, and to Tim Happel, who taught me all known and unknown aspects of I-mode plasmas.
This work could not be possible without the help and commitment of the entire ASDEX Upgrade team, from the technicians to the session leaders during experimental days. A big acknowledgment goes to all of you.
The discussions with expert physicists at IPP have been the foundations over which I build up this thesis. For this reason I would like to thank particularly Elisabeth Wolfrum, Peter Manz, Marco Wischmeier, Bernhard Sieglin, Dominik Brida, Dirk Nille and Luís Gil. Also, I would like to thank Albrecht Herrmann for his precious advice on emissivity measurements of divertor tiles, and Stefan Eder for his support in the IR lab as well as in installing the IR cameras at the ASDEX Upgrade tokamak.
Additionally, I would like to thank who helped me in tutoring the Double Plasma Experiment, in particular Ferdinand Hitzler and Lennart Bock, but also Andreas Bolland who was always available to repair broken filaments and pumps on a short notice.
But what made this work possible was also the nice work atmosphere at IPP and the tight human bonds created among colleagues. Special thanks go to Monika Koleva for her deep friendship, but also to the Italian crew (Teobaldo Luda di Cortemiglia, Nicola Bonanomi, Riccardo Casagrande), to the Spanish crew (Joaquin Galdon Quiroga, Javier Gonzalez Martin, Pilar Cano Megías, Diego Cruz Zabala), to Anton Jansen Van Vuuren, Klara Höfler, Georg Harrer, Alex Bock, Balázs Tál, Michael Griener, Ulrike Plank, Andres Cathey Cevallos, Martin Hosner and to my office mate Pierre David.
A big thanks to my flatmates Carmine Pellegrino and Nora Penzel who helped me not to get crazy during the Covid-19 lockdown and to be very productive in that period.

Dulcis in fundo, I would like to thank my family who always supported me during these three years.